2009-12-02

Prediction of Fluid Viscosity Through Transient Molecular Dynamic Simulations

Jason Christopher Thomas
Brigham Young University - Provo

PREDICTION OF FLUID VISCOSITY THROUGH TRANSIENT MOLECULAR DYNAMIC SIMULATIONS

by

Jason Thomas

A dissertation submitted to the faculty of

Brigham Young University

in partial fulfillment of the requirements for the degree of

Doctor of Philosophy

Department of Chemical Engineering

Brigham Young University

December 2009

BRIGHAM YOUNG UNIVERSITY

GRADUATE COMMITTEE APPROVAL

of a dissertation submitted by

Jason Thomas

This dissertation has been read by each member of the following graduate committee and by majority vote has been found to be satisfactory.

Date	Richard L. Rowley, Chair
Date	Dean R. Wheeler
Date	W. Vincent Wilding
Date	Thomas A. Knotts
Date	William G. Pitt

BRIGHAM YOUNG UNIVERSITY

As chair of the candidate's graduate committee, I have read the dissertation of Jason Thomas in its final form and have found that (1) its format, citations, and bibliographical style are consistent and acceptable and fulfill university and department style requirements; (2) its illustrative materials including figures, tables, and charts are in place; and (3) the final manuscript is satisfactory to the graduate committee and is ready for submission to the university library.

Date

Richard L. Rowley
Chair, Graduate Committee

Accepted for the Department

Dean R. Wheeler
Graduate Coordinator

Accepted for the College

Alan R. Parkinson
Dean, Ira A. Fulton College
of Engineering and Technology

ABSTRACT

PREDICTION OF FLUID VISCOSITY THROUGH TRANSIENT

MOLECULAR DYNAMIC SIMULATIONS

Jason Thomas

Department of Chemical Engineering

Doctor of Philosophy

A novel method of calculating viscosity from molecular dynamics simulations is developed, benchmarked, and tested. The technique is a transient method which has the potential to reduce CPU requirements for many conditions. An initial sinusoidal velocity profile is overlaid upon the peculiar velocities of the individual molecules in an equilibrated simulation. The transient relaxation of this initial velocity profile is then compared to the corresponding analytical solution of the momentum equation by adjusting the viscosity-related parameters in the constitutive equation that relate the shear rate to the stress tensor.

The newly developed Transient Molecular Dynamics (TMD) method was tested for a Lennard-Jones (LJ) fluid over a wide range of densities and temperatures. The simulated values were compared to an analytical solution of the boundary value problem for a Newtonian fluid. The resultant viscosities agreed well with those published for Equilibrium Molecular Dynamics (EMD) simulations up to a dimensionless density of 0.7. Application of a linear viscoelastic Maxwell constitutive equation was required to achieve good agreement at dimensionless densities greater than 0.7. When the Newtonian model is used for densities in the range of 0.1 to 0.3 and the Maxwell model is used for densities higher than 0.3, the TMD method was able to predict viscosities with an uncertainty of 10% or better.

Application of the TMD method to multi-site molecules required the Jeffreys constitutive equation to adequately fit the simulation responses. TMD simulations were performed on model fluids representing *n*-butane, isobutane, *n*-hexane, water, methanol, and hexanol. Molecules with strong hydrogen bonding and Coulombic interactions agreed well with NEMD simulated values and experimental values. Simulated viscosities for nonpolar and larger molecules agreed with NEMD simulations at low to moderate densities, but deviated from these values at higher densities. These deviations are explainable in terms of potential model inaccuracies and the shear-rate dependence of both NEMD and TMD viscosity values. Results show that accurate viscosity predictions can be made for multi-site molecules as long as the shear-rate dependence of the viscosity is not too large or is adequately addressed.

ACKNOWLEDGMENTS

I would like to thank my wife Kara who has supported me through my schooling. I also want to thank Richard Rowely for his help and support in my endevours.

Table of Contents

List of Tables

List of Figures

Chapter 1

Introduction

Transport properties are important physical properties of a fluid. They can be experimentally measured at many temperatures and pressures, but not at all conditions. High temperatures and pressures can be problematic for experimental design, and thermal decomposition may make high-temperature measurements impossible, yet such conditions commonly exist where lubricants are used. In addition, experimental measurements can be expensive and time consuming. Consequently, a reliable and efficient method for prediction of transport properties, accurate at virtually any condition, is desirable. Many current viscosity prediction methods are based on group contribution methods, corresponding states theory, or empirical correlations. These methods are of limited accuracy and do not extrapolate well to chemicals and conditions outside the domain of experimental data upon which they were based. Newer molecular dynamics simulations methodologies offer possible solutions to these challenges based on physically realistic simulations on the molecular scale.

In this study, a new transient molecular dynamics (TMD) method is developed and tested as a more efficient method to predict viscosity at virtually any condition. While the general idea and preliminary implementation of a TMD method for transport property predictions are not new, the approach used here is a novel, more general and efficient approach. The purpose of this research is to develop, benchmark and test a reliable TMD method which is quicker, simpler to implement and more flexible than previous molecular dynamics methods, that has broader applicability and that is more accurate than semi-empirical

or theoretical correlations for the prediction of viscosity. An immediate and significant need of the method is in the Design Institute for Physical Properties (DIPPR®) Project 801 at Brigham Young University where prediction methods must be used to obtain the temperature dependence of vapor and liquid viscosities for new compounds to be included in the database, but for which there are no experimental values. Current methods have been found to be very limited in accuracy, sometimes being in error by more than an order of magnitude.

There are a number of methods currently available for estimating different transport properties. The methods most commonly used to predict viscosity fall into the following categories: empirical correlations, corresponding states methods, group contribution methods, and molecular dynamics simulations.

Empirical correlations, corresponding states methods and group contribution methods rely on trends in properties that correlate with compound structure. A distinct advantage of these types of methods is their simplicity, ease of use, and hand-calculator-level computations, but they are often only applicable to certain types or families of compounds. For instance, empirical correlations should not be used on families or compounds dissimilar to the ones used in the correlations' development. Corresponding states methods should only be used on conformal fluids, generally excluding fluids comprised of strongly-polar or hydrogen-bonded molecules, unless specifically extended to these types of compounds. Group contribution methods also are restrictive in the types of molecules and families that can be considered as they depend upon having regressed information from experiment for the type and possible arrangement of the various chemical moieties within the molecule. They generally neglect electron induction effects from next-nearest neighbor groups. Even if a method can be applied to a particular compound, the resulting accuracy can vary widely. As a general rule, gas viscosity can be better predicted than liquid viscosity due to a stronger theoretical basis. Methods for liquids often rely on empirical trends, restricting their generality. At any one condition, there can be large differences among values predicted us-

ing empirical correlations, corresponding states methods and group contribution methods. And, predicting an accurate temperature and pressure dependence using these methods can be even more difficult.

Molecular dynamics simulation offers an alternative method for predicting viscosity by modeling interactions at the molecular level. These methods predict fluid properties from the underlying physical forces between the molecules themselves. Models for these molecular forces typically include Lennard-Jones interaction sites to account for van der Waals forces and can include charges to account for Coulombic forces associated with polar interactions and association. Current techniques have shown promise in predicting viscosity for the simple molecules for which they have been tested, although their main drawback is the substantial computer time required to obtain statistically accurate values. Their main advantage is that the simulated properties result naturally from the molecular interactions model. This means that all of the physics, the temperature and pressure dependence of the properties as well as their inter-relationships, are fully included, and accuracy at any condition depends primarily upon the accuracy of the intermolecular potential model. However, ease of implementation and computational efficiency vary with the available methods.

The two dominant methods used today are equilibrium molecular dynamics (EMD) and non-equilibrium (steady-state) molecular dynamics (NEMD) methods. Time is spent implementing, maintaining and modifying codes, but currently a primary limitation of these methods is the actual simulation time required to get results. For all of these methods, increased simulation time usually increases the result's accuracy for a given molecular potential. EMD methods use natural fluctuations within the fluid to obtain transport properties, but prolonged simulation times are required to achieve accurate results because of the low signal-to-noise ratio. NEMD methods are designed to enhance the signal-to-noise ratio by applying very large (orders of magnitude larger than physically realizable) shear rates in the simulation, but in so doing they require multiple long simulations made at several different shear rates to effectively extrapolate to zero (or at least to a physically realizable)

shear rate. While both methods are successful, the excessive simulation time required still restricts their wide use. In this work, we seek to develop a transient simulation method that will take advantage of the tremendous strengths of MD simulation methods while minimizing the current disadvantages mentioned above.

A selection of current analytical prediction methods is reviewed. The assumptions of the analytical prediction methods determine the scope of the methods and show where they can be used reliably. Next, current molecular dynamic simulation methods are presented to show what capabilities are currently available and provide a basis for comparison. The transient simulation method is developed for the well characterized Lennard-Jones fluid and results are compared to previous simulation studies. Application of the transient simulation method is applied to more complex molecules and the method is extended to account for a more complex behavior. Results show the strengths and weaknesses of the transient simulation method and where improvement can be made.

Chapter 2

Analytical Prediction Methods

The important role viscosity plays in many engineering applications has led many to develop prediction methods. The viscosity of a fluid is a strong function of density and less so a function of temperature. The strong density dependence makes it difficult to develop a method to cover both liquid and vapor densities. Typically, empirical correlations, corresponding-states methods and group-contribution methods treat condensed-phase (liquid) and vapor-phase viscosities separately. The primary features of current methods that can be used to characterize the method are identified in this chapter, although some methods can use multiple features spanning the different types. While many methods have been developed, only the most notable methods will be discussed.

2.1 Types of Analytical Prediction Methods

The principal types of analytical prediction methods are empirical correlation methods, corresponding-state methods, and group-contribution methods. Empirical correlation methods are the least robust prediction methods and may be limited to a specific compound, family, or group of compounds. Group-contribution methods tend to be simpler to implement and more general. A similarity between basic molecular groups is assumed and often the contribution of a group is assumed to be linearly additive. The last method type presented, corresponding states, relies on the similarity of observed behavior and applies trends observed in one compound to another.

2.1.1 Empirical Correlations

Experimental viscosity has been correlated with a multitude of functional forms. Some are simple in form and applicable to only one compound. Not only can they not be extended to other compounds, they may even have trouble when extrapolated outside of the original conditions upon which the method was based. Other correlations are more complex, relate some physical quantity to viscosity, and attempt to be general for the vast majority of organic compounds. Some postulated physical explanations have been connected to certain functional forms in an effort to either improve accuracy or broaden applicability. Although potential underlying physical relationships are presented with some correlations, agreement with experiment tends to be a stronger driving force for acceptance.

Many examples of empirical correlations can be found, a few of which are below. Sometimes a correlation reduces the viscosity value in some way, similar to corresponding states. The most general type of empirical correlations often employs a functional form similar to

$$\ln \eta = A + \frac{B}{T} + C \ln T + DT^E \tag{2.1}$$

where η is viscosity, T is temperature, and the other variables are fitting parameters. This functional form provides the flexibility needed to account for three trends seen when $\ln \eta$ is graphed versus $1/T$;

- The dependence of $\ln \eta$ on $1/T$ is approximately linear
- Higher temperature viscosities can deviate below the linear trend
- Lower temperature viscosities can deviate above the linear trend

The variables A and B account for the linear dependence. Deviations about the linear trend at temperature extremes can be fitted with the remaining C, D, and E coefficients.

The functional forms given below demonstrate how different reference points can produce variations on the general theme above.

$$\ln\left(\frac{\eta}{\eta_b}\right) = B\left(\frac{1}{T}-\frac{1}{T_b}\right)+C\ln\left(\frac{T}{T_b}\right)+D\left(T^E-T_b^E\right) \tag{2.2}$$

$$\ln\eta_r = \frac{B}{T_b}\left(\frac{1}{T_r}-1\right)+C\ln T_r+DT_b^E\left(T_r^E-1\right) \tag{2.3}$$

Here T_b is the normal boiling point, η_b is the viscosity at T_b, and T_r is temperature reduced by the critical point temperature, and η_r is the reduced viscosity made dimensionless by dividing by the viscosity at the critical point.

2.1.2 Group-Contribution Methods

Group-contribution methods are a popular and straightforward way to predict viscosity. Molecules are divided into individual groups by chemical functionality and each group is assigned a viscosity contribution. Group-contribution methods tend to be the most comprehensive prediction methods, although groups lacking a defined contribution can be a problem, i.e., the desired group is not found in the reported method. An advantage of group-contribution methods is the ability to create a method based on a small set of common groups and, when needed, less common groups can usually be added without altering the original method.

The choice of groups is often crucial to the accuracy and complexity of a method. Some common methods of defining groups are as individual atoms (C, H, O, N, etc.), as simple functional groups (CH_3, -CH_2-, CH_2, -OH, etc.), or as longer-range functional groups connected to specific neighbors (CH_2-CH_2-OH, etc.). The complexity of the method increases from the former to the later. The more complex methods can also have difficulty predicting values for molecules dissimilar to those used to develop the method [1]. Group-contribution methods tend to be the most versatile, robust, and popular prediction methods currently used [2].

2.1.3 Corresponding States

The similarity between liquid molecular interactions gives rise to similarities in the viscous behavior of liquids when appropriately compared on equivalent bases. Property values for different compounds are calculated through a mapping or transformation of the data. Graphically, multiple data sets are collapsed into one data set through the mapping function. The saturated liquid viscosities of the *n*-alkanes, Figure 2.1, exhibit similar temperature-dependent behavior that suggests an appropriate transformation could collapse the curves into one. One state point of the reduced data set would correspond to different state points for different molecules. The correspondence of different state points from different molecules to one reduced state point is called corresponding-states. This single data set would then be referred to as reduced viscosity values. The success of such a method can be measured by plotting multiple reduced data sets and measuring the scatter of the data. A successful method would result in a coherent trend with little scatter. The greater the scatter the less accurate the method. Adjusting the *n*-alkane data found in Figure 2.2 to correspond at the critical point by reducing the temperature with the critical temperature and reducing the viscosity with ξ is successful to an extent in collapsing the viscosity at higher temperatures, but less so near the melting point. The value ξ is defined as

$$\xi = \left(\frac{RT_c N_0^2}{P_c^4 M^3} \right)^{1/6} . \tag{2.4}$$

where R is the universal gas constant, T_c is the critical temperature, N_0 is Avogadro's number, P_c is the critical pressure, and M is the molecular weight. While the curves appear closer together, there is room for improvement considering the curves fan out at lower temperatures. A method which uses corresponding states principles is the method by Przezdziecki and Sridhar [3]. Values predicted using this method can disagree with experimental data significantly, and the predicted values can exhibit unphysical trends, such

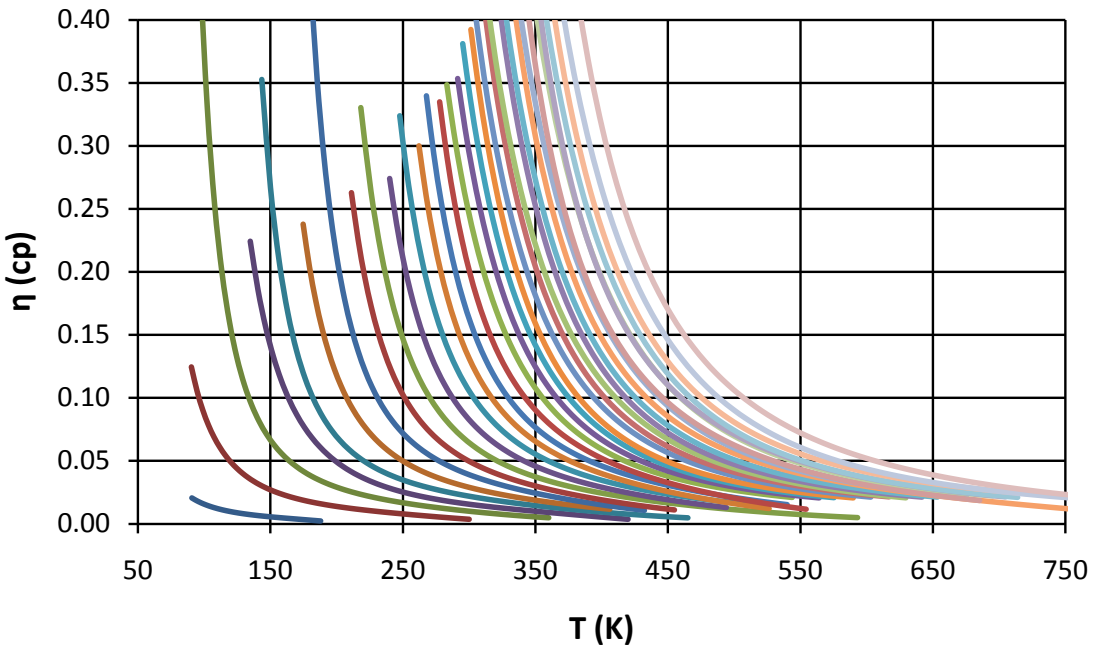

Figure 2.1: The saturated liquid viscosities of the *n*-alkanes [4]. Methane is the first curve at the bottom left and towards the right the number of carbon atoms increases. Values for molecules with 1 – 30, 32, and 36 carbon atoms are plotted.

as increasing viscosity for increasing temperature of saturated liquids at higher temperatures [4].

2.2 Vapor Viscosity

Vapor viscosity is among the easier transport properties to predict. There is sufficient theoretical basis to calculate the ideal-gas viscosity accurately. Accurate low-density methods are generally modifications of the well-known Chapman-Enskog solution [5]. Some of these methods include the Reichenberg method [6, 7, 8], the method of Yoon-Thodos [9], the method of Stiel-Thodos [10], and the method of Chung [11]. For an ideal gas, statistical mechanics provides a theoretical background for the method of Chung. The methods of Reichenberg, Yoon-Thodos and Stiel-Thodos build upon the Chapman-Enskog method

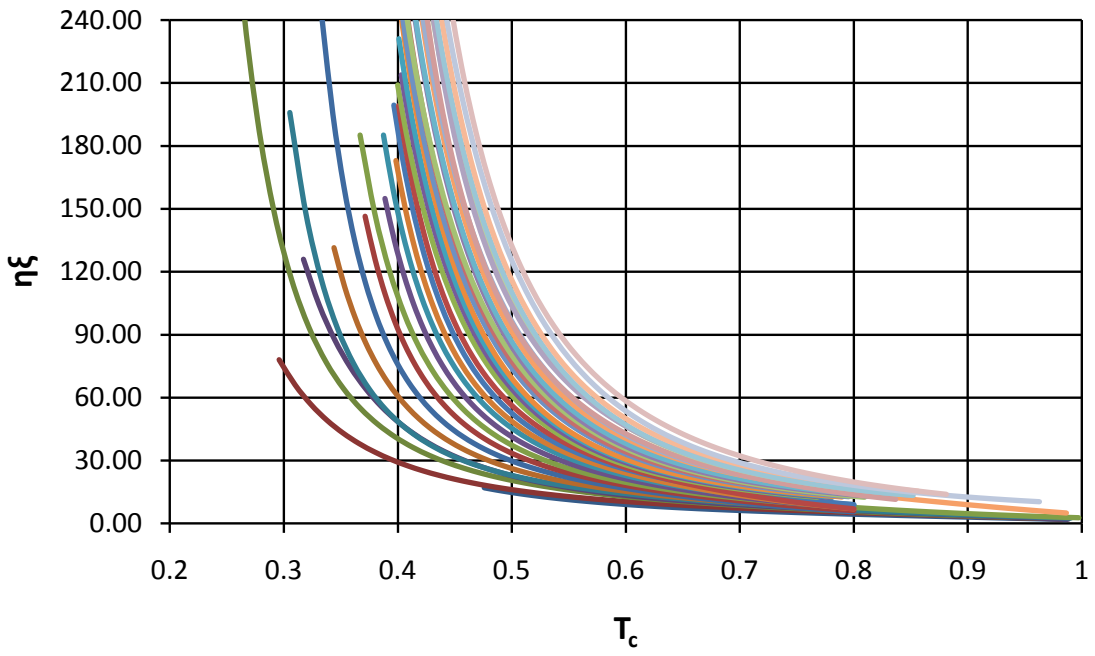

Figure 2.2: The saturated liquid viscosities of the *n*-alkanes plotted as a function of reduced temperature and reduced viscosity obtained with the reducing parameter ξ [4]. Methane is the first curve at the bottom. Compare to Figure 2.1.

and include corrections based on corresponding states. Corresponding-states methods typically do poorly for polar or highly-branched molecules. Extended Lee-Kesler methods also exist, but are not typically used. One extended Lee-Kesler method designed to account for polarity was developed by Okeson and Rowley [12]. The training set used indicates errors below 10 percent, but the method has not been tested further. Based on experience, the DIPPR® 801 project has found that the Reichenburg, Yoon-Thodos, Chung and Stiel-Thodos methods produce errors typically below 10 percent. Despite the well-behaved nature of most gases, none of the methods above deal adequately with associating gases. This is an area in which molecular dynamics simulations clearly excel.

Chapman-Enskog

The Chapman-Enskog method is based on a rigorous calculation for a dilute monatomic gas. The method assumes a low-density limit because the binary collisions are treated explicitly, while collisions involving three or more molecules are truncated from the expansion used to develop the method. As the density of the gas increases, the higher-order collisions occur more frequently and lead to deviations from theory. Treatment of the binary collisions involves multiple integrals over the intermolecular potential to give a collision integral. A hard-sphere potential gives a collision integral of 1. The Chapman-Enskog method uses numerically calculated values of the collision integrals for a Lennard-Jones potential. These values have been tabulated and correlated for convenience [13].

$$\Omega_\eta = \frac{1.16145}{T^{*0.14874}} + \frac{0.52487}{\exp(0.77320T^*)} + \frac{2.16178}{\exp(2.43787T^*)} \,. \tag{2.5}$$

The value T^* is defined as k_bT/ε where k_b is Boltzmann's constant, T is the temperature, and ε is the Lennard-Jones well-depth parameter. The collision integral Ω is then related to the viscosity η by

$$\eta = \frac{5}{16}\frac{\sqrt{\pi m k_b T}}{\pi\sigma^2\Omega_\eta} \tag{2.6}$$

where σ is the Lennard-Jones size parameter and m is the mass of a molecule. For molecules adequately modeled with a Lennard-Jones potential, the results are virtually exact for the low-density limit.

2.3 Liquid Viscosity

While vapor viscosity is relatively easy to predict, liquid viscosity proves much more difficult. All the methods to be discussed have little theoretical basis and rely heavily on empiricism. Methods such as Hsu's method [14], Van Velzen's method [1], Bhethanabotla's

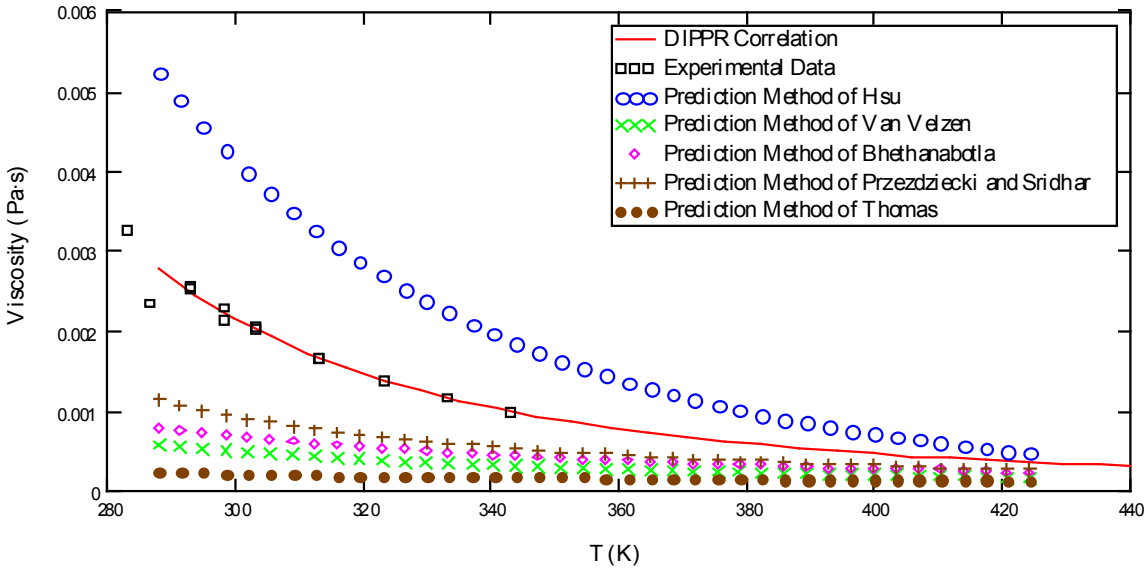

Figure 2.3: Prediction of liquid viscosity by various methods for cyclooctane.

method [15], Thomas' method [16], and the method of Przezdziecki and Sridhar [3] can disagree significantly. For example, Figure 2.3 compares the predicted values for cyclooctane to the experimental values and the DIPPR® 801 recommended correlation. Van Velzen, Bhethanabotla and Thomas are all group-contribution methods, while the Przezdziecki and Sridhar method is a corresponding-states method. Some methods develop the whole temperature-dependent curve all at once, while the basis of other methods is an accurate prediction of the viscosity at one point and with an added on temperature dependence. The Hsu and Van Velzen prediction methods are thought to predict liquid viscosity within about 10%. The Bhethanabotla, Thomas and Przezdziecki-Sridhar methods are believed to predict liquid viscosity within a 25% error. Because liquid viscosity is so much harder to predict than vapor viscosity, there remains much room for improved prediction in this area.

2.3.1 The Method of Thomas

Thomas [16] proposed a group-contribution method of the form

$$\log\left(\eta\sqrt{v}\right) = 0.0670 + k\left(\frac{T_c}{T} - 1\right) \tag{2.7}$$

where η is the liquid viscosity in $10^{-1}\cdot\text{mPa}\cdot\text{s}$, v is specific volume in $\text{cm}^3\cdot\text{g}^{-1}$, and k is a sum of group contributions. Molecules are split primarily into atomic groups (C, I, H, O, Cl, S, Br) with specific groups for double bonds, C_6H_5, CO (ketones and esters), and CN (cyanides). The basis of the method is that $\log\left(\eta\sqrt{v}\right)$ at the critical point is approximately constant for normal non-associated liquids with further variations accounted for by the group sum k. 123 compounds were used in the method's development resulting in an average error of 5% for 108 compounds, but the remaining compounds either showed significant prediction errors or a k value could not be calculated. The method of Thomas is a very simple prediction method, but its lack of group parameters and prediction errors for compounds not included in the original analysis significantly hinder its utilization.

2.3.2 The Method of Hildebrand

Hildebrand [17] based his model of viscosity on the ability of the fluid to flow due to expansion beyond the closest-packed structure of the fluid. The model is generally written as

$$\frac{1}{\eta_L} = B\left(\frac{V - V_0}{V_0}\right) . \tag{2.8}$$

The parameter B represents the ability of the molecules to absorb momentum while V_0 represents a molecular volume at which viscous flow stops. This method has been a starting point for other prediction methods and is a fluidity model because the inverse of the viscosity, or the fluidity, is proportional to the free space within the fluid. The fluidity is viewed as linear relative to the expansion of the fluid beyond the core molecular volume, V_0.

2.3.3 The Method of Przezdziecki and Sridhar

Przezdziecki and Sridhar [3] present a correlation of liquid viscosity values based on Hildebrand's fluidity model. The method attempts to accurately predict values of B and V_0 which can then be used in Hildebrand's model.

B is correlated according to the following equation

$$B = \frac{0.33V_c}{f_1} - 1.12\,, \tag{2.9}$$

where

$$f_1 = 4.27 + 0.032M_W - 0.077P_c + 0.014T_m - 3.82\frac{T_m}{T_c} \tag{2.10}$$

and V_c is the critical volume in $\mathrm{cm}^3 \cdot \mathrm{mol}^{-1}$, P_c is the critical pressure in atm, T_c is the critical temperature in K, T_m is the melting temperature in K, and M_W is the molecular weight in $\mathrm{g} \cdot \mathrm{mol}^{-1}$.

V_0 is correlated with the volume at the melting temperature

$$V_0 = 0.0085T_c\omega - 2.02 + \frac{V_m}{0.342\frac{T_m}{T_c} + 0.894} \tag{2.11}$$

where ω is the acentric factor. Przezdziecki and Sridhar note that it is very important to accurately predict V_0 because Equation 2.8 is very sensitive to the value of V_0. This sensitivity leads to some erroneous predictions due to unphysical behavior when V_0 is inaccurately chosen. The most notorious behavior is the unrealistic decrease in viscosity as temperature decreases along the liquid saturation curve. The published method shows predictions for 27 compounds and reports an average error of 8.7%.

2.3.4 The Method of Van Velzen

An alternative view of the mechanism of momentum transport in liquids, in opposition to the fluidity model proposed by Hildebrand, is that of Eyring's theory of activated

complexes. In this view, movement of one molecule past another is an activated process, requiring energy for one molecule to move past another into a hole in the fluid. This gives rise to the so-called Andrade equation which ascribes a reciprocal-temperature dependence to the logarithm of viscosity with the corresponding coefficient being related to the activation energy. Van Velzen's method [1] assumes the liquid viscosity adheres to the Andrade equation between the melting point and the normal boiling point,

$$\log(\eta_L) = A + B/T \ . \tag{2.12}$$

This is modified to give

$$\log(\eta_L) = A\left(\frac{1}{T} - \frac{1}{T_0}\right) \tag{2.13}$$

where $T_0 = -B/A$. B and T_0 are determined by the functional groups and structural effects.

The Andrade equation gives a straight line behavior relationship between $\log(\eta_L)$ and $1/T$. It is acknowledged that for certain compounds such as associated liquids and hydrocarbon mixtures of higher molecular weight that the behavior is actually slightly curved. Van Velzen and coworkers have chosen the simpler functional form knowing accuracy would suffer for such compounds.

The approach used in this method is to correlate the chain length N for the n-alkanes to values of B and T_0. Depending on the magnitude of N, one of two correlations is chosen. For all other compounds an equivalent chain length is calculated to allow the correlations developed for n-alkanes to be used. The B value is then adjusted further based on structure or functional groups. While the chosen function is simple, calculation of the parameters B and T_0 is not. For many compounds with sufficient differences from those included in the regression set, predicted values suffer greatly.

2.3.5 The Method of Hsu

Hsu's method [14] is an empirical group-contribution method. It is valid between the melting point and a reduced temperature of 0.75 at atmospheric pressure. The method is based on the following equation which has proven effective in correlating data:

$$\ln(\eta_L) = A + BT + \frac{C}{T^2} + D\ln(P_c) \tag{2.14}$$

where A, B, C, and D are found by group contributions, P_c is the critical pressure in bar, and η is in mPa $\cdot$ s. The method's test set used 482 organic compounds with 4627 experimental data points. The AAD% was 4.14. Aromatics, alcohols and ketones showed slightly higher deviations. A test set of 35 organic compounds with 117 data points gave the lowest average deviation when compared to the methods of van Velzen, Przezdziecki and Sridhar, and Orrick and Erbar [18, 19]. Application of the method is straightforward and only requires knowledge of P_c.

2.3.6 The Method of Bhethanabotla

Bhethanabotla's method [15] can be used up to a reduced temperature of 0.8. Like the Van Velzen method, it is based on the activated process view of viscosity or the Andrade temperature dependence. An equation of the form

$$\ln\left(\frac{\eta}{\rho M_W}\right) = A + \frac{B}{T} \tag{2.15}$$

is used where A and B are found by group contributions and ρ is the density and M_W is the molecular weight. Use of van Velzen's method would generally be preferred over this method.

2.3.7 The Method of Okeson and Rowley

Okeson and Rowley's method [12] is a four-parameter corresponding-states method developed to be an extended Lee-Kesler method. The reducing parameter, ξ, for viscosity is

$$\xi = \left(\frac{RT_c N_0^2}{P_c^4 M^3} \right)^{1/6} . \tag{2.16}$$

R is the universal gas constant, T_c is the critical temperature, N_0 is Avogadro's number, P_c is the critical pressure, and M is the molecular weight. The viscosity is correlated with the following equation

$$\eta\xi = (\eta\xi)_0 + \frac{\alpha}{\alpha_1}\left[(\eta\xi)_1 - (\eta\xi)_0\right] + \beta\left\{(\eta\xi)_2 - (\eta\xi)_0 - \frac{\alpha_2}{\alpha_1}\left[(\eta\xi)_1 - (\eta\xi)_0\right]\right\} \tag{2.17}$$

where α is a size/shape factor and β is a polar factor. The subscripts indicate that three reference fluids are used. Methane is reference fluid 0, *n*-octane is reference fluid 1, and water is reference fluid 2. The value of α is given by

$$\alpha = -7.706 \times 10^{-4} + 0.0330r + 0.01506r^2 - 9.997 \times 10^{-4} r^3 \tag{2.18}$$

where r is the radius of gyration. The value for β must be back-calculated based on a single data point, but not necessarily from a viscosity value. The extended Lee-Kesler method was developed for other fluid properties as well and typically a density point can be used to obtain the value of β which is independent of the type of property being considered.

Reducing Parameter

When developing their method Okeson and Rowley found that the reducing parameter given in Equation 2.16 produced the best agreement of their method with experiment. However, there are many ways to construct a reducing parameter. Okeson and Rowley had

considered another reducing parameter of

$$\xi_T = \frac{V_c^{2/3}}{(T_c M_W)^{1/2}} \,. \tag{2.19}$$

The difference between ξ and ξ_T is the value of the critical compressibility factor. The critical values within ξ and ξ_T could be replaced by other compound properties. T_c could be replaced by T_b, P_c by 1 atm, and V_c by V_b. The choice of reducing parameter only needs to be influenced by its efficacy at "reducing" differences for a single chosen point of commonality, whether this be the critical point, boiling point, or other designated point.

2.4 Methods Covering Gas and Liquid Viscosity

Because of the difficulty of developing a prediction method which covers both vapor and liquid viscosities, few have been developed. A well-known method covering a large density range is presented below.

TRAnsport Property Prediction (TRAPP)

TRAPP is an extended corresponding states method for nonpolar fluid mixtures for densities ranging from dilute gas to dense liquid [20]. The only constants used are critical constants and the acentric factor. The viscosity of the mixture of interest, η_{mix}, is related to the viscosity of a hypothetical pure fluid, η_x, at the given temperature and density. This hypothetical pure fluid is then related to a reference fluid using a factor F_η based on corresponding states:

$$\eta_{mix}(\rho, T) = \eta_x(\rho, T) = \eta_0(\rho_0, T_0) F_\eta \,. \tag{2.20}$$

The factor F_η is calculated based on the molecular weight M and substance reducing parameters $f_{x,0}$ and $h_{x,0}$ using

$$F_\eta = \frac{M_x}{M_0}^{1/2} f_{x,0}^{1/2} h_{x,0}^{-2/3} \,, \tag{2.21}$$

where x refers to the hypothetical pure fluid of interest and 0 is the reference fluid. The state point of the ideal pure fluid and the corresponding state point of the reference fluid are related by the substance reducing parameters.

$$T_0 = \frac{T}{f_{x,0}} \tag{2.22}$$

$$\rho_0 = \rho h_{x,0} \tag{2.23}$$

Further details found in the literature on the calculation of $f_{x,0}$ and $h_{x,0}$ show that these are functions of the critical parameters and acentric factor and use mixing rules for mixtures based on van der Waals mixing rules [20]. The substance reducing parameters and density are iteratively solved prior to calculating F_η.

For TRAPP the reference fluid was chosen to be methane which was the only fluid with adequate experimental data at the time. Because the range of data available for the reference fluid dictates the scope and accuracy of the method, the relatively high freezing point of methane on a reduced scale had to be addressed. A 32-term BWR equation of state for methane was extended and extrapolated to 40 K. The reference viscosity correlation utilized was based on methane's experimental viscosity except for high densities where pseudo-data based on propane allowed a sufficient density range to be covered. At high densities a noncorrespondence in viscosity was also taken into account.

The authors of TRAPP initially were interested in properties of LNG and light hydrocarbon mixtures which made methane a suitable reference fluid. The method was found to work well for hydrocarbons having up to 20 carbon atoms. The prediction error for pure fluids and mixtures is reported to be on the order of 7 to 8% [20].

2.5 Conclusion

Each of the methods presented has expanded the prediction capabilities available. Although prediction methods have become more powerful and accurate over time, the limita-

tions imposed by assumptions and data sets used in the regressions must be remembered. Group-contribution methods such as Hsu's method can be used for a diverse set of compounds; however, common compounds with ample experimental data may be better characterized by an empirical correlation. Methods such as TRAPP are reliable and accurate over a large range of state points; however, this method can only be used for hydrocarbon mixtures. Methods which do not cover the desired density and temperature range or which do not apply to the fluids of interest cannot be used reliably. Out of the large number of methods available, each has its strengths and weaknesses indicating that at present a tradeoff of generality and accuracy must usually be made.

Chapter 3

Simulation Methods

3.1 Current Molecular Dynamics Methods

Molecular dynamics simulations have been used to obtain a number of fluid properties including viscosity. Comprehensive overviews of molecular dynamics simulations have been written by Allen and Tildesley [21] and Frenkel and Smit [22]. It has been shown that viscosity model data can be obtained from molecular dynamics simulations in two principal ways. Equilibrium molecular dynamics (EMD) have been used to successfully calculate viscosity from the Green-Kubo relations [23, 24, 25]. The other principal method is through nonequilibrium molecular dynamics (NEMD) [26, 27, 28, 29, 30].

3.1.1 Equilibrium Molecular Dynamics – Green Kubo Formalism

EMD predictions calculate time correlations using the mechanical variables of molecules found in equilibrated molecular dynamics simulations and relate the time correlations to transport properties. The Green-Kubo integral formula is used to obtain the viscosity from the integral of the averaged time correlation function for the decay of natural fluctuations in the localized off-diagonal elements of the pressure tensor:

$$\eta = \frac{V}{k_b T} \int_0^\infty \langle \tau_{\alpha\beta}(0) \tau_{\alpha\beta}(t) \rangle \mathrm{d}t \ , \tag{3.1}$$

where the components of the pressure tensor are given by

$$\tau_{\alpha\beta}(t) = \frac{1}{V}\sum_{i}\left(\frac{p_{\alpha i}p_{\beta i}}{m_i} + \alpha_i f_{\beta i}\right). \tag{3.2}$$

Here η is the viscosity, V is volume of the simulation cell, T is temperature, t is time, k_b is the Boltzmann constant, $\tau_{\alpha\beta}$ is an off-diagonal element of the pressure tensor ($\alpha \neq \beta$), i is a molecular index, p is momentum, m is molecular mass, f is force, α is a Cartesian coordinate, and β is a Cartesian coordinate [21].

The integral over infinite time is truncated for use with simulations of finite length. A long simulation is required due to the slow convergence of the integral. The slow integral convergence is often referred to as a long time tail. Data from basic molecular dynamics simulations evaluated in accordance with Equations 3.1 can accurately predict the viscosity, but use of this method may require prohibitively long simulations for routine use. This is because the natural fluctuations in the off-diagonal elements of the pressure tensor are small so that many averages of the time correlation function are required to achieve statistical reliability.

3.1.2 Steady-State Periodic Perturbation

The steady-state periodic perturbation method applies a periodic force and relates the steady-state velocity profile to the viscosity [31, 32]. The periodic force does not depend on time and is represented by

$$F_x(z) = m\dot{\gamma}\sin\left(\frac{2\pi n z}{L_z}\right), \tag{3.3}$$

where $\dot{\gamma}$ is a constant shear rate, m is the mass of an individual particle, n is the wave number, and L_z is the box length in the z direction. The analytical solution to the Navier-Stokes equations for the supplied force is itself a steady-state periodic velocity profile. The chosen force is applied and the velocity profile is allowed to develop. Once a steady-state

is reached the magnitude of the resulting sinusoidal velocity profile is fit to the equation

$$u_x(z) = u_0 \sin\left(\frac{2\pi n z}{L_z}\right) , \tag{3.4}$$

where u_0 is the magnitude of the profile. The magnitude is then related to the shear viscosity by

$$\eta = \frac{\rho L_z^2 \dot{\gamma}}{4\pi^2 n^2 u_0} , \tag{3.5}$$

where ρ is the mass density. A thermostat, such as that by Berendenson [33, 34], is needed because the external force constantly adds energy to the system which eventually becomes thermal motion.

A couple of issues arise when implementing this method. The larger the simulation size the longer it will take to reach steady-state. The efficiency of the method decreases as the time prior to reaching steady-state dwarfs the time after reaching steady state. In addition, it is possible that the viscosity depends on the wavelength which could require an extrapolation to zero wavelength. Multiple runs could be used to fit the wave-length dependence, or a sufficiently small wavelength could be found by increasing the simulation size and/or decreasing n to 1.

Simulation results for a Lennard-Jones fluid were reported in the literature for a number of state points [31, 32]. Results obtained showed that the velocity profile was sinusoidal within a tolerable error, but the viscosity was dependent upon the magnitude of $\dot{\gamma}$. Results agreed with published EMD values only when the $\dot{\gamma}$ corresponding to the lowest viscosity value was used.

3.1.3 Boundary-Driven NEMD

In boundary-driven NEMD simulations, the system is driven by application of forces or changes in the molecular motion or energy at the boundaries in order to enhance the signal-to-noise ratio and decrease the amount of averaging required to obtain statistically reliable

results. One method uses "sliding brick" boundary conditions, known as the Lees-Edwards boundary conditions [35]; see Figure 3.1. The rate at which adjacent boxes slide past each other is related to the shear rate as described below.

Introduced into the equations of motion is a drift velocity that maintains the fluid in Coutte flow,

$$v_d(y) = y\frac{\mathrm{d}v_x}{\mathrm{d}y}\,, \tag{3.6}$$

where v_d is the drift velocity and $\mathrm{d}v_x/\mathrm{d}y$ is the shear rate. The maximum drift velocity occurs at the top of the simulation cell, $y = L_y$, where L_y is the length of the cell in the y direction, and the replicate box above that can be viewed as a sliding box of velocity $v_d(L_y)$ with the same linear additional drift velocity profile within the replicate box above as given in Equation 3.6. When a particle crosses boundaries into an adjacent "sliding" box, its position and velocity are altered before normal periodic boundary conditions (PBC) are applied. Looking at Figure 3.1, the drift velocity v_d is subtracted from the molecular velocity of a molecule that crosses the upper boundary or added to the velocity of a molecule that crosses the lower boundary before the molecule is placed back into the simulation cell on the opposite side of the cell by the periodic boundary conditions. The position is also adjusted by a displacement x_{disp} if the molecule crosses the upper boundary or subtracted if the molecule crosses the lower boundary. The displacement is found according to

$$x_{disp} = v_d t - L_x \mathrm{floor}(v_d t/L_x) \tag{3.7}$$

where t is time, and L_x is the length of the simulation in the x direction. The function floor() simply truncates the non-integer portion. The result of the boundary conditions is Coutte flow, but the linear velocity profile takes time to develop. If non-polar molecules are incorporated into the simulation, then the Lee-Edwards boundary conditions are easily added. If polar molecules are incorporated, then the method used to account for Coulombic

interactions must also be altered. This is not a trivial matter, but the technique to do so is available in the literature [36].

3.1.4 Homogeneous Field-Driven NEMD

Like boundary-driven NEMD simulations, homogeneous field-driven NEMD simulations drive the system to create Coutte flow. However, the homogeneous field-driven algorithms include an additional force on all of the molecules in the simulation, not just those at the boundaries. With respect to viscosity, homogeneous field-driven NEMD simulations alter the equations of motion to either apply a specified shear rate and measure shear stress, or impose a well-defined shear stress and measure the shear rate. The SLLOD equations of motion combined with the Lees-Edwards boundary conditions [35] form the primary NEMD method used in simulations. The SLLOD equations are derived from Newton's equations of motion and are constrained to give Couette flow. The SLLOD equations of motion are

$$\dot{\mathbf{q}}_i = \frac{\mathbf{p}_i}{m} + \mathbf{q}_i \cdot \nabla \mathbf{u} \,, \tag{3.8}$$

$$\dot{\mathbf{p}}_i = \mathbf{F}_i - \nabla \mathbf{u} \cdot \mathbf{p}_i \,, \tag{3.9}$$

where $\nabla \mathbf{u}$ is the shear rate tensor, m is the mass of a site, $\mathbf{q}_i$ is the position of site i, $\mathbf{p}_i$ is the momentum of site i, $\dot{\mathbf{q}}_i$ is the time derivative of position, and $\dot{\mathbf{p}}_i$ is the time derivative of momentum. For Coutte flow there is only one non-zero element, $(\nabla \mathbf{u})_{yx} = \dot{\gamma}$. This gives

$$\dot{\mathbf{q}}_i = \frac{\mathbf{p}_i}{m} + \hat{\mathbf{x}} \dot{\gamma} y_i \,, \tag{3.10}$$

$$\dot{\mathbf{p}}_i = \mathbf{F}_i - \hat{\mathbf{x}} \dot{\gamma} p_{yi} \,. \tag{3.11}$$

Due to better signal-to-noise ratios, NEMD simulations are more computationally efficient than EMD simulations. However, the shear rates required are much higher than any experimental apparatus is capable of measuring and result in non-Newtonian behavior.

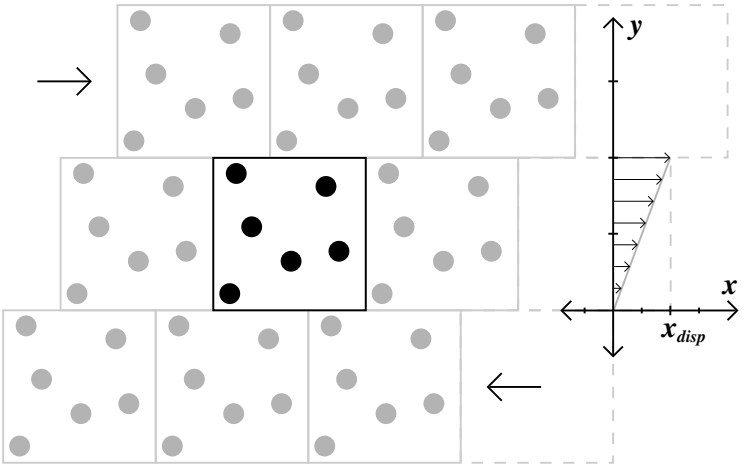

Figure 3.1: Representation of Lees-Edwards boundary conditions.

As discussed below, results at several different shear rates are required to extrapolate to a zero-shear-rate viscosity. As a result NEMD simulations still require substantial effort and simulation time, limiting their use as a routine prediction method.

Viscosity Shear-Rate Dependence

Many fluids of interest exhibit Newtonian behavior for the shear rates encountered in real-world fluid applications; however, MD simulations often show non-Newtonian behavior. The apparent discrepancy between experiment and simulation is due to the high shear rates needed in NEMD simulations to create a signal strong enough to overcome the noise. Typically the largest shear rates achievable in experiment are orders of magnitude lower than those commonly used in NEMD simulations. Experimental shear rates are typically limited to be below 10^5 s^{-1} while many simulated shear rates are on the order of 10^9 s^{-1}. This is a concern for those using MD simulations to predict real world conditions and with most compounds it is unclear at what point Newtonian behavior gives way to non-Newtonian behavior. Some experimentalists have seen non-Newtonian behavior of fluids such as $C_{30}H_{62}$, but at very large pressures and low temperatures. There has been some work focused on achieving lower shear rates in simulation [37].

To address the shear-rate dependence of viscosity as seen in NEMD simulations, different extrapolation procedures to zero shear have been used [38, 39, 40, 41, 42, 43, 44]. Simulations at different shear rates are carried out, and the dependence of viscosity upon shear rate is fitted to some functional form. One example uses a linear dependence to correlate viscosity and shear rate, $\dot{\gamma}$, with an example extrapolation seen in Figure 3.2.

A frequently used shear-rate dependence of viscosity assumes viscosity is proportional to the square root of shear rate, $\dot{\gamma}^{1/2}$. This assumption appears to do well for low density liquid data, but may not do so well for very dense liquids. The sample extrapolation for isobutane in Figure 3.2 shows that the assumed temperature dependence appears to be valid for low densities, but it appears to fail at the higher densities which led the researchers to ignore these values in the fit because the assumed dependence is no longer linear. The extrapolation procedure resulting from linear response theory [38, 39] is also proportional to $\dot{\gamma}^{1/2}$ given by

$$\eta = \eta_0 + A\dot{\gamma}^{1/2} \tag{3.12}$$

where η is the viscosity for a given shear rate $\dot{\gamma}$, and η_0 and A are fitting parameters. η_0 is taken to be the zero-shear viscosity value reported in the literature.

For polymeric compounds, a power law is often used to fit the shear-rate dependence of experimental data. The form of the power law is given by

$$\eta = A\dot{\gamma}^{n-1} \, . \tag{3.13}$$

MD simulation results have used the power law to fit the shear-rate dependence [40]. Such a dependence predicts a linear behavior when $\log\eta$ is graphed vs. $\log\dot{\gamma}$ (log of shear rate). The value $n-1$ is often found to be in the range -0.4 to -0.9 for polymeric liquids. NEMD simulations for hexadecane produced a value of -0.45, which was within the experimentally observed range. Although $n-1$ falls within the experimentally valid range, the actual

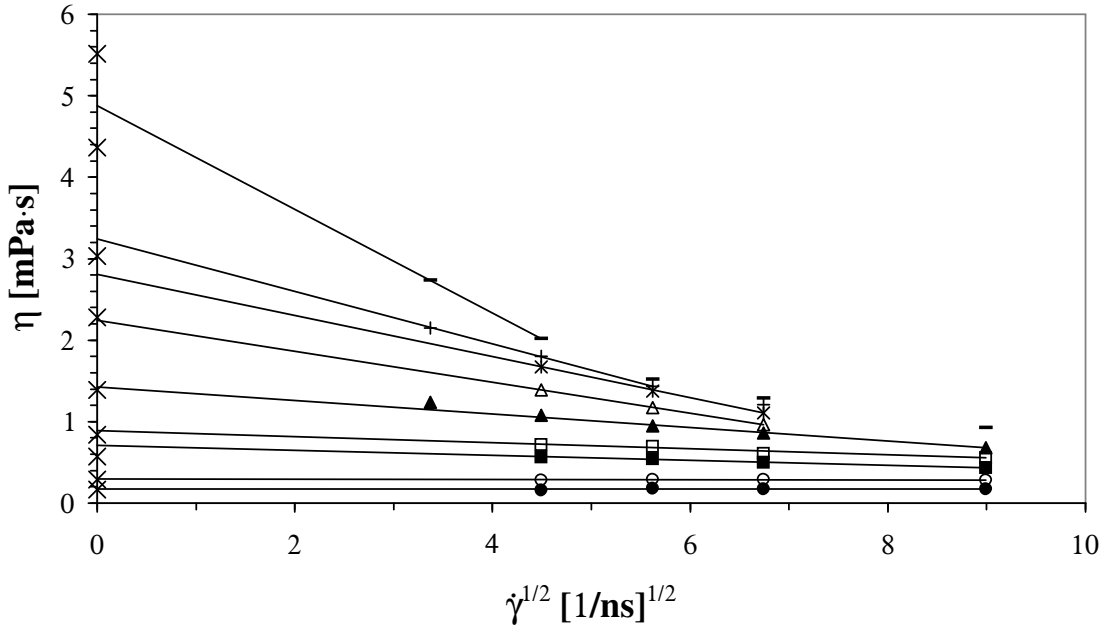

Figure 3.2: NEMD extrapolation applied to isobutane results for viscosity [45, 46]. Multiple shear rates at the following state points were used to extrapolate to a zero-shear viscosity: 9.905 kmol/m^3 & 300 K (●), 10.735 kmol/m^3 & 250 K (○), 11.502 kmol/m^3 & 200 K (■), 11.822 kmol/m^3 & 180 K (□), 12.141 kmol/m^3 & 140 K (▲), 12.333 kmol/m^3 & 135 K (△), 12.461 kmol/m^3 & 120 K (⋆), 12.589 kmol/m^3 & 125 K (+), and 12.716 kmol/m^3 & 125 K (–). Values obtained from EMD simulations corresponding to the above state points are plotted as an (×) at zero shear. Used with permission from Rowley and Ely [46].

viscosity values were found to be too low. The under-predicted viscosities for hexadecane were assumed to result from an inadequate potential model.

Another scheme to fit the shear-rate dependence is given by

$$\eta = \eta_0 - A\dot{\gamma}\,. \tag{3.14}$$

One could also use [41, 42]

$$\eta = \eta_0 - A\dot{\gamma}^2\,. \tag{3.15}$$

An inverse viscosity relation has also been proposed [43]

$$\eta^{-1} = \eta_0^{-1} - A\, P_{xz}\,. \tag{3.16}$$

Shear-rate-dependent viscosity appears to have different regimes. At high shear rates there is often one shear-rate dependence, and another at lower shear rates. This can be seen in the different slopes shown in Figure 3.2 at different shear rates for the higher density simulations. At very low shear rates, a Newtonian plateau region has been identified. One model known as the Carreau–Yasuda model tries to incorporate both shear dependence and a plateau region with the given functional form [44]

$$\frac{\eta - \eta_0}{\eta - \eta_\infty} = [1 + (\lambda\dot{\gamma})a)]\,\frac{\eta - 1}{a} \tag{3.17}$$

NEMD simulations of 2,2,4,4,6,8,8-heptamethylnonane over a range of shear rates exhibit a plateau region as shown in Figure 3.3.

In summary, there are a number of schemes that can be used to fit the shear-rate dependence of viscosity. Unfortunately each one is based on particular example fluids which limit the predictive or extrapolation capability to new fluids under investigation. Many results have been published using a square-root dependence on shear rate, but as more computationally intensive simulations are carried out at lower shear rates, a plateau is reached. The plateau region is taken to be independent of shear rate allowing one to obtain the low- or zero-shear viscosity from the average of points within the plateau region. This of course requires substantial computer time to identify the plateau region. Moreover, use of the plateau region to get the zero-shear value is limited by the same efficiency issues as EMD simulations where the statistical noise associated with a low driving force requires longer simulations. It is important to understand the errors associated with the extrapolation procedure regardless of the method chosen.

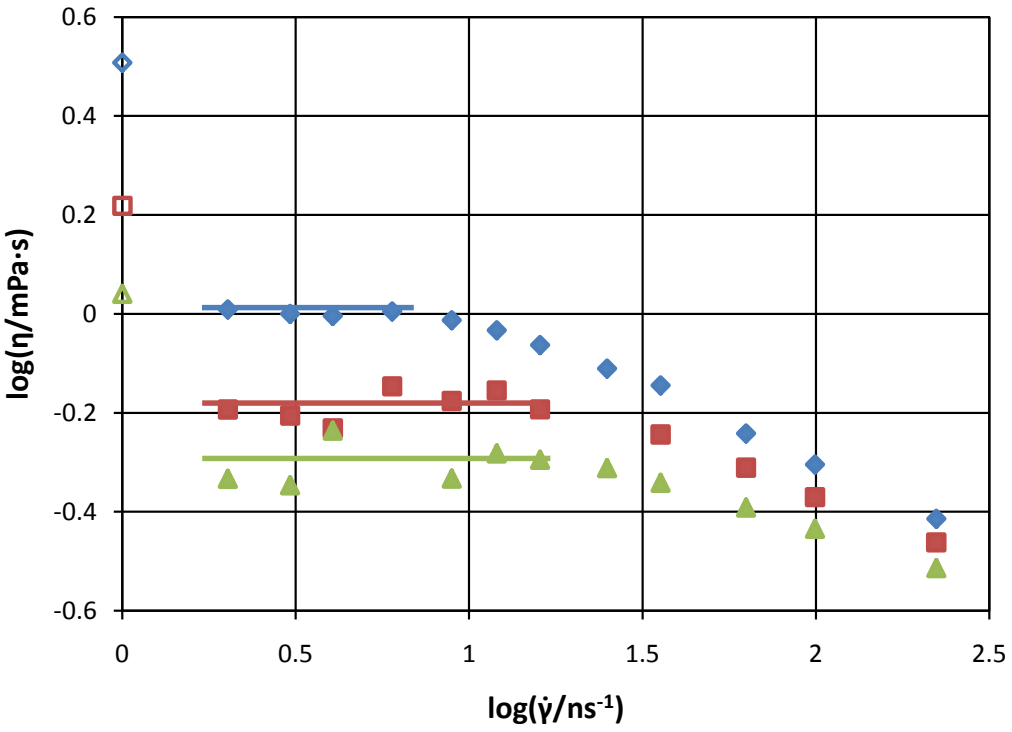

Figure 3.3: NEMD simulations of 2,2,4,4,6,8,8-heptamethylnonane at 0.1 MPa and 298 K (◆), 333 K (■), and 363 K (▲) show a distinct plateau in the viscosity values at lower shear rates [47]. Lines have been drawn to highlight the plateau region where viscosity appears independent of shear rate. Experimental values corresponding to the above state points are plotted as open symbols.

3.2 TMD Methods

Unlike NEMD methods which rely on a steady-state value, transient molecular dynamics (TMD) methods attempt to explain time varying behavior. Three previous TMD methods include prediction of mutual diffusion, viscosity and thermal conductivity. All three methods specify initial and boundary conditions and obtain appropriate solutions to the macroscopic equations of change for momentum, energy and mass. The data are then fitted to the macroscopic solutions to obtain transport coefficients. The three transient methods are summarized below.

In 1993, Maginn and colleagues presented a TMD method to predict diffusivity of

methane in silicalite [48]. The method (referred to as gradient relaxation molecular dynamics (GRMD)) uses a step profile in the concentration gradient. The equation used in their regression was a Fourier series solution that required tracking the concentration in both space and time. The method was deemed computationally demanding and appeared to under-predict diffusivities. The under-prediction was blamed on the simulation being outside the linear response regime where Fick's law is applicable. This method apparently was not developed further for diffusivity.

In 2000, Arya, Maginn and Chang published a TMD method to predict viscosity [49]. They referred to this method as the momentum impulse relaxation method (MIR). A Gaussian velocity profile was used with a Fourier series solution in the infinite domain. This required the PBCs to be modified to mimic the infinite domain. The computational efficiency of the method was shown to be a significant improvement over EMD and NEMD methods. Arya and coworkers conceded that the main disadvantages of their method are the modifications required to the PBCs and the inability of the modified PBCs to completely mimic an infinite domain. To account for these shortcomings, larger simulation boxes were used and the initial Gaussian velocity profile was chosen so that the bulk of the "hump," or velocity gradient region, was far from the boundaries. This leads to a less efficient use of the simulation cell and makes the method more reliant on choosing a "good" Gaussian shape for a given condition. The inefficiency is due to the large portion of the momentum gradient that is confined to a small portion of the total simulation cell which results in only a small portion of the molecules participating in momentum transport. A more efficient method would allow a larger fraction of the molecules to significantly contribute to the momentum transport process. This method apparently was not developed further for viscosity.

In 2005, Hulse and colleagues presented a TMD method to predict thermal conductivity [50]. A lumped-capacitance approach was used for a small, instantaneously heated volume within the overall fluid simulation cell with the solution given in spherical coordi-

nates. A spherical volume of molecules within a cubic simulation cell is heated and allowed to relax. Subsequently, the temperature of the heated molecules is then tracked to give a temperature decay which is then fitted to the transient solution of the energy equation subject to semi-infinite boundary conditions. The isochoric heat capacity of the simulation was also found from the simulation in order to calculate the residual thermal conductivity with reference to a zero-density liquid. A zero-density thermal conductivity was added to obtain the actual thermal conductivity.

Hulse found a bias in his simulation temperature profiles. Hulse noted [51] that allowing the thermal conductivity to vary with temperature eliminated the bias in this temperature profiles, but resulted in a slight, consistent under prediction. The Hulse method, similar to the MIR method, does not use the entire simulation cell to transport energy and is inefficient in that sense. Finally, the transient solution against which the simulated response is matched assumes a constant thermal conductivity independent of temperature, which may be a source of error for the large temperature gradients used.

Deficiencies in the previous methods include a number of issues. One such issue already noted is inefficient simulation cell usage. Both the viscosity and thermal conductivity methods limit initial gradients to a small portion of the simulation cell and therefore only a fraction of the molecules participates in momentum or energy transport. Another issue is the PBC changes required by the MIR method. As a side effect of the boundary-condition deficiencies, larger gradients are used to counteract the inefficient use of the simulation cell volume. Maginn and coworkers' GRMD method has adequate boundary conditions, but it has a large gradient that is initially discontinuous. These large gradients may generate nonlinear responses not properly accounted for in the method.

In addition, an issue that is not fully addressed in any of the previous studies is ballistic effects that occur at the start of any transient method. Ballistic phenomena at extremely short times are due to the more straight-line velocities of molecules before collisions with neighboring molecules alter the velocities and the properties dependent upon them. Hulse's

thermal conductivity method clearly showed nonconformity to the continuum equations at the beginning of the response to the temperature jump. This difference was most likely a ballistic phenomenon and should be expected to occur. Ballistic effects are more prominent in gases than liquids, but they still exist in liquids at very short times observable in TMD simulations.

Improvements in transport-property prediction will always be desired. These improvements include simpler prediction methods, more efficient prediction ability and better accuracy. In the realm of molecular dynamics simulations, these correlate to easier code implementation and quicker simulation times for a given accuracy. The simplicity and clarity of a method are also good characteristics. By this we mean that simulations that mimic experimental determinations of transport properties aid in the recognition of potential difficulties, the equivalency of the simulated and measured transport property, and in the identification of possible improvements to the method. In addition to efficiency, these are some of the characteristics incorporated in the TMD method developed in the next chapter.

Chapter 4

Transient Molecular Dynamics: Development and Results for a LJ Fluid

4.1 Viscosity Prediction

To adequately predict viscosity using a TMD method, a suitable solution to a physically meaningful boundary-value problem must be made. For a molecular dynamics simulation based on Cartesian coordinates, a Cartesian-coordinate solution should naturally give the easiest and simplest solution. The equation of change for momentum can be simplified by several realistic assumptions. Any simulation where viscosity will play a role includes velocity gradients. When one assumes that there is no bulk flow in the y or z direction and there are no pressure gradients or external forces, the equation of change for momentum simplifies to

$$\rho \frac{\partial v_x}{\partial t} = \eta \frac{\partial^2 v_x}{\partial y^2} \tag{4.1}$$

where ρ is density, v_x is the velocity in the x direction and η is the viscosity. This is the same equation that Arya et al. used in their MIR method. Although they solved the equation for an initial Gaussian velocity distribution on an infinite domain, we will solve the equation on a periodic finite domain, better representing the molecular dynamics simulation with its PBC. When the velocity profile is an even function about the boundaries, the above equation can be solved with a finite Fourier integral transform with the Neumann-Neumann

boundary conditions of

$$\left(\frac{\partial v_x}{\partial y}\right)\Big|_{y=0} = 0 = \left(\frac{\partial v_x}{\partial y}\right)\Big|_{y=L} \tag{4.2}$$

to give the following solution

$$v_x(t,y) = C_0\frac{1}{L} + \frac{2}{L}\sum_{n=1}^{\infty} C_n \cos\left(\frac{n\pi}{L}y\right)\exp\left[-\frac{\eta}{\rho}\left(\frac{n\pi}{L}\right)^2 t\right] \tag{4.3}$$

where

$$C_n = \int_0^L v_x(0,\xi)\cos\left(\frac{n\pi}{L}\xi\right)\mathrm{d}\xi \quad \text{for } n = 0,1,2,\ldots \tag{4.4}$$

Here t is time, L is the length of the simulation box in the y direction and ξ is an integration variable in the y direction. In order to fit the molecular dynamics simulation to the boundary conditions, an initial velocity profile must be chosen such that the profile is an even function about the boundary condition (the profile forms a mirror image on either side of the boundary). In accordance with the previous statement and to simplify the Fourier series solution, the initial velocity profile

$$v_x(0,y) = v_{max}\cos\left(\frac{2\pi}{L}y\right) \tag{4.5}$$

is used to obtain the following simple solution of Equations 4.1 – 4.5.

$$v_x(t,y) = v_{max}\cos\left(\frac{2\pi}{L}y\right)\exp\left[-\frac{\eta}{\rho}\left(\frac{2\pi}{L}\right)^2 t\right] = v_x(0,y)\phi(t)\ , \tag{4.6}$$

where v_{max} is the maximum streaming velocity and $\phi(t)$ is the magnitude of the velocity profile normalized by the profile at $t = 0$. The initial velocity profile and solution also indicate that there is no net bulk velocity. Such a solution is simple and suggests that a molecular dynamics simulation using the above constraints will have an exponential decay in time of the streaming velocity profile. Molecules throughout the cell transport momen-

tum and the whole cell is involved in the regression of η from Equation 4.6, enhancing the method's efficiency.

Anticipating the above solution, one first equilibrates the molecular dynamics simulation and then adds the above initial velocity profile to the random velocities of the simulation. Because the solution above indicates that one can separate the spatial solution from the temporal solution, analysis of the data becomes simplified. Rather than fit all the data at once, it can be done in two steps. At each time step, the magnitude of the sinusoidal profile is found. The decay of the sinusoidal profile is then fit to an exponential. Finally, the viscosity is extracted from the parameters of the exponential fit. Fitting the data becomes simple and efficient.

4.2 Preliminary Results

Simulations have been carried out for a Lennard-Jones fluid to predict viscosity at a number of different conditions. The range of conditions and their accuracy indicates how versatile the TMD method is at predicting viscosity. A typical run at a particular condition is repeated and averaged to get both an average value and to quantify the repeatability of the results. Simulations for a Lennard-Jones fluid were run using dimensionless quantities. Dimensionless quantities are found with the following relations:

$$T^* = k_b T/\varepsilon\,, \tag{4.7}$$

$$\rho^* = \rho\sigma^3 N_0\,, \tag{4.8}$$

$$t^* = t(\varepsilon/m\sigma^2)^{1/2}\,, \tag{4.9}$$

$$\eta^* = \eta\sigma^2/(m\varepsilon)^{1/2}\,, \tag{4.10}$$

where T is temperature, ρ is molar density, t is time, η is viscosity, k_b is Boltzmann's constant, N_0 is Avogadro's number, m is a molecule's mass, ε is the LJ well-depth parameter,

Table 4.1: Preliminary results over a range of conditions compared to EMD simulation results of Painter et al. [52].

T^*	ρ^*	η^*_{tmd}	$\pm$	η^*_{emd}	$\pm$
1.5	0.4	0.428	0.035	0.412	0.052
0.8	0.8	2.188	0.215	2.325	0.41
2.1	0.8	1.832	0.124	1.852	0.455

and σ is the LJ size parameter. Comparison with previous EMD results [52] show good agreement.

Fitting is best done by separating the spatial and temporal portions of Equation 4.6. The spatial data are analyzed by fitting data to a sinusoidal curve at specified time steps. The combined results over a number of time steps can then be fitted to the temporal portion of the equation with an exponential decay. The regressed parameter of the exponent is then used to obtain the viscosity. The spatial element of the data is fitted in the code, while a representative graph of the temporal element can be seen in Figures 4.1 and 4.2 below. The manipulated spatial data can be fitted directly with an exponent as shown in Figure 4.1, or the equation can be linearized by taking the logarithm of the data and fitting these values to a line as shown in Figure 4.2. Fitting the data to an exponential function appears to give the best fit, but viewing the natural log of the data helps identify any ballistic effects, as evident in the left of Figure 4.2. It is evident that the first few time steps should be truncated before a fit is made. Lennard-Jones sites continuously exert a force upon one another; however the strong interaction within a couple diameters behaves similarly to the collision of two hard spheres. The inverse of the collision frequency for hard spheres, shown as the vertical line at short times in Figures 4.1 and 4.2, seems to adequately predict the amount of truncation required. The previous TMD papers fail to make note of the required truncation and this would presumably account for some low predictions, particularly at low densities. Preliminary results are found in dimensionless units in Table 4.1 below and are compared to the simulation results of Painter et al. [52].

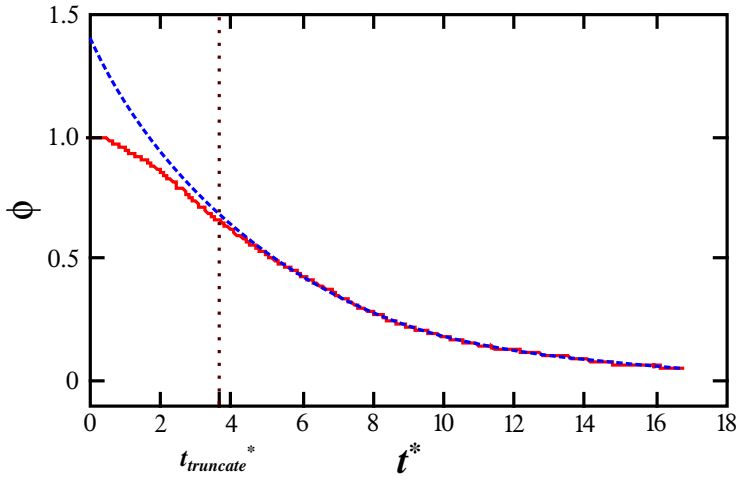

Figure 4.1: Fit to exponential decay and truncated ballistic region seen prior to vertical dotted line. ϕ is the magnitude of the velocity profile normalized by the profile at $t = 0$. (—) simulation results, (----) fit, and (···) truncation.

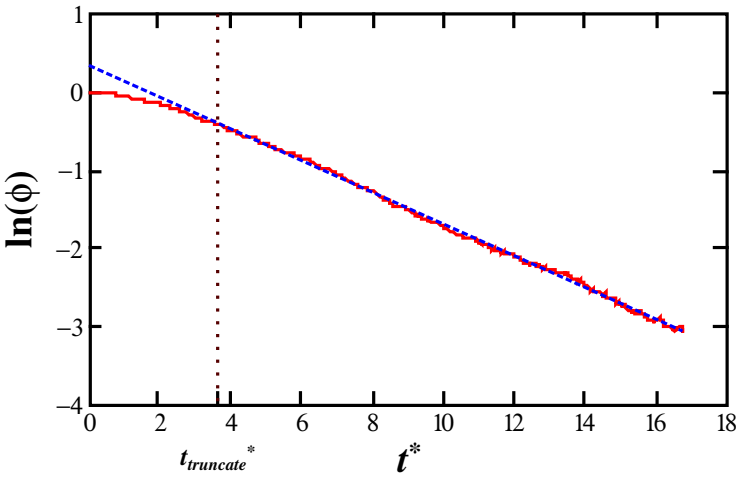

Figure 4.2: Linear fit to exponential decay and truncated ballistic region seen prior to vertical dotted line. ϕ is the magnitude of the velocity profile normalized by the profile at $t = 0$. (—) simulation results, (----) fit, and (···) truncation.

Application of the Lennard-Jones fluid results to other fluids is easily done by choosing the appropriate Lennard-Jones parameter values for ε and σ. A table of Lennard-Jones parameters for simple molecules is found in Table 4.2.

Table 4.2: Lennard-Jones parameters for simple molecules [5].

	σ (Å)	ε/k_b (K)
He	2.576	10.2
Ne	2.789	35.7
Ar	3.432	122.4
Kr	3.675	170.0
Xe	4.009	234.7
CH_4	3.780	154

4.3 Theory

In the TMD method, the simulation configuration conforms to that of a physically-meaningful solvable boundary-value problem with an initial non-equilibrium profile of a property that relaxes toward equilibrium. The transport property governing the profiles rate of decay toward equilibrium is obtained by adjusting it to obtain the best fit (usually in a least-squares sense) of the solution of the macroscopic boundary-value problem to the corresponding response observed in the simulation. For example in a TMD method developed by Hulse et al. [50], molecules within a small spherical region of a previously equilibrated simulation cell are instantaneously heated by scaling their velocities. The subsequent transient temperature decay of this spherical region is then matched, by adjusting the value of the thermal conductivity in the analytical solution, to the analytical solution of the macroscopic boundary-value problem corresponding to the temperature decay of a spherical fluid with an initial temperature higher than the spatially infinite, initially isothermal fluid in which it is embedded. Similarly, the TMD method developed by Maginn and

coworkers [48, 49, 53] matches the transient decay of an initial composition or velocity profile to the analytical solutions of the corresponding boundary value problems for mass and momentum transfer, respectively, by adjusting the diffusion coefficient or viscosity.

The method developed in this study is analogous to these previous methods in requiring the transient simulation to conform to a well-defined macroscopic boundary-value problem for which an analytical solution is available. Here we use the simulation cell and coordinates shown in Figure 4.3. An initial sinusoidal velocity profile is overlaid on the molecular velocity vectors in a previously equilibrated simulation cell as sketched in Figure 4.3. This two-dimensional configuration in Cartesian coordinates with $v_x(y)$ and $v_y = 0 = v_z$ meshes well with standard MD simulations performed in Cartesian coordinates. Assuming the fluid is relatively incompressible and that there are neither pressure gradients nor external forces, one can combine the equations of continuity and momentum for this configuration into one equation as

$$\rho \frac{\partial v_x}{\partial t} = -\frac{\partial \tau_{yx}}{\partial y} \tag{4.11}$$

where ρ is density, v_x is the velocity in the x direction, t is time, and τ_{yx} is the shear stress.

A constitutive equation relating the shear stress to the viscosity is required to complete the formulation of the boundary-value problem. We consider in development of this TMD method only fluids that can be adequately modeled with either a Newtonian or a linear viscoelastic constitutive equation. Restriction of the method to these two classes of fluid guarantees that the solution of the boundary-value problem is separable, but does not significantly restrict application of the simulation method for the model fluids of interest in this and related work.

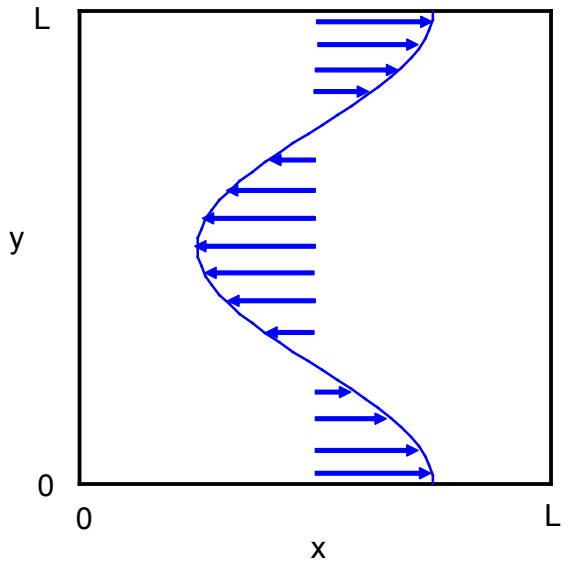

Figure 4.3: Schematic of the simulation cell showing the x and y coordinates with an overlay representation of the initial cosine velocity profile for v_x.

4.3.1 Newtonian Fluid Constitutive Equation

For the geometry depicted in Figure 4.3, the relation between shear stress and shear rate for a Newtonian fluid is

$$\tau = -\eta \frac{\partial v_x}{\partial y} \tag{4.12}$$

where η is viscosity. Insertion of Equation 4.12 into Equation 4.11 gives the working partial differential equation that relates the transient behavior of the velocity to the viscosity:

$$\rho \frac{\partial v_x}{\partial t} = \eta \frac{\partial^2 v_x}{\partial y^2} \tag{4.13}$$

In the TMD method developed here, we use an initial velocity profile of the form

$$v_x(0,y) = v_{max} \cos\left(\frac{2\pi}{L} y\right) \tag{4.14}$$

which exhibits maxima in the velocity, v_{max}, at the cell boundaries in the y direction as

illustrated in Figure 4.3 and conforms to the periodic boundary conditions of the simulation and Neumann-Neumann boundary conditions that require zero shear at $y = 0$ and $y = L$; namely

$$\left(\frac{\partial v_x}{\partial y}\right)\bigg|_{y=0} = 0 = \left(\frac{\partial v_x}{\partial y}\right)\bigg|_{y=L} \tag{4.15}$$

The solution of this boundary value problem is

$$v_x(t,y) = v_{max}\cos\left(\frac{2\pi}{L}y\right)\exp\left[-\frac{\eta}{\rho}\left(\frac{2\pi}{L}\right)^2 t\right] = v_x(0,y)\phi(t) \tag{4.16}$$

where

$$\phi(t) = \exp\left[-\frac{\eta}{\rho}\left(\frac{2\pi}{L}\right)^2 t\right] \tag{4.17}$$

The initial streaming velocity distribution is thus seen to decay exponentially with time t, by the transient function $\phi(t)$. The corresponding MD simulation is performed in a box of length L in the y direction. The streaming velocity given by Equation 4.14 is overlaid on the instantaneous molecular velocities of an initially equilibrated simulation. The exponential decay in time of the velocity profile is tracked, and the viscosity is obtained by matching in a least-squares sense the analytical solution given in Equation 4.16 to the simulated transient data.

A convenient form for $\phi(t)$ that optimizes Equation 4.16 to the simulation values can be derived that uses individual particle positions and velocities instead of a continuous profile, thus avoiding "binning" of molecular velocities and fitting to a velocity profile. The sum of squared residuals is first written as

$$S = \sum_{i=1}^{N}\left[v_{x_i} - \phi(t)v_{max}\cos\left(\frac{2\pi}{L}y_i\right)\right]^2 \tag{4.18}$$

To minimize S, the derivative of S with respect to ϕ is set equal to zero, and the resultant

equation is solved to find the optimum value of ϕ at each t. This gives

$$\phi(t) = \frac{\sum_{i=1}^{N} \frac{v_{x_i}(t)}{v_{max}} \cos\left[\frac{2\pi}{L} y_i(t)\right]}{\sum_{i=1}^{N} \cos^2\left[\frac{2\pi}{L} y_i(t)\right]} \tag{4.19}$$

For large enough values of N and under the assumption that particles are evenly distributed along the y axis, the denominator can be treated as a Riemann sum which can be taken as a definite integral in the limit of small particle spacing, Δy. Thus,

$$\sum_{i=1}^{N} \cos^2\left[\frac{2\pi}{L} y_i(t)\right] = \frac{1}{\Delta y} \int_0^L \cos^2\left[\frac{2\pi}{L} y\right] \mathrm{d}y = \left(\frac{1}{\Delta y}\right)\left(\frac{L}{2}\right) = \frac{N}{2}\,, \tag{4.20}$$

where the orthogonality of the trigonometric cos function has been used to perform the integration. This gives the final expression for the optimized $\phi(t)$ calculated in terms of individual molecular y_i and v_{xi} values at each time step:

$$\phi(t) = \frac{2}{N} \sum_{i=1}^{N} \frac{v_{x_i}}{v_{max}} \cos\left(\frac{2\pi}{L} y_i\right) \tag{4.21}$$

4.3.2 Viscoelastic Constitutive Equation

Keshavarzi et al. [54] suggest that LJ fluids exhibit viscoelastic behavior at higher densities, for example when $\rho^* > 0.7$ where $\rho^* = \rho/\sigma^3$. Here ρ is the number density and σ is the LJ size parameter. Linear viscoelastic fluids can be represented by a number of different models, but all can be rearranged into the form

$$\tau = -\int_{-\infty}^{t} G(t-t')\dot{\gamma}(t')\mathrm{d}t' \tag{4.22}$$

where $G(t-t')$ is the relaxation modulus. For simplicity the Maxwell equation [55] which includes both elastic and viscous effects is used here. For a fluid with flow in the x direction and the velocity gradients in the y direction as in Figure 4.3, the chosen constitutive

equation is

$$\tau_{yx} + \lambda \frac{\partial \tau_{yx}}{\partial t} = -\eta_0 \dot{\gamma}_{yx} \tag{4.23}$$

The variable λ is the relaxation time and η_0 is the viscosity at zero shear. The subscripts on $\dot{\gamma}_{yx}$ indicate the direction in which shear is taking place. If λ is zero, the equation for a Newtonian fluid is returned. This differential equation can be solved to give

$$\tau_{yx} = \int_{-\infty}^{t} \left\{ \frac{\eta_0}{\lambda} \exp\left(-\frac{t-t'}{\lambda} \right) \right\} \dot{\gamma}_{yx}(t') \mathrm{d}t' \tag{4.24}$$

The quantity in brackets is the relaxation modulus. Substitution of Equation 4.24 into Equation 4.11 gives

$$\rho \frac{\partial v_x(t,y)}{\partial t} = \int_{-\infty}^{t} \left[\frac{\eta_0}{\lambda} \exp\left(-\frac{t-t'}{\lambda} \right) \right] \left[\frac{\partial^2 v_x(t',y)}{\partial y^2} \right] \mathrm{d}t' \tag{4.25}$$

This equation simplifies to

$$\frac{\partial \phi(t)}{\partial t} = -\frac{a}{\lambda} \int_{-\infty}^{t} \exp\left[-\frac{(t-t')}{\lambda} \right] \phi(t') \mathrm{d}t' \,, \tag{4.26}$$

where

$$a = \frac{\eta_0}{\rho} \left(\frac{2\pi}{L} \right)^2 \,, \tag{4.27}$$

for the case of a factorable velocity profile of the form

$$v_x(t,y) = \phi(t) v_{max} \cos\left(\frac{2\pi}{L} y \right) \tag{4.28}$$

as used in the TMD simulations. Equation 4.26 can be solved using Laplace transforms for the initial sinusoidal pulse represented by Equation 4.14.

The transform of Equation 4.26 is

$$s\Phi(s) - \phi(0) = -a \left[\frac{1}{1+\lambda s} \right] \Phi(s) \tag{4.29}$$

where $\Phi(s)$ is the Laplace transform of ϕ in terms of the Laplace space variable s.

The inverse transform of Equation 4.29 gives the solution for $\phi(t)$, which can be written in the convenient form

$$\phi(t) = \frac{1}{2}\left[A_- \exp\left(-B_+ t/2\lambda\right) + A_+ \exp\left(-B_- t/2\lambda\right)\right] \tag{4.30}$$

where

$$A_\pm = 1 \pm (1-4a\lambda)^{-1/2} \quad B_\pm = 1 \pm (1-4a\lambda)^{1/2} \quad a = \frac{\eta_0}{\rho}\left(\frac{2\pi}{L}\right)^2 \tag{4.31}$$

As was the case for the Newtonian constitutive equation, Equation 4.21 can be used with the transient velocity data obtained from the simulation to find the optimized values for ϕ, in the least squares sense. These values for $\phi(t)$ are then used to regress the best values for η_0 and λ using Equation 4.30 and 4.31. Although not straightforward, it can be shown that Equation 4.30 is equivalent to Equation 4.17 in the limit as λ approaches zero. This is easily verified with the constitutive equations by taking the limit as λ approaches zero.

4.3.3 Simulation Details

Molecular dynamics simulations were performed for LJ fluids using periodic boundary conditions and the minimum image convention. Pair-wise additivity of the LJ pair potentials was assumed, and the LJ potential was truncated at 3.5σ. A velocity Verlet algorithm was used with a dimensionless time step of $t^* = 0.003$ for all but the two highest temperatures studied; a shorter time step of $t^* = 0.001$ was used for these two temperatures. Although 256 particles were used in the "standard" simulations, additional simulations were performed for higher densities with 512 particles by doubling the simulation cell length in the y direction. These larger simulations were performed to help decouple the two parameters η_0 and λ in Equations 4.30 and 4.31 when analyzing the data using the viscoelastic model. Simulations were made at a large number of state points within the

domain $0.8 < T^* < 4.0$ and $0.05 < \rho^* < 1.0$ as shown in Table 4.3. Here $T^* = kT/\varepsilon$, k is Boltzmann's constant, and T is temperature.

Standard NVT MD simulations were used to create the initially equilibrated starting configurations at each desired temperature and density. These NVT simulations were allowed to equilibrate for 20,000 time steps after which equilibrated configurations were saved at 1000 time-step intervals to create 80 different equilibrated configurations from which to initiate the transient simulations. An instantaneous cosine velocity profile conforming to Equation 4.14 was added to the specific particle velocities of the equilibrated configurations, and standard NVE simulations were then performed allowing the velocity profile to relax. The magnitude of the initial velocity profile was calculated from a specified maximum velocity gradient of $dv_x^*/dy^* = 0.056$ for 256-particle simulations and $dv_x^*/dy^* = 0.028$ for 512-particle simulations. Parametric studies of the shear rate suggested that these values were optimal in producing a clear transient response without producing shear-rate dependent viscosities that can occur at higher shear rates.

Values of $v_x^*(t,y)$ generated by the simulation, such as those shown in Figure 4.4, were collected as a function of time and converted to optimum $\phi(t)$ values using Equation 4.21. A heuristic was used to dynamically determine when to terminate collection of the transient data. The time required for $\phi(t)$ to decay from 0.5 to 0.25 was monitored, and the simulation was continued beyond the $\phi(t) = 0.25$ time for nine times this time interval.

The 80 $\phi(t)$ transient-decay samples were averaged to obtain a smoother data set and ten replicates of these smoother data sets were generated at each state point. A single regression was performed to obtain the predicted viscosity at each state point from the ten replicate data sets (800 transient decays), but separate regressions on the individual replicates were also performed to estimate the standard deviation of the viscosity value. Three examples of fitting the transient ϕ decay to the macroscopic analytical equations for the two different constitutive models, Equations 4.17 and 4.30, are shown in Figure 4.5. At lower densities, roughly $\rho^* < 0.3$, $\phi(t)$ is well represented with the Newtonian model. At

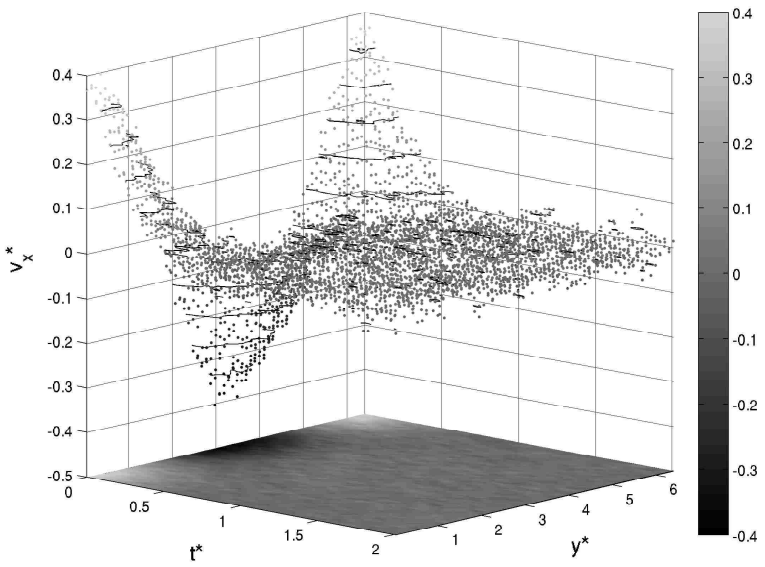

Figure 4.4: Typical decay of the initial velocity profile of the molecules in the simulation cell. This particular response is for $\rho^* = 0.95$ and $T^* = 1.5$.

high densities, $\rho^* > 0.7$, $\phi(t)$ can exhibit a negative region which the viscoelastic model can reproduce but the Newtonian model cannot. At intermediate densities, $0.3 < \rho^* < 0.7$, either model can be used to fit the transient response data. A chi-squared test was used to determine quality of the regressions. In all cases, the observed decay retained the cosine shape conformal to the original applied velocity distribution.

As can be seen from Figure 4.5, $\phi(t)$ for low densities and very short times ($t^* < 0.5$) is inconsistent with the purely exponential decay of the Newtonian model given in Equation 4.17. This short-time inconsistency, prior to the purely exponential decay of $\phi(t)$, correlates roughly with the inverse of the collision frequency that one would calculate for hard spheres with the same value of T^* and ρ^*, suggesting that multiple molecular collisions may be required before the continuum equations apply. For hard spheres, simple kinetic theory [56] predicts $\langle v^* \rangle = \sqrt{8T^*/\pi}$ for the expectation of the velocity and $\langle l^* \rangle = 1/(\sqrt{2}\pi\rho^*)$ for the mean free path. A straightforward estimate of the collision time

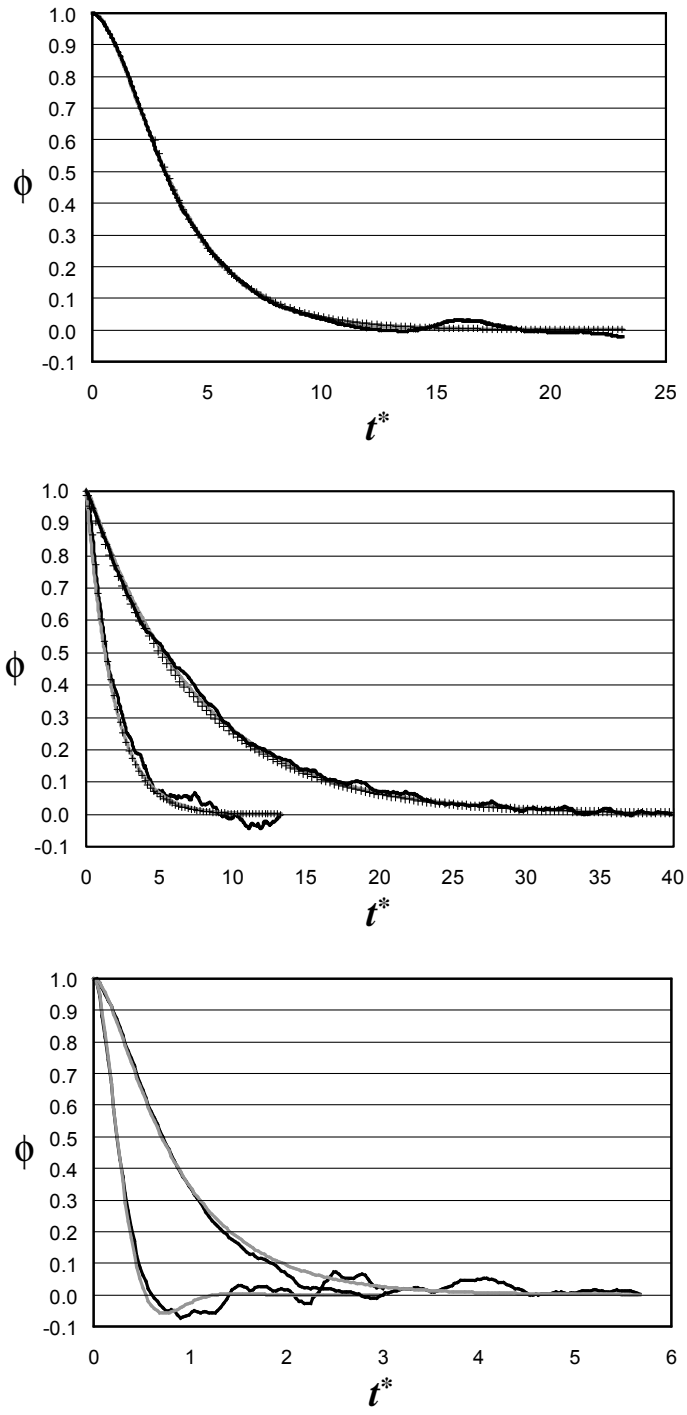

Figure 4.5: Theoretical fit to simulated temporal response $\phi(t)$. The three graphs correspond to $\rho^* = 0.05$, 0.40 and 0.95 all at $T^* = 1.50$. A Newtonian fit is not included for the highest density. Graphed are the simulated data (—), Newtonian fit (+++), and Maxwell fit (—).

is therefore

$$t^*_{coll} = \frac{\langle l^* \rangle}{\langle v^* \rangle} = \frac{1}{4\rho^* \sqrt{\pi T^*}} \tag{4.32}$$

In regressing low-density data with the Newtonian model, we have not used the early simulation data before $1.4t^*_{coll}$ to accommodate this molecular relaxation period. The multiplier of 1.4 is an approximate time when discrepancies between simulation data and the analytical solution appear to fall within the noise, as seen in Figures 4.1 and 4.2. Regressions at higher densities generally did not agree with simulated data, even after the early simulation data was truncated. This lack of effect was expected, because at higher densities the amount of simulation data truncated becomes diminishingly small.

4.4 Results

Table 4.3 shows the regressed dimensionless viscosity values η^* and the calculated standard deviations obtained over the whole ρT domain using the Newtonian constitutive equation and the 256-particle simulation results. Figure 4.6 compares these results to the correlation (based on EMD values) reported by Rowley and Painter [52]. The results of this work are best compared to the results of Rowley and Painter due to the similarities in the simulation details and simulation sizes used. We have also made a similar comparison (not shown) to EMD viscosity values reported by Woodcock [57] for larger simulation cells. That comparison gives the same trend in bias and larger deviations at very large densities near the solid-liquid transition line where the simulated viscosity appears to have a size dependence. Extensive and very accurate EMD simulation results ($\pm 3\%$ for liquid densities, increasing to $\pm 10\%$ for low-density gases) were recently reported by Meier et al. [24]. The largest differences between EMD results of Painter et al., Woodcock, and Meier et al. occur for dense liquids near the solid-liquid equilibrium curve when the number of molecules in the simulation becomes increasingly important.

Table 4.3: Lennard-Jones dimensionless viscosity values η^* and calculated standard deviations (in parenthesis) obtained from TMD simulations using the Newtonian fluid assumption and Equation 4.17. The shaded areas correspond to the liquid-vapor two-phase region and the solid-phase region.

	T*												
ρ*	0.80	1.00	1.10	1.20	1.25	1.30	1.50	1.80	2.10	2.50	3.00	3.50	4.00
0.05			0.104	0.110	0.124	0.126	0.137	0.155	0.182	0.200	0.231	0.273	0.241
			(0.009)	(0.005)	(0.010)	(0.008)	(0.008)	(0.011)	(0.013)	(0.032)	(0.033)	(0.067)	(0.024)
0.10				0.133	0.140	0.143	0.164	0.180	0.204	0.234	0.276	0.313	0.323
				(0.008)	(0.012)	(0.014)	(0.018)	(0.006)	(0.013)	(0.027)	(0.027)	(0.044)	(0.025)
0.15						0.174	0.194	0.222	0.244	0.276	0.321	0.325	0.356
						(0.011)	(0.015)	(0.012)	(0.018)	(0.027)	(0.026)	(0.025)	(0.050)
0.20						0.203	0.220	0.262	0.280	0.311	0.368	0.400	0.399
						(0.013)	(0.006)	(0.016)	(0.022)	(0.022)	(0.036)	(0.048)	(0.075)
0.30							0.297	0.309	0.355	0.372	0.445	0.485	0.460
							(0.020)	(0.014)	(0.041)	(0.046)	(0.038)	(0.056)	(0.072)
0.40							0.410	0.445	0.484	0.489	0.515	0.614	0.622
							(0.039)	(0.054)	(0.032)	(0.041)	(0.066)	(0.091)	(0.082)
0.50						0.559	0.585	0.579	0.628	0.636	0.728	0.770	0.734
						(0.034)	(0.053)	(0.037)	(0.085)	(0.072)	(0.106)	(0.101)	(0.126)
0.60				0.805	0.803	0.804	0.840	0.851	0.878	0.876	0.881	0.945	1.013
				(0.060)	(0.066)	(0.079)	(0.087)	(0.097)	(0.097)	(0.103)	(0.101)	(0.144)	(0.124)
0.70			1.167	1.186	1.237	1.291	1.212	1.200	1.191	1.276	1.341	1.330	1.347
			(0.115)	(0.122)	(0.084)	(0.084)	(0.098)	(0.133)	(0.190)	(0.142)	(0.199)	(0.121)	(0.193)
0.80	2.516	2.436	2.231	2.282	2.272	2.107	1.893	1.843	1.966	2.029	1.780	1.949	1.681
	(0.288)	(0.275)	(0.300)	(0.228)	(0.164)	(0.179)	(0.274)	(0.313)	(0.208)	(0.333)	(0.255)	(0.274)	(0.373)
0.85	4.359	3.639	3.241	3.310	3.142	2.989	2.693	2.550	2.744	2.505	2.256	2.151	2.194
	(0.366)	(0.351)	(0.261)	(0.297)	(0.270)	(0.346)	(0.271)	(0.203)	(0.483)	(0.365)	(0.313)	(0.433)	(0.427)
0.90		5.556	5.252	4.611	4.395	4.541	3.953	3.510	3.184	3.248	2.777	2.959	2.931
		(0.619)	(0.378)	(0.337)	(0.325)	(0.487)	(0.583)	(0.473)	(0.296)	(0.531)	(0.444)	(0.504)	(0.740)
0.95				-	-	-	5.951	5.155	4.566	4.117	3.458	3.309	3.630
							(0.593)	(0.551)	(0.459)	(0.598)	(0.618)	(0.726)	(0.640)
1.00								7.023	6.057	5.451	5.087	4.290	4.137
								(0.876)	(0.717)	(0.809)	(0.987)	(1.051)	(0.963)

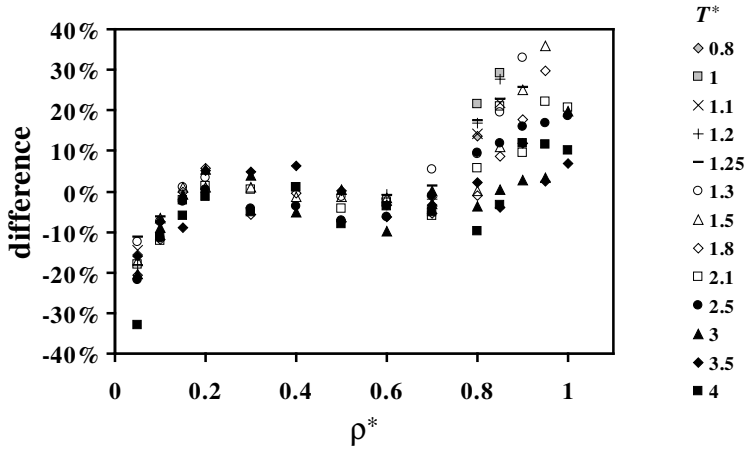

Figure 4.6: Plot of percent difference between TMD results assuming a Newtonian fluid and Painter's EMD results [52].

The assumption of Newtonian behavior yields good agreement of the predicted viscosity values with the EMD results over a large range of fluid conditions ($0.1 < \rho^* < 0.7$) as seen in Figure 4.6, but the systematic deviation between the two methods is evident at dimensionless densities above 0.8. This increasingly positive deviation from the EMD values with increasing density corresponds with the transient behavior of $\phi(t)$ that we observed above a dimensionless density of 0.7, namely, that $\phi(t)$ exhibited increasingly larger negative regions with increasing density for $\rho^* > 0.7$. This behavior is attributed to viscoelastic behavior.

Table 4.4 provides the η^* values and their standard deviations obtained when the simulation results are analyzed in terms of the viscoelastic model; the positive systematic bias observed at the higher densities is removed. Figure 4.7 compares the viscosity values obtained using the viscoelastic model to the same EMD results used in Figure 4.6. Figure 4.8 shows a comparison of the TMD results to the more recent Meier EMD values [24]. Both Figures 4.7 and 4.8 suggest a slightly negative bias of the TMD results relative to the EMD results, but the agreement is well within the uncertainty of the two data sets. Values using the viscoelastic model are not reported for $\rho^* < 0.15$ based on a poor goodness of fit

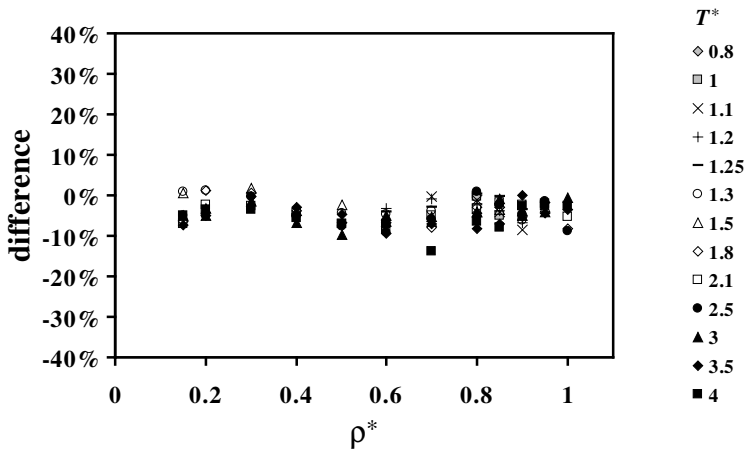

Figure 4.7: Plot of percent difference between TMD results assuming a Maxwell fluid and Woodcock's EMD results [57].

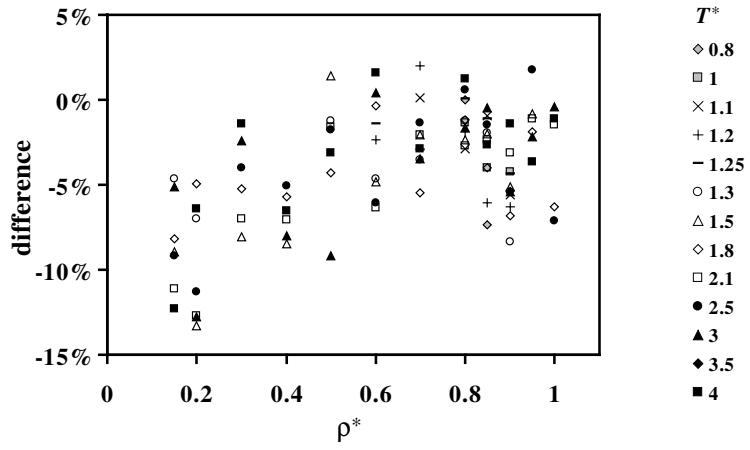

Figure 4.8: Plot of percent difference between TMD results assuming a Maxwell fluid and Meier's EMD results [24].

obtained when simultaneously fitting the response from the 256-and 512-particle systems. Values of the viscosity in the region $0.3 < \rho^* < 0.7$ obtained by both the Newtonian and viscoelastic model were the same within the uncertainty of the simulated results. As mentioned above, use of the viscoelastic model provided very good fits of all of the transient data and is seen to remove the high-density bias.

Table 4.4: Lennard-Jones dimensionless viscosity values η^* and calculated standard deviations (in parenthesis) obtained from TMD simulations using the Maxwell fluid assumption and Equation 4.30. The shaded areas correspond to the liquid-vapor two-phase region and the solid-phase region.

	T*												
ρ*	0.80	1.00	1.10	1.20	1.25	1.30	1.50	1.80	2.10	2.50	3.00	3.50	4.00
0.05			-	-	-	-	-	-	-	-	-	-	-
0.10				-	-	-	-	-	-	-	-	-	-
0.15						0.172 (0.006)	0.193 (0.009)	0.220 (0.010)	0.243 (0.011)	0.277 (0.013)	0.313 (0.018)	0.343 (0.021)	0.370 (0.048)
0.20						0.201 (0.010)	0.219 (0.010)	0.255 (0.009)	0.280 (0.035)	0.299 (0.013)	0.335 (0.016)	0.374 (0.014)	0.392 (0.022)
0.30							0.301 (0.040)	0.332 (0.044)	0.352 (0.021)	0.393 (0.047)	0.422 (0.029)	0.471 (0.039)	0.494 (0.051)
0.40							0.401 (0.013)	0.436 (0.010)	0.457 (0.030)	0.484 (0.055)	0.511 (0.062)	0.571 (0.128)	0.586 (0.079)
0.50						0.548 (0.077)	0.590 (0.142)	0.588 (0.032)	0.615 (0.038)	0.637 (0.150)	0.654 (0.086)	0.732 (0.175)	0.749 (0.106)
0.60				0.788 (0.089)	0.786 (0.092)	0.790 (0.021)	0.801 (0.033)	0.829 (0.102)	0.831 (0.051)	0.854 (0.043)	0.944 (0.243)	0.925 (0.260)	1.008 (0.122)
0.70			1.203 (0.063)	1.214 (0.082)	1.183 (0.137)	1.180 (0.048)	1.164 (0.047)	1.166 (0.142)	1.235 (0.299)	1.221 (0.156)	1.262 (0.080)	1.293 (0.181)	1.314 (0.186)
0.80	2.164 (0.064)	2.025 (0.071)	1.961 (0.077)	1.930 (0.079)	1.948 (0.059)	1.947 (0.085)	1.867 (0.097)	1.833 (0.213)	1.813 (0.124)	1.876 (0.275)	1.802 (0.053)	1.761 (0.432)	1.871 (0.264)
0.85	3.007 (0.106)	2.719 (0.114)	2.598 (0.167)	2.497 (0.105)	2.564 (0.111)	2.480 (0.098)	2.391 (0.103)	2.279 (0.128)	2.260 (0.128)	2.203 (0.159)	2.248 (0.205)	2.127 (0.207)	2.099 (0.549)
0.90		3.801 (0.081)	3.602 (0.146)	3.399 (0.157)	3.482 (0.118)	3.243 (0.191)	3.119 (0.187)	2.868 (0.167)	2.851 (0.175)	2.667 (0.179)	2.602 (0.373)	2.751 (0.199)	2.622 (0.275)
0.95				-	-	-	4.318 (0.244)	3.981 (0.233)	3.705 (0.175)	3.541 (0.240)	3.295 (0.381)	3.165 (0.408)	3.146 (0.746)
1.00								5.178 (0.401)	4.898 (0.282)	4.273 (0.355)	4.236 (0.330)	3.963 (0.264)	3.822 (0.453)

Viscosity predictions show a negative systematic bias in Figures 4.6 at very low densities ($\rho^* < 0.1$). The TMD method is less well suited for prediction of gas viscosities at low density. This is likely because the low (relatively speaking) molecular collision frequency in dilute gases makes momentum transport less easily modeled with the continuum equations. As the density decreases the time frame which is truncated increases, indicating that the large mean free path of molecules influences a greater portion of the response. Additional simulations with longer times and larger system sizes suggest that accurate results can be obtained at dimensionless densities lower than 0.1, but we have not pursued that avenue further because of the decreased efficiency of the method in that region and because the Chapman-Enskog theoretical equations [56] are accurate and easier to use in this density range.

It should be noted that there are three missing entries in Tables 4.3, 4.4, and 4.5 at very high densities near the liquid-solid phase boundary. These values were omitted from these tables because the chi-squared statistics indicated an inability to adequately fit the simulated decay of $\phi(t)$ even with the viscoelastic equations. While the response from either the 256- or 512-particle systems could be fitted individually, both responses could not be simultaneously regressed suggesting an inadequacy in the linear viscoelastic model near the solid-liquid phase boundary. The two sizes of simulation cells were used both to ensure size consistency of the model and to provide good decoupling of the two parameters in the viscoelastic model. Values of the dimensionless viscoelastic relaxation time λ^* obtained and their standard deviations are reported in Table 4.5.

4.5 Conclusion

A TMD method has been developed for efficient prediction of fluid viscosity. The simulation produces transient velocities from an initial cosine velocity profile. These transient velocities are fitted to a theoretical analytical solution of the boundary value problem describing the macroscopic momentum transfer for the geometry and initial condition used in

Table 4.5: Lennard-Jones dimensionless viscosity values λ^* and calculated standard deviations (in parenthesis) obtained from TMD simulations using the Maxwell fluid assumption and Equation 4.30. The shaded areas correspond to the liquid-vapor two-phase region and the solid-phase region.

	T*												
ρ*	0.80	1.00	1.10	1.20	1.25	1.30	1.50	1.80	2.10	2.50	3.00	3.50	4.00
0.05			-	-	-	-	-	-	-	-	-	-	-
0.10				-	-	-	-	-	-	-	-	-	-
0.15						0.501 (0.204)	0.519 (0.199)	0.537 (0.271)	0.426 (0.194)	0.355 (0.091)	0.435 (0.162)	0.343 (0.098)	0.361 (0.221)
0.20						0.459 (0.159)	0.390 (0.243)	0.323 (0.167)	0.337 (0.225)	0.344 (0.122)	0.364 (0.161)	0.369 (0.156)	0.254 (0.138)
0.30							0.232 (0.180)	0.179 (0.170)	0.176 (0.120)	0.125 (0.182)	0.197 (0.089)	0.184 (0.136)	0.162 (0.125)
0.40							0.176 (0.073)	0.154 (0.157)	0.159 (0.117)	0.152 (0.112)	0.119 (0.127)	0.109 (0.147)	0.195 (0.207)
0.50						0.110 (0.114)	0.058 (0.091)	0.080 (0.125)	0.137 (0.071)	0.105 (0.131)	0.070 (0.105)	0.021 (0.101)	0.075 (0.104)
0.60				0.030 (0.064)	0.049 (0.046)	0.092 (0.039)	0.081 (0.051)	0.033 (0.046)	0.068 (0.066)	0.141 (0.095)	0.009 (0.070)	0.033 (0.114)	0.013 (0.106)
0.70			0.039 (0.029)	0.035 (0.034)	0.060 (0.049)	0.062 (0.032)	0.047 (0.041)	0.038 (0.041)	0.044 (0.053)	0.042 (0.044)	0.066 (0.052)	0.068 (0.050)	0.021 (0.072)
0.80	0.120 (0.016)	0.103 (0.032)	0.092 (0.028)	0.074 (0.027)	0.063 (0.036)	0.072 (0.032)	0.073 (0.042)	0.037 (0.038)	0.067 (0.041)	0.022 (0.031)	0.037 (0.029)	0.022 (0.055)	0.036 (0.047)
0.85	0.170 (0.012)	0.131 (0.031)	0.111 (0.018)	0.097 (0.028)	0.080 (0.019)	0.081 (0.018)	0.074 (0.035)	0.066 (0.034)	0.055 (0.021)	0.049 (0.033)	0.037 (0.033)	0.040 (0.051)	0.020 (0.061)
0.90		0.157 (0.022)	0.148 (0.024)	0.126 (0.027)	0.111 (0.023)	0.115 (0.019)	0.091 (0.040)	0.061 (0.024)	0.054 (0.032)	0.058 (0.041)	0.037 (0.042)	0.052 (0.026)	0.040 (0.022)
0.95				-	-	-	0.129 (0.018)	0.115 (0.022)	0.071 (0.028)	0.067 (0.023)	0.037 (0.028)	0.064 (0.028)	0.049 (0.052)
1.00								0.112 (0.025)	0.095 (0.029)	0.085 (0.019)	0.053 (0.024)	0.053 (0.035)	0.045 (0.011)

the simulation. The viscosity is adjusted in this procedure to give the best least-squares fit of the simulation data to the macroscopic equation.

To obtain the macroscopic equation explicit in the viscosity, a constitutive equation is used to relate the stress tensor to the velocity gradient. In this work we have used two different constitutive relations. If the fluid is considered to be Newtonian, the analysis equation is capable of fitting the transient response observed from the simulation only for dimensionless densities less than 0.7. At higher densities, the velocity decay shows a region of velocity reversal indicative of viscoelastic behavior. Correspondingly, the resultant viscosity values obtained from the method agree with previous EMD results in the density range $0.1 < \rho^* < 0.7$. The TMD method as developed here is not recommended for dimensionless densities below 0.1 where the frequency of molecular collisions is low. Increased simulation cell sizes can be used to ameliorate this problem, but this comes at the expense of the efficiency of the method which is one of the method's strongest assets. This does not limit the method because simulations are generally not required in the low-density region where theoretical equations can be used to predict dilute-gas viscosities.

At higher densities, the transient velocity decay is well-represented by the equations obtained using a linear viscoelastic model to relate the shear stress to the velocity gradient. The Maxwell model adequately represents the regions of reversed velocity flow observed in the transient velocity decay for $\rho^* > 0.7$. We have used two cell sizes in our simulations and required the model to adequately fit both transient responses to ensure a decoupling of the two parameters in the viscoelastic model. The resultant viscosity values agree well with EMD results over the density domain $\rho^* > 0.3$ and also with the TMD results obtained using the Newtonian fluid assumption in the region $0.3 < \rho^* < 0.7$. However, the transient responses in the two different size systems could not be fitted simultaneously using the viscoelastic model for three densities along the liquid-solid phase transition line.

The TMD method developed here can be used to rapidly simulate fluid viscosity for dimensionless densities above 0.1. The viscoelastic model can be used for densities above

0.3, but must be used to obtain accurate results at dimensionless densities greater than 0.7. The velocity relaxation in the LJ fluid is very fast and data are collected over a dimensionless time of 10 – 20, corresponding to approximately 20 – 40 ps for Ar. An average of 800 of these velocity relaxations produces a viscosity estimate with an uncertainty of less than 10%.

Chapter 5

Transient Molecular Dynamics Results for Complex Fluid Models

In the last chapter, it was shown that TMD simulations of simple Lennard-Jones molecules produce viscosity values which agree well with other simulation methods over a wide range of state points. The purpose of those comparisons was to validate the simulation procedure itself by benchmarking its results against those of well-established methods for the same simple interaction potential model. While the Lennard-Jones fluid is an important theoretical fluid which can be used to model simple, spherical molecules such as argon and methane, different intermolecular potential models are needed to capture the more complex interactions of most fluids of interest since the molecular structure of these multiatomic fluids is considerably more complex. Consequently, applying the TMD method to these complex models requires further method testing to ensure the system response conforms to the theory.

In addition to the added complexity of the intermolecular interactions, internal degrees of freedom involving vibrations, bond rotations, and angle bending may be part of the intramolecular potential model. The effect of shear on the molecular configurations controlled by these intramolecular interactions is also expected to impact the rheology of the molecules. That is, we expect that there may be need for more flexibility in the response to shear for fluids modeled with more complex molecular potential energies. We therefore included in our testing of the TMD method an additional constitutive equation that

can model additional rheological response beyond that which we found sufficient for the simple LJ fluid treated in Chapter 4.

5.1 Complex Fluid Models

The complexity of potential models used in simulations has been traditionally limited by expensive force calculations that are the core of MD simulations. The early use of MD simulations required very simple intermolecular potential models in accordance with the computational power of the day. The hard-sphere fluid played a dominant role in both theory and computation due to its very simple potential and its amenability to some analytical solutions. The Lennard-Jones model was another primary workhorse in the early development of simulation methods and is still the most widely used model in simulations, though now it is most common to use multiple instances of this potential centered at each atom within the molecule rather than as a single interaction potential with its origin at the molecular center. The term "Lennard-Jones potential" does not identify a unique potential, but simply a function of the form

$$E_{lj} = c_{m,n}\varepsilon\left[\left(\frac{\sigma}{r}\right)^m - \left(\frac{\sigma}{r}\right)^n\right] . \tag{5.1}$$

E_{lj} is the Lennard-Jones potential, $c_{m,n}$ is a coefficient dependent on m and n, σ is the size parameter, ε is the well-depth parameter, r is the distance between sites, m is a positive integer, and n is a positive integer. Common usage associates the Lennard-Jones potential with the 6-12 potential form, where $c_{12,6} = 4$, $m = 12$, and $n = 6$. These simple models can represent only the most basic of molecules, but they serve as important fundamental building blocks of more complex models.

Most complex models are based on a decomposition of the complex molecular potential into simpler interactions. This often involves mathematically separating the forces into Van der Waals, Coulombic, dihedral, bond-vibration, and angle-bending forces; some are seen

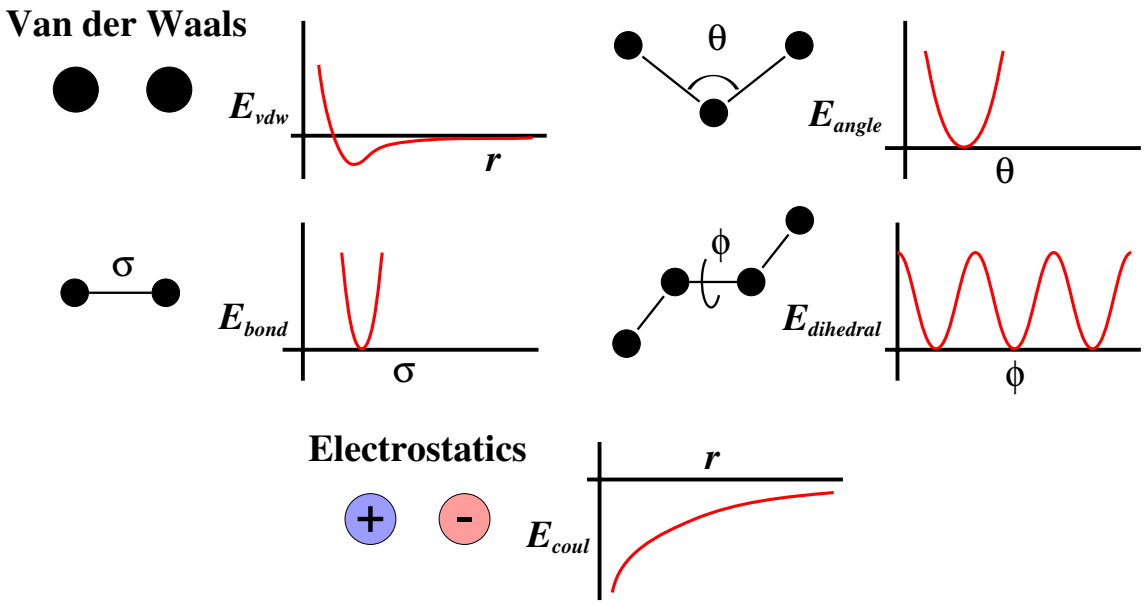

Figure 5.1: Molecular interactions which serve as the building blocks for complex molecular models include van der Waals or dispersion interactions, bond vibrations, angle bending, torsional or dihedral changes, and electrostatics.

in Figure 5.1. Lennard-Jones potentials often serve as the basis for the van der Waals interactions. Often the van der Waals interaction associated with a a single atom or small group such as -CH_2- will be approximated with a LJ potential at the center of the atom or group. Coulombic interactions which account for hydrogen bonding and/or ionic effects are added by placing point charges at different sites in the molecule. Dihedral potentials are added for groups consisting of four or more sites separated by three consecutive bonds. Bond vibrations and angle bending can be modeled explicitly or replaced by rigid bonds and angles through the use of constraints. Bond vibrations and angle bending occur on a much shorter time scale than translational and rotational motion. Inclusion of these modes therefore adds considerable CPU cost to MD simulations and depending on the property of interest may be unnecessary [58]. As multiple potentials are combined into one molecular model, different relaxation modes and constraints affect the simulation results.

An explicit example of a molecular force field is presented as follows

$$E = E_{vdw} + E_{bond} + E_{angle} + E_{dihedral} + E_{coul} \tag{5.2}$$

with individual interactions given by

$$E_{vdw} = \sum_i \sum_{j>i} 4\varepsilon_{ij} \left[\left(\frac{\sigma_{ij}}{r_{ij}} \right)^{12} - \left(\frac{\sigma_{ij}}{r_{ij}} \right)^{6} \right] \tag{5.3}$$

$$E_{bond} = \sum_{bonds} K_r (r - r_{eq})^2 \tag{5.4}$$

$$E_{angle} = \sum_{angles} k_\theta (\theta - \theta_{eq})^2 \tag{5.5}$$

$$E_{dihedral} = k_b \sum_{dihedrals} \sum_{i=0}^{5} a_{\phi,i} \cos^i \phi \tag{5.6}$$

$$E_{coul} = \sum_i \sum_{j>i} \frac{q_i q_j e^2}{r_{ij}} \, . \tag{5.7}$$

The variable r is the bond distance, r_{eq} is the equilibrium bond distance, K_r is a fitting parameter, θ is the bond angle, θ_{eq} is the equilibrium bond angle, k_θ is a fitting parameter, ϕ is the dihedral angle, k_b is Boltzmann's constant, $a_{\phi,i}$ is a fitting parameter, q is the charge on site i or j, and e is the charge of an electron.

The purpose of any molecular force field is to capture the realistic behavior of the molecular systems. The Equations given for E_{vdw}, E_{bond}, E_{angle}, and $E_{dihedral}$ are all approximations to the real potentials. For each of these interactions other alternative potential models are available. The van der Waals interaction has been successfully modeled using a square-well potential, Lennard-Jones potential, and Morse potential in addition to many other proposed models. A simple harmonic potential is shown for the bond vibration potential and bond bending potential, but more complex anharmonic potentials could be used. Bond and angle potentials significantly increase the cost of a simulation due to the shorter time scales on which bond vibrations and angle bending occur. Because shorter time steps

must be taken, the length of time which can be simulated for a certain computational effort is reduced, or the number of time steps in the simulation must be increased to obtain the same statistical accuracy of the resultant properties. Methods have been implemented to address and somewhat mitigate these issues and often are based on multi-time step algorithms [21]. Alternatively the bond lengths and bond angles can be frozen out through the use of constraints allowing larger time steps to be used [21]. The effects of using rigid bonds and angles depend on the property being studied. Most dihedral potentials are given by a sum of cos and sin terms which fit the periodic nature of this potential as the dihedral angle is rotated through 360 degrees. The time scale required by the dihedral potential is of the same magnitude of the van der Waals interaction. The Coulombic interactions given by E_{coul} are based on rigorous physics, and therefore the major competing methods are based on this same potential. Work has been done on reducing the computational expense associated with the Coulombic interactions and has resulted in multiple methods such as the Ewald-sum, Particle-Mesh Ewald, and P^3M methods designed to efficiently solve the fundamental electrostatic problem [36, 59, 60, 61, 62].

The most expensive part of a MD simulation is the explicit force calculation between sites [21]. The calculations of van der Waals interactions scale as $O(N^2)$, where N is the number of interaction sites, if efficiency steps are not taken. Some methods to improve the efficiency include application of a cut-off distance and a neighborhood list. Molecules within a certain cut-off distance are considered neighbors and stored in a list to be used in the force calculation. A neighborhood list can considerably reduce the computation time, particularly for lower densities. Calculations for bond potentials, angle bending potentials, and dihedral potentials scale linearly with the number of interaction sites $O(N)$. Explicit bond vibrations and angle bending unfortunately require shorter time steps than the van der Waals force calculations. This is often ameliorated by only performing bond vibration and angle bending calculations for a certain number of short time steps between larger time steps in which the full force calculation is done.

Dealing with the Coulombic interactions can also be expensive and depends on the method used but can be reduced to order $O(N \log N)$. Because the Coulombic interaction is a long-range interaction, it cannot be truncated for the box sizes used in MD simulations without excessive error. In contrast, van der Waals interactions are often truncated on the order of 13 Å. For the case of a cubic simulation cell with periodic boundary conditions the Coloumbic potential is modified slightly to

$$E_{coul} = \frac{1}{2} \sum_{i=1}^{N} \sum_{j=1}^{N} \sum_{\mathbf{n} \in \mathbb{Z}^3}^{\prime} \frac{q_i q_j e^2}{|\mathbf{r}_{ij} + \mathbf{n}L|} \tag{5.8}$$

The prime indicates that when $i = j$ the $\mathbf{n} = \{0,0,0\}$ term is omitted. This slow converging series is the subject of more efficient methods such as the Ewald Sum and the P^{3}M methods. These more efficient methods split the Coulombic potential into two parts with a splitting function $f(r)$,

$$\frac{1}{r} = \frac{f(r)}{r} + \frac{1 - f(r)}{r} \, . \tag{5.9}$$

The function $f(r)$ is chosen such that $f(r)/r$ quickly decays in a manner suitable for a spherical cut-off that may be applied with the van der Waals cut-off and $1 - f(r)/r$ will be a mildly varying long range portion which can be accurately approximated with only a few Fourier terms. The most popular methods use the complementary error function for $f(r)$, but many other functions could be used. In addition to separating the Coulombic potential into two parts, the Ewald method uses a Fourier transform when solving the electrostatic Poisson equation. The P^{3}M method similarly splits the potential, but interpolates the point charges on regularly spaced grids to take advantage of the fast Fourier transform [61, 62].

The available computational power and time requirements of the simulation will often limit the type of potential model which may be chosen. Four sets of fairly complete potential models have been developed by two groups, each producing a set used to build atomistic models and another used to build courser models. Jorgenson's group developed the OPLS (Optimized Potentials for Liquid Simulations) and OPLS–AA mod-

els [63, 64, 65, 66, 67]. Siepmann's group developed the TRAPPE and TRAPPE–EH models [68, 69, 70, 71, 72, 73, 74, 75, 76]. All of these are transferable potential models in which the pieces of the molecular potential can be reused to build new molecular models. Because OPLS was developed earlier and is a simpler model set, most viscosity simulation values reported in the literature have used models based on OPLS. Thus the nonbonded or van der Waals interaction potential between two -CH_2- groups is taken to be independent of the molecule in which it appears, and the model (LJ in this case) parameters can be used to represent the interaction between all pairs of -CH_2- groups within the total molecule-molecule force field equations for simulations involving *n*-butane, *n*-pentane, *n*-hexane, and other similar molecules containing -CH_2- groups.

5.2 Theory

Similar to that for a LJ fluid, the TMD method for complex molecules uses the same well-defined macroscopic boundary-value problem for which an analytical solution is available if a viscoelastic constitutive equation is used. A constitutive equation relates the shear rate to the shear stress and determines the particular solution to the boundary value problem. Solutions of a Newtonian constitutive equation and Maxwell constitutive equation to the boundary-value problem and initial conditions presented in sections 4.1 and 4.3 have already been derived in sections 4.3.1 and 4.3.2 and used for the case of a LJ fluid [77]. The Newtonian constitutive equation worked well for lower liquid densities, but failed at high liquid densities. The Maxwell constitutive equation was considered as an extension to the Newtonian equation and worked well for the high density LJ fluid. Unfortunately, simulations of fluids modeled with multiple sites showed the two previous constitutive equations to be inadequate, leading to the consideration of a third constitutive equation, the Jeffreys equation. The Jeffreys equation is also a linear visco-elastic constitutive equation amenable to separation of variables whose solution to the boundary-value problem is presented be-

low which is then compared to the constitutive equations and solutions for Newtonian and Maxwell fluids.

5.2.1 Solution to Jeffreys Equation

An analytical solution to the Jeffreys equation can be obtained for the initial conditions and boundary conditions that we have defined for the TMD simulations. A solution of

$$\rho \frac{\partial v_x}{\partial t} = -\frac{\partial \tau_{yx}}{\partial y} \tag{5.10}$$

in which the Jeffreys constitutive equation

$$\tau_{yx} + \lambda \frac{\tau_{yx}}{\partial t} = -\eta_0 \left(\dot{\gamma}_{yx} + \lambda_2 \frac{\partial \dot{\gamma}_{yx}}{\partial t} \right) \tag{5.11}$$

is used in place of τ_{yx}, subject to the boundary conditions

$$\left(\frac{\partial v_x}{\partial y} \right) \Big|_{y=0} = 0 = \left(\frac{\partial v_x}{\partial y} \right) \Big|_{y=L} \tag{5.12}$$

and the initial condition of

$$v_x(0,y) = v_{max} \cos \left(\frac{2\pi}{L} y \right) \tag{5.13}$$

can be obtained. Here ρ is density, v_x is the velocity in the x direction, t is time, and τ_{yx} is the shear stress.

The solution of the Jeffreys equation in terms of shear stress can be written as

$$\tau_{yx} = \int_{-\infty}^{t} \left[\frac{\eta_0}{\lambda} \left(1 - \frac{\lambda_2}{\lambda} \right) \exp \left(-\frac{t-t'}{\lambda} \right) \dot{\gamma}_{yx}(t') \right] dt' + \frac{\eta_0 \lambda_2}{\lambda} \dot{\gamma}_{yx}(t) \, . \tag{5.14}$$

Combining this with Equation 5.11, one obtains

$$\rho\frac{\partial v_x(t,y)}{\partial t} = \int_{-\infty}^{t}\left[\frac{\eta_0}{\lambda}\left(1-\frac{\lambda_2}{\lambda}\right)\exp\left(-\frac{t-t'}{\lambda}\right)\left(\frac{\partial^2 v_x(t',y)}{\partial y^2}\right)\right]dt' + \frac{\eta_0\lambda_2}{\lambda}\frac{\partial^2 v_x(t,y)}{\partial y^2}\,. \tag{5.15}$$

For the given initial velocity profile

$$v_x(0,y) = v_{max}\cos\left(\frac{2\pi}{L}y\right)\,, \tag{5.16}$$

the equation can be simplified to

$$\frac{\partial\phi(t)}{\partial t} = -\frac{a}{\lambda}\left(1-\frac{\lambda_2}{\lambda}\right)\int_{-\infty}^{t}\exp\left(-\frac{t-t'}{\lambda}\right)\phi(t')dt' - \frac{a\lambda_2}{\lambda}\phi(t) \tag{5.17}$$

where

$$v_x(t,y) = v_{max}\cos\left(\frac{2\pi}{L}y\right)\phi(t) = v_x(0,y)\phi(t)\,. \tag{5.18}$$

A solution can be found through Laplace transforms if $\phi(t) = 0$ for $t < 0$. The Laplace transform of Equation 5.17 is

$$s\Phi(s) - \phi(0) = \frac{a}{\lambda}\left(1-\frac{\lambda_2}{\lambda}\right)\left(\frac{1}{s+\frac{1}{\lambda}}\right)\Phi(s) - \frac{a\lambda_2}{\lambda}\Phi(s)\,. \tag{5.19}$$

The transformed function can be rearranged to give

$$\Phi(s) = \frac{\phi(0)}{2}\left(A_-\frac{1}{s+\frac{B_+}{2\lambda}} + A_+\frac{1}{s+\frac{B_-}{2\lambda}}\right) \tag{5.20}$$

where

$$A_\pm = 1 \pm \frac{1-a\lambda_2}{\sqrt{1+2a\lambda_2+a^2\lambda_2^2-4a\lambda}} \tag{5.21}$$

$$B_\pm = 1 + a\lambda_2 \pm \sqrt{1+2a\lambda_2+a^2\lambda_2^2-4a\lambda} \tag{5.22}$$

$$a = \frac{\eta_0}{\rho}\left(\frac{2\pi}{L}\right)^2 . \tag{5.23}$$

The inverse transform provides the final solution,

$$\phi(t) = \frac{1}{2}\left[A_- \exp\left(-B_+ t/2\lambda\right) + A_+ \exp\left(-B_- t/2\lambda\right)\right] . \tag{5.24}$$

When $\lambda_2 \to 0$ the result clearly becomes that of the Maxwell constitutive equation.

A parametric study for the Jeffreys solution gives a similar response as seen with the Maxwell solution, but shifted along the time axis.

5.2.2 Comparison of Constitutive Equations

The constitutive equations for a Newtonian fluid, Maxwell equation, and Jeffreys equation are

$$\tau_{yx} = -\eta\dot{\gamma} \qquad \text{(Newtonian)} \tag{5.25}$$

$$\tau_{yx} + \lambda\frac{\partial\tau_{yx}}{\partial t} = -\eta_0\dot{\gamma}_{yx} \qquad \text{(Maxwell)} \tag{5.26}$$

$$\tau_{yx} + \lambda\frac{\partial\tau_{yx}}{\partial t} = -\eta_0\left(\dot{\gamma}_{yx} + \lambda_2\frac{\partial\dot{\gamma}_{yx}}{\partial t}\right) \qquad \text{(Jeffreys)} \tag{5.27}$$

In all three equations τ_{yx} is the shear stress or the yx component of the stress tensor, $\dot{\gamma}_{yx}$ is the shear rate, and η is the viscosity. In the Maxwell equation and Jeffreys equation η_0 is the zero-shear-rate viscosity and it is analogous to the Newtonian viscosity. The λ term is a relaxation time. The λ_2 term is a retardation time. As the relaxation time increases the fluid takes longer to respond to changes in velocity gradients (analogous to a spring constant). As the retardation time increases, the fluid shows greater resistance to changes in velocity gradients (analogous to a damping constant). If the relaxation time is zero then the retardation term cannot be uncoupled from the viscosity term.

Because each constitutive equation is a linear viscoelastic constitutive equation, each has a solution of the form

$$v_x(t,y) = v_{max}\cos\left(\frac{2\pi}{L}y\right)\phi(t) = v_x(0,y)\phi(t) \tag{5.28}$$

where $\phi(t)$ has a functional form specific to the constitutive equation. In each instance values of $\phi(t)$ are regressed from the simulation at specific values of t using

$$\phi(t) = \frac{2}{N}\sum_{i=1}^{N}\frac{v_{x_i}}{v_{max}}\cos\left(\frac{2\pi}{L}y_i\right). \tag{5.29}$$

The solutions for each constitutive equation are repeated below. For the Newtonian fluid the solution is

$$\phi(t) = \exp(-at) \tag{5.30}$$

where

$$a = \frac{\eta}{\rho}\left(\frac{2\pi}{L}\right)^2. \tag{5.31}$$

For the Maxwell constitutive equation the solution is

$$\phi(t) = \frac{1}{2}\left[A_-\exp\left(-B_+t/2\lambda\right) + A_+\exp\left(-B_-t/2\lambda\right)\right] \tag{5.32}$$

where

$$A_\pm = 1 \pm (1-4a\lambda)^{-1/2} \tag{5.33}$$

$$B_\pm = 1 \pm (1-4a\lambda)^{1/2} \tag{5.34}$$

$$a = \frac{\eta_0}{\rho}\left(\frac{2\pi}{L}\right)^2. \tag{5.35}$$

For the Jeffreys constitutive equation the solution is

$$\phi(t) = \frac{1}{2}\left[A_-\exp\left(-B_+t/2\lambda\right) + A_+\exp\left(-B_-t/2\lambda\right)\right] \tag{5.36}$$

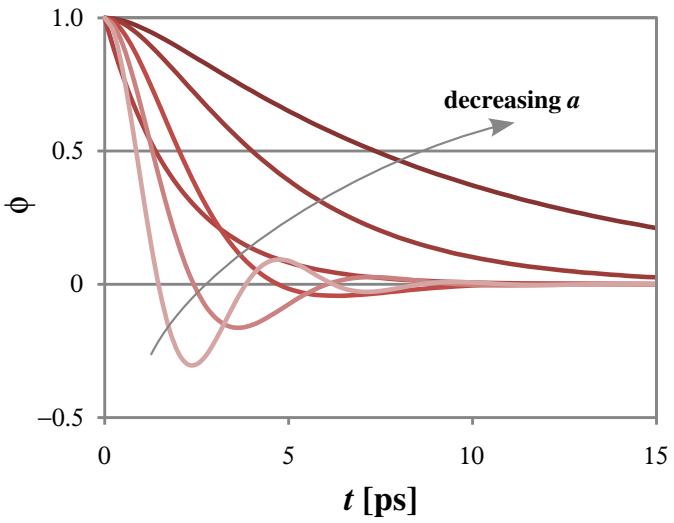

Figure 5.2: The response of $\phi(t)$ for a Maxwell fluid when $\lambda_1 = 1.0$ ps and $a = 0.1$, 0.2, 0.5, 1.0, and 2.0 ps^{-1}. Smaller values of a correspond to diminished oscillations, slower decay and a darker color.

where

$$A_{\pm} = 1 \pm \frac{1 - a\lambda_2}{\sqrt{1 + 2a\lambda_2 + a^2\lambda_2^2 - 4a\lambda}} \tag{5.37}$$

$$B_{\pm} = 1 + a\lambda_2 \pm \sqrt{1 + 2a\lambda_2 + a^2\lambda_2^2 - 4a\lambda} \tag{5.38}$$

$$a = \frac{\eta_0}{\rho}\left(\frac{2\pi}{L}\right)^2 . \tag{5.39}$$

Comparing the constitutive equations and solutions to the given boundary value problem, one can see that as $\lambda_2 \to 0$ the Jeffreys solution becomes the Maxwell solution. Similarly for the Maxwell solution the fluid becomes Newtonian as $\lambda \to 0$.

A parametric study of the response curve based on different values of a, λ, and λ_2 is found in Figures 5.2, 5.3 and 5.4. For the simple case of a Newtonian fluid the response is an exponential decay whose rate of decay is determined by a.

The Maxwell solution can be recast from a function of three independent variables into a function of two dimensionless variables. The characteristic shape of the Maxwell solution

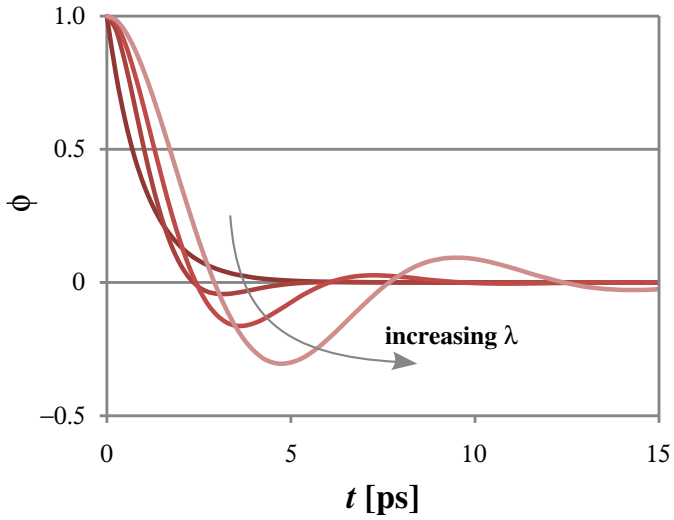

Figure 5.3: The response of $\phi(t)$ for a Maxwell fluid when $a = 1.0$ ps^{-1} and $\lambda = 0.0$, 0.5, 1.0, and 2.0 ps. Larger values of λ correspond to increased oscillations and a lighter color.

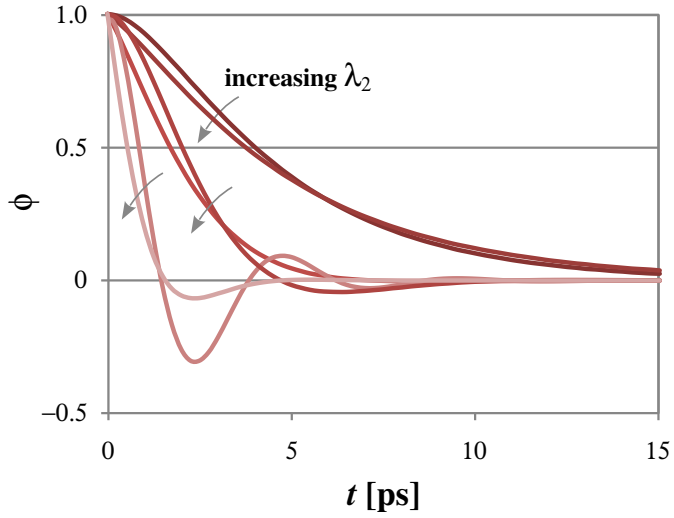

Figure 5.4: The response of $\phi(t)$ for a Jeffreys fluid when $a = 0.2, 0.5, 2.0$ ps^{-1}, $\lambda = 1.0$ ps, and λ_2 is increases from 0.0 to 0.5 ps. An increase in λ_2 casues the intial slope to steepen. Smaller values of a correspond to diminished oscillations, slower decay and a darker color.

only depends on the product $a\lambda$. The domain of interest for the response is dependent on a dimensionless time. The product $a\lambda$ determines the shape of the response curve, while the values of a and/or λ determine the time scale upon which the response occurs. The response can monotonically decay or overshoot with an oscillatory behavior. As a result, for the Maxwell solution response a larger a value will typically lead to a faster decay, however when $a \cdot \lambda > 0.25$ oscillations begin to form in the response curve. The fastest overall rate of decay occurs when $4a\lambda = 1$. Figure 5.2 shows the effect of a upon the response of $\phi(t)$. When oscillations are exhibited, smaller values of a will diminish the number and size of oscillations but not decrease the overall rate of decay for a fixed λ value. Once $4a\lambda$ becomes smaller than 1, the value of a begins to dominate the overall rate of decay. Figure 5.3 shows the effect of λ when a is fixed. When oscillations are present, the overall rate of decay is clearly determined by λ.

For the solution using the Jeffreys equation, λ_2 is the only new factor. The effect of a non-zero λ_2 value causes the initial decay rate to be faster.

The values for $\phi(t)$ obtained by application of Equation 5.29 are used to regress the best values for η, λ, and λ_2 in the least squares sense.

5.3 Simulation Details

MD simulations were performed for the non-polar compounds *n*-butane, isobutane and *n*-hexane in addition to the polar compounds water, methanol, 1-hexanol using united atom models and explicit sites for oxygen atoms and hydrogen atoms attached to oxygen. The SPC/E model for water was employed [78]. The hydrocarbon-backbone torsional potential is modeled with

$$u_{tors}(\phi(t))/k = \sum_{i=0}^{5} a_i \cos^i \phi \tag{5.40}$$

where ϕ is the torsional angle and a_i are coefficients specific to the dihedral angle being modeled. The torsional potentials for the C-C-C-C backbone were taken from the Ryckaert-

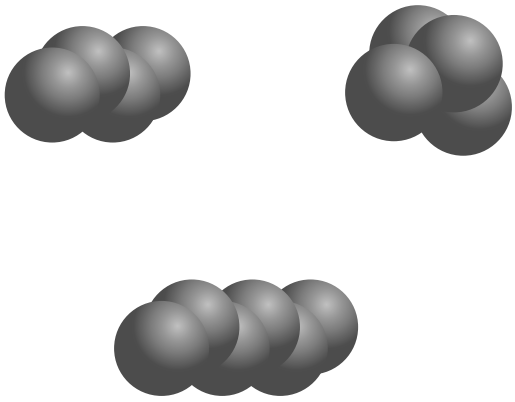

Figure 5.5: Nonpolar site models for *n*-butane, isobutane, and *n*-hexane.

Bellmans potential [79]. Model parameters for the compounds studied can be found in Tables 5.1, 5.2, 5.3, and 5.4. A series of simulations spaced periodically along the phase dome for a saturated liquid were carried out for each compound. The following details were used for these simulations. The LJ site-site interactions were truncated to the smaller of 13 Å or half the length of the smallest dimension of the simulation box. Point charges were treated using the P^3M method [61, 62]. A fourth-order Gear predictor corrector scheme was used to integrate the time steps. The time step was taken to be 1 fs. Simulation sizes of 256, 384, and 512 molecules were run with the box cell length in the *y* direction extended to give aspect ratios of 1, 1.5 and 2, respectively. The multiple cell sizes were used to help decouple the fitting parameters η, λ, and λ_2. The shape of the curves are primarily determined by the values of $a\lambda$ and $a\lambda_2$. Changes in the length of the simulation cell directly impact a, yet leave λ and λ_2 unchanged, resulting in different shapes for the response curve and indicating that multiple lengths should allow better decoupling of the parameters.

In addition to the above simulations, additional simulations reproduced state points of

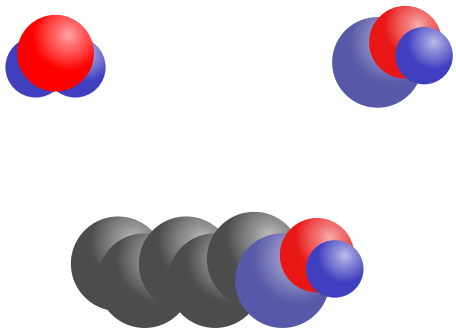

Figure 5.6: Polar site models for water, methanol, and 1-hexanol showing the use of spherical site-site potential models for CH_x, α-CH_2 (connected to the OH group), oxygen, and hydrogen atoms colored by partial charge (blue - positive, gray - neutral, red - negative.

simulated values as reported in the literature, primarily from NEMD simulations. Simulations at state points found in the literature were run under slightly different conditions as noted below. Plots of the simulated state points in relation to the phase dome are given. The saturated liquid part of the phase dome comes from DIPPR®'s saturated liquid density correlations [4] and the saturated vapor curves come from calculations based on the Peng-Robinson equation of state and required constant values from DIPPR®.

5.3.1 *n*-Butane

A number of NEMD values for *n*-butane have been reported in references [45, 46]. TMD simulations at 7 state points duplicating those in the reference were run. A time step of 2.90 fs was used for these simulations, and the Lennard-Jones interactions were truncated at 9.8075 Å. Simulation sizes of 256, 384, and 512 molecules were run with the box cell length in the *y* direction being extended to give aspect ratios of 1, 1.5 and 2, respectively. Additional simulations were run with 125, 187, and 250 molecules with aspect ratios of

Table 5.1: Lennard-Jones site parameters used to simulate *n*-butane, isobutane, *n*-hexane, water, methanol and 1-hexanol.

	site(s)	mass amu	epsilon/k_b K	sigma Å	charge e-	Ref.
n-Butane	CH_2, CH_3	14.5130	72.000	3.923	0.0000	[45, 46]
Isobutane	CH_3, CH	14.5130	72.000	4.020	0.0000	[45, 46]
n-Hexane	CH_2, CH_3	14.3628	72.000	3.923	0.0000	[80]
SPCE	O	15.999	78.197	3.166	-0.8476	[78]
	H	1.008	0.000	0.000	0.4238	
Methanol	CH_3	15.0347	105.200	3.740	0.2650	[36]
	O	15.9994	86.500	3.030	-0.7000	
	H	1.008	0.000	0.000	0.4350	
1-Hexanol	CH_3	15.0347	88.060	3.905	0.0000	
	CH_2	14.0268	59.380	3.905	0.0000	
	CH_2-α	14.0268	59.380	3.905	0.2650	
	O	15.9994	85.550	3.070	-0.7000	
	H	1.008	0.000	0.000	0.4350	

Table 5.2: Bond distances used to simulate *n*-butane, isobutane, *n*-hexane, water, methanol and 1-hexanol.

	Connectivity	Bond Length (Å)	Ref.
n-Butane	C-C	1.53	[45, 46]
Isobutane	C-C	1.53	[45, 46]
n-Hexane	C-C	1.53	[80]
SPCE	O-H	1.00	[78]
Methanol	C-O	1.4246	[36]
	O-H	0.9451	
1-Hexanol	C-C	1.54	
	C-O	1.43	
	O-H	0.99	

Table 5.3: Bond angles used to simulate *n*-butane, isobutane, *n*-hexane, water, methanol and 1-hexanol.

	Connectivity	Angle °	Ref.
n-Butane	C-C-C	109.47	[45, 46]
Isobutane	C-C-C	109.47	[45, 46]
n-Hexane	C-C-C	109.47	[80]
SPCE	H-O-H	109.47	[78]
Methanol	C-O-H	108.53	[36]
1-Hexanol	C-C-C	112.4	
	C-C-O	113.09	
	C-O-H	104.0	

Table 5.4: Dihedral parameters used to simulate *n*-butane, *n*-hexane, and 1-hexanol.

	Connectivity	a_0	a_1	a_2	a_3	a_4	a_5	Ref.
n-Butane	C-C-C-C	1116	1462	-1578	-368	3156	-3788	[45, 46]
n-Hexane	C-C-C-C	1116	1462	-1578	-368	3156	-3788	[80]
1-Hexanol	C-C-C-C	1116	1462	-1578	-368	3156	-3788	
	C-C-C-O	1116	1462	-1578	-368	3156	-3788	
	C-C-O-H	852	2235	196	-3460	47.5	134	

1, 1.5 and 2, respectively. The relationship of these points to the equilibrium coexistence curve is shown in Figure 5.7. The saturation lines or coexistence curves were obtained from the DIPPR® 801 [4] correlation for saturated liquid densities while the saturated vapor curve was obtained from the Peng-Robinson equation of state.

5.3.2 Isobutane

Several NEMD values of viscosity for isobutane are also reported in references [45, 46]. TMD simulations at 9 state points were run duplicating the conditions reported for the NEMD simulations. A time step of 2.97 fs was used in these simulations. The LJ

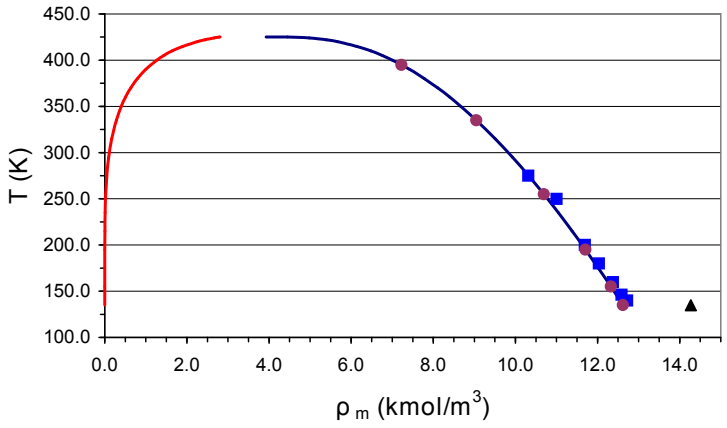

Figure 5.7: Conditions at which the TMD simulations were run for model *n*-butane (●) relative to previously published NEMD simulations (■) [45, 46], the actual *n*-butane saturated vapor (—) and liquid (—) curves [4], and the solid density at the melting point (▲) [4].

interactions were truncated at 10.050 Å. Simulation sizes of 256, 384, and 512 molecules were run with the box cell length in the *y* direction being extended to give aspect ratios of 1, 1.5 and 2, respectively. Additional simulations were run with 125, 187, and 250 molecules with aspect ratios of 1, 1.5 and 2, respectively. As for *n*-butane, the relationship of the isobutane points at which the TMD simulations were performed are shown relative to the equilibrium coexistence curve in Figure 5.8. The saturation lines or coexistence curves were obtained from the DIPPR® 801 [4] correlation for saturated liquid densities while the saturated vapor curve was obtained from the Peng-Robinson equation of state.

5.3.3 *n*-Hexane

NEMD viscosity values for *n*-hexane have been reported in reference [80]. TMD simulations at 9 state points were run, duplicating the conditions reported for the NEMD simulations. In this case, the time step used in the simulations was 2.88 fs. The LJ interactions were truncated at 9.8075 Å. Simulation sizes of 256, 384, and 512 molecules were run with the box cell length in the *y* direction being extended to give aspect ratios of 1, 1.5 and 2, respectively. Additional simulations were run with 125, 187, and 250 molecules with aspect

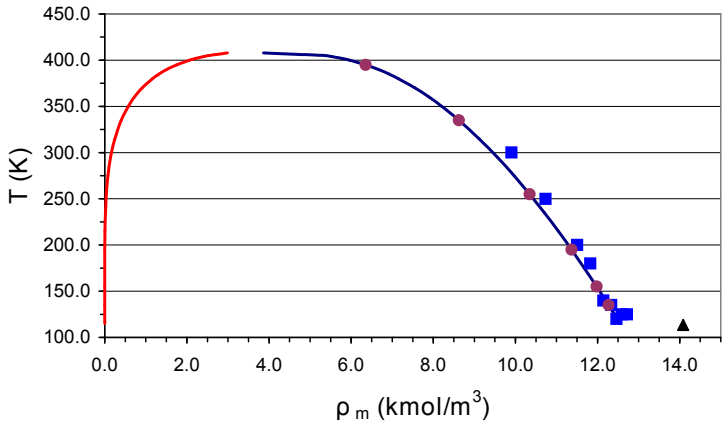

Figure 5.8: Conditions at which the TMD simulations were run for model isobutane (●) relative to previously published NEMD simulations (■) [45, 46], the actual isobutane saturated vapor (—) and liquid (—) curves [4], and the solid density at the melting point (▲) [4].

ratios of 1, 1.5 and 2, respectively. The relationship of these points relative to the saturation curve is shown in Figure 5.9. As for the other fluids studied here, the saturation lines or coexistence curves were obtained from the DIPPR® 801 correlation for saturated liquid densities while the saturated vapor curve was obtained from the Peng-Robinson equation of state.

5.3.4 Water

The extended simple point charge SPC/E developed by Berendsen [78] was used to model water. NEMD simulation values for water using the SPC/E model have been published for three state points corresponding to densities of 55.2642 kmol/m^3, 55.2900 kmol/m^3, and 55.3974 kmol/m^3 [81, 82, 83].

Balasubramanian et al. [81] ran both EMD and NEMD simulations for SPC/E water at a single state point of 303.15 K and 55.2642 kmol/m^3. Reported viscosity values were from simulations with 512 molecules at a density of 0.9956 g/cm^3. A r_{cut} value of 11.4 Å was used and an α value of 0.307 was used for the splitting parameter of the Ewald sum. A time step of 2.5 fs was used for the results of interest. From the NEMD simulations,

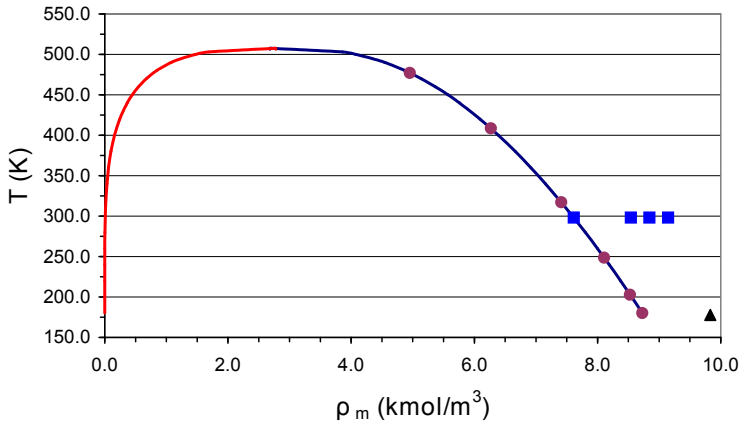

Figure 5.9: Conditions at which the TMD simulations were run for model *n*-hexane (●) relative to previously published NEMD simulations (■) [80], the actual *n*-hexane saturated vapor (—) and liquid (—) curves [4], and the solid density at the melting point (▲) [4].

shear thinning was observed at shear rates of 0.1 ps^{-1} and higher, 5 orders of magnitude higher than an experimentally accessible shear rate. Below this shear rate was a plateau region where viscosity appeared independent of shear rate. The reported viscosity value of 0.66 ± 0.02 mPa·s came from EMD simulations. NEMD simulations with a shear rate of 0.025 ps^{-1} and was assumed to be within the shear-independent plateau region produced a slightly lower value of 0.62 ± 0.02 mPa·s. The experimental value at zero shear is 0.797 ± 0.02 mPa·s.

Wheeler et al. [82] reported a viscosity value for SPC/E water using NEMD simulations at a state point of 0.996 g/cm^3 and 298.15 K. A simulation size of 300 molecules was used with an r_{cut} value of 20.8 Å. Five shear rates of 400, 200, 100, 50, and 16 ns^{-1} were used to extrapolate to zero shear. The value reported was 0.754 ± 0.05 mPa·s. Results were compared to an experimental value of 0.890 ± 0.02 mPa·s [84]. Another viscosity value was reported by Wheeler et al. [83] for SPC/E water that was obtained from EMD simulations at 0.998 g/cm^3 and 298 K. The simulation size was between 3500 and 4000 molecules. The value reported was 0.74 ± 0.05 mPa·s.

TMD simulations were run at the same three conditions at which Wheeler reported

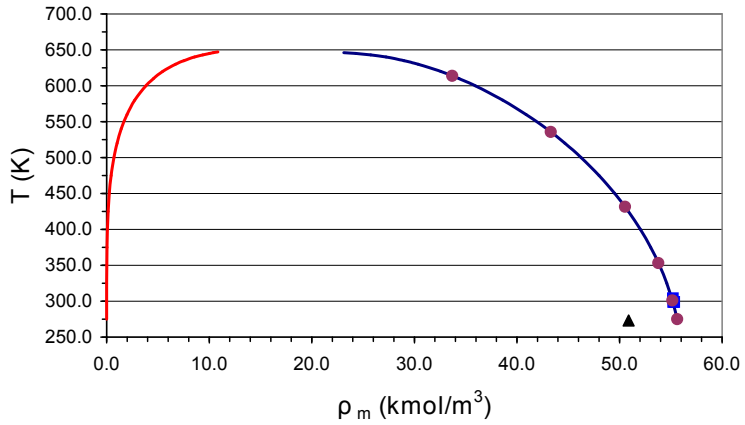

Figure 5.10: Conditions at which the TMD simulations were run for SPC/E water (●) relative to previously published NEMD and EMD simulations (■) [81, 82, 83], the actual water saturated vapor (—) and liquid (—) curves [4], and the solid density at the melting point (▲) [4].

results. The relationship of these points to the equilibrium phase dome for water is shown in Figure 5.10. The phase dome for water was obtained from the Peng-Robinson equation of state.

5.3.5 Methanol

Simulated viscosity values have also been reported in the literature [36] for methanol. TMD simulations at 5 state points duplicating those in this reference were also performed. The time step used was 1.0 fs, and the LJ interactions were truncated at 10.0 Å. Simulation sizes of 256, 384, and 512 molecules were run with the box cell length in the *y* direction being extended to give aspect ratios of 1, 1.5 and 2, respectively. Additional simulations were run with 216, 324, and 432 molecules with aspect ratios of 1, 1.5 and 2, respectively. Some EMD simulation values were reported in the reference to benchmark and corroborate the NEMD values. The relationship of these points to the methanol vapor-liquid equilibrium dome is shown in Figure 5.11. The coexisting densities for methanol were obtained from

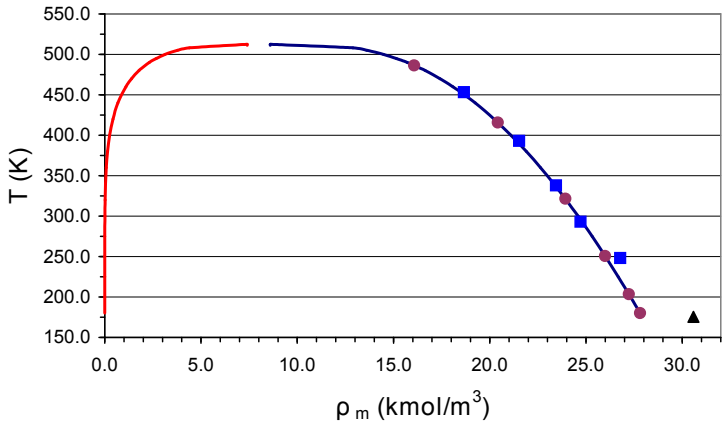

Figure 5.11: Conditions at which the TMD simulations were run for model methanol (●) relative to previously published NEMD simulations (■) [36], the actual methanol saturated vapor (—) and liquid (—) curves [4], and the solid density at the melting point (▲) [4].

the DIPPR® 801 correlation for the liquid branch and from the Peng-Robinson equation of state for the vapor branch.

5.3.6 1-Hexanol

No literature values for simulated viscosity of 1-hexanol have been reported to our knowledge. The saturated liquid curve was again obtained from the DIPPR® 801 correlation, and the vapor curve was obtained from Peng-Robinson equation of state. Six different state points along the saturated liquid curve were chosen at which TMD simulations were performed. These points are shown in relation to the coexistence curve in Figure 5.12.

5.3.7 Additional Simulation Details

All of the initial equilibrated starting configurations for the above model systems were created by starting the simulation at a low density gas, gradually compressing the simulation, and allowing the simulation to equilibrate at the final desired density. Standard NVT

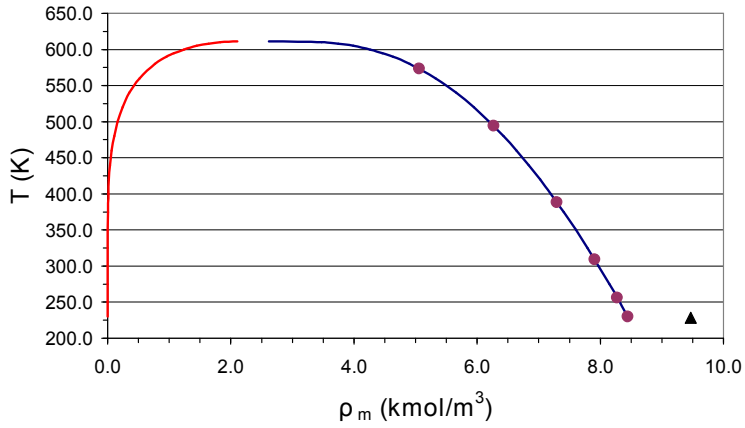

Figure 5.12: Conditions at which the TMD simulations were run for model 1-hexanol (●) relative to the actual 1-hexanol saturated vapor (—) and liquid (—) curves [4], and the solid density at the melting point (▲) [4].

MD simulations were used at the desired densities and temperatures to equilibrate each system for 20,000 time steps. Subsequently, the NVT simulations were allowed to continue while saving configurations every 500 time steps to create 50 equilibrated configurations. An instantaneous cosine velocity profile conforming to Equation 5.18 was applied to the configurations which were allowed to relax as NVE ensembles. The initial magnitude of the velocity profile was chosen to balance the effects of an increased signal to noise ratio with trade-offs in thermal heating and shear-rate effects.

The magnitude of thermal heating was quantified as follows. Application of a given velocity profile adds a known quantity of heat. If the heat capacity of the fluid is known then the average final temperature can be calculated. Even when the heat capacity is not known, the average final temperature can still be bounded. The heat capacity at constant volume of the fluid must be greater than the value $1.5R$ associated with the translational degrees of freedom. An upper bound to the average temperature increase due to thermal heating can be calculated if one uses a lower bound for the heat capacity of $1.5R$. For the TMD simulations the upper bound to the average temperature increase due to thermal

heating is

$$\Delta T_{ub} = \frac{m v_{max}^2}{6 k_b} \tag{5.41}$$

where m is the mass of the molecule, and ΔT_{ub} represents the upper-bound estimation of the temperature increase due to viscous dissipation of the energy into sensible heat. This bounding equation is applicable over the entire range of states and should work well for gases, but becomes much more conservative for liquids because their heat capacities are larger than those for the gas. The values of v_{max} used in all the simulations result in a ΔT_{ub} value of 15K or below. The actual temperature increases were as expected even lower. Even though viscosity has a temperature dependence, the temperature change in the system is assumed small with respect to its effect on viscosity for the simulations run.

The shear-rate effect on viscosity cannot be known a priori unless observed in previous simulations. In NEMD simulations a shear-rate effect on viscosity is seen and seems to increase at increasing density, see Figure 3.2. For the TMD simulations, the shear rate changes along the y axis. A maximum shear rate can be calculated, but even this changes over time as the velocity profile decays with time. At each state point multiple box sizes are used to create different shear-rate profiles. For a given state point, if shear-rate effects are large enough, it is believed that they will be observed when fitting the $\phi(t)$ values simultaneously from the different box sizes.

Larger shear rates will give a larger signal-to-noise response. Based on the magnitude of thermal velocity fluctuations, the expected uncertainty in the fitted response is given by

$$\sigma_{C_N} = \sqrt{\frac{2 k_b T}{m}} \tag{5.42}$$

where m is the mass of a molecule. The signal to noise ratio as given by

$$\frac{signal}{noise} = \frac{v_{max}}{\sigma_{C_N}} \, . \tag{5.43}$$

The $\phi(t)$ values were monitored and fitted by adjusting the viscosity parameters in the appropriate constitutive equations. An original heuristic was used to determine the stopping point of the simulation. This heuristic consisted of observing the time it took for the average signal of several responses to reach 25% of the original value after reaching 50% of the original value. The simulation time was then set to the time it took to decay 75% plus nine times the time from 50% decay to 75% decay. 50 $\phi(t)$ response curves were averaged together to create a smoother response. 20 replicates of these data sets were used at once in the regressions.

As stated above, multiple cell sizes were used to help decouple the fitting parameters η, λ, and λ_2. The shape of the curves are primarily determined by the values of $a\lambda$ and $a\lambda_2$. Changes in the length of the simulation cell directly impact a because it is a function of cell length, yet leave λ and λ_2 unchanged. Simultaneously fitting the results from multiple simulations of various sizes ensures that a is decoupled from the λ and λ_2 parameters. The performed regressions use one set of η, λ, and λ_2 parameters to fit the simulation data of the multiple simulations of various sizes at once.

5.4 Results

The transient velocity responses to the TMD simulations were observed to be more complex than those seen with the LJ model fluid. Because the simulations were for the liquid state it was expected that a visco-elastic effect would be prominent as found for a LJ fluid. However, simply using the solution for the Maxwell constitutive equation given by Equation 5.32 did not adequately fit the response curves. Use of the solution for the Jeffreys constitutive equation given by Equation 5.36 fared much better. As a result all results are reported by using Equation 5.36 to fit the response curves of the simulations.

Some examples of responses seen for *n*-butane are given in Figures 5.13 and 5.14. Figure 5.13 shows the response and fit at medium density while Figure 5.14 shows the response

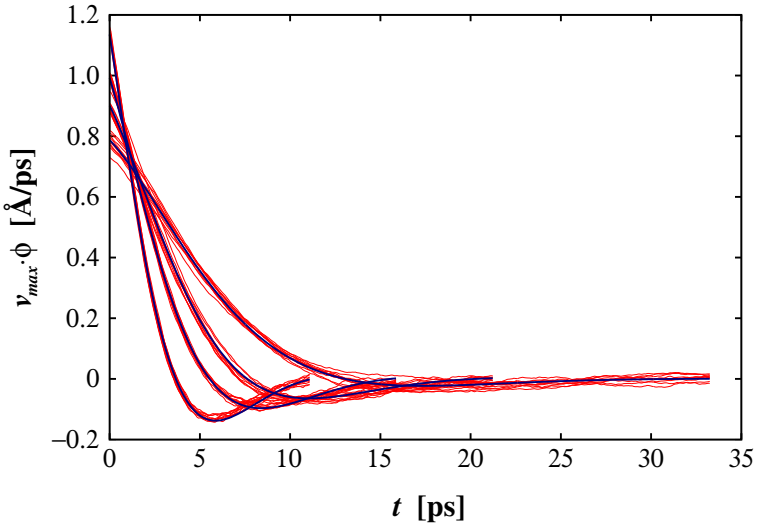

Figure 5.13: Sample responses (—) of *n*-butane and the regressed best fit (—) at a density of 11.689 mol/L and 200 K. Multiple curves correspond to aspect ratios of 1, 1.5, 2, and 3 with a slower response for the larger simulations.

and fit at the highest density simulated for *n*-butane. Within the figure for the medium density, only slight differences between the best fit curve and the simulation response can be detected. Errors in the best fit curve of the higher density response are larger, but are still considered small.

For all compounds, results at low saturated liquid densities (and subsequently higher temperatures) were found to agree with previous literature values and the DIPPR® 801 correlations better than at high densities for saturated liquid viscosity. Results at the lowest densities were within 15% of the DIPPR® 801 correlations. Specifically for *n*-butane and isobutane, results at the lowest densities were within 2% of the reported NEMD simulation values. At higher densities disagreement between TMD results and literature values were found and tended to increase for increasing density for all compounds. Disagreement between the EMD and NEMD literature values and DIPPR®'s correlation also grew larger at increasing density and indicates possible limitations of the molecular models. Unlike results for other compounds, results for water and methanol correlated very well with

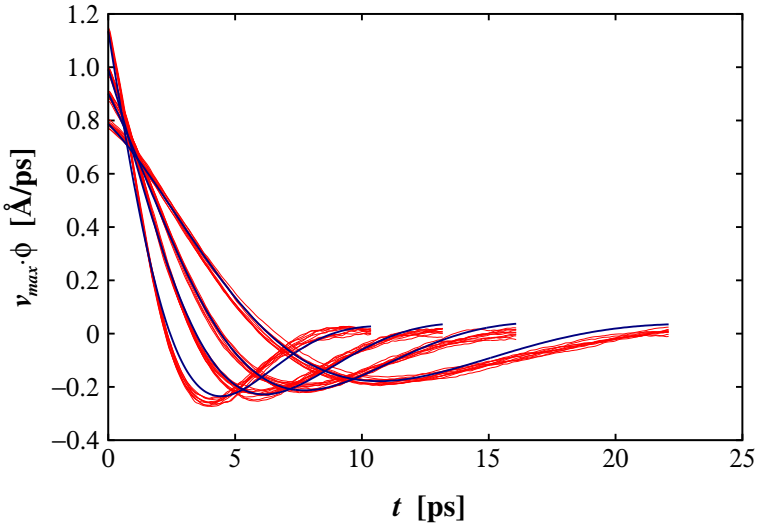

Figure 5.14: Sample simulation responses (—) of *n*-butane and the regressed best fit (—) at a density of 12.721 mol/L and 140 K. Multiple curves correspond to aspect ratios of 1, 1.5, 2, and 3 with a slower response for the larger simulations.

EMD and NEMD literature values at higher densities. Results for water agreed with literature values within 10% while results for methanol at high densities showed less than a 15% discrepancy with literature values. Results from simulation at the highest densities for methanol still showed greater than 50% deviation from the DIPPR® 801 correlation. The largest discrepancy with the DIPPR® 801 correlation occurred for hexanol at dense state points. The accuracy of results for *n*-hexane fell between those associated with *n*-butane and hexanol. Although we have compared simulation values to the reported DIPPR® 801 values, it should be remembered that deviations between experiemntal and simulated values are a result of model inadequacies. Agreement between simulated values using different techniques is a better indicator of the efficacy of the simulation method.

Much of the disagreement for *n*-butane and isobutane at denser state points is a result of the greater shear-rate dependence of viscosity at those conditions. A major difficulty in NEMD simulations is accounting for the shear-rate dependence of viscosity and relating it back to the zero-shear Newtonian viscosity. As already discussed in Section 3.1.4 there

are multiple methods one can try to use to extrapolate to the zero-shear viscosity. Each method may depend on the fluid and state point. The NEMD simulations of *n*-butane and isobutane assumed a linear shear-rate dependence vs. $\dot{\gamma}^{0.5}$. This assumption works well for most of the state points, but it appeared to become deficient for the higher densities. Unfortunately, the TMD simulations at high densities also appear to have some shear-rate dependence. If the responses at the four different simulation aspect ratios (see Figure 5.14) for the highest *n*-butane density are fit individually instead of simultaneously one obtains a viscosity which appears to increase as the shear rates decreases as seen in Figure 5.15. The values of η regressed from these simulations for fixed values of λ and λ_2 appear fairly linear with respect to $\dot{\gamma}_{max}^{0.5}$, as shown in Figure 5.16. Also shown in Figure 5.16 are the NEMD values of η versus the applied steady-state shear rate, $\dot{\gamma}$. The extrapolated value of 1.538 mPa·s still falls below the corresponding NEMD literature value of 2.277 mPa·s. When all the responses were used simultaneously in one regression without accounting for shear-rate dependence, the fitted response appeared to fit the curves well resulting in a viscosity value of 1.409 mPa·s. This can be deceptive because the influence of shear rate on the viscosity does not appear to be pronounced in these responses; however the value obtained is 9% lower than the TMD value obtained through zero-shear extrapolation. The shear-rate dependence of the TMD simulated η is different than the η values from the NEMD simulation. This is because in the TMD simulation, $\dot{\gamma}_{max}^{0.5}$ overstates the average shear in the simulation. The maximum shear rate reported on the *x*-axis is only seen at the start of the simulation and only over a portion of the simulation cell. The very steep slope used to extrapolate the NEMD values is likely to overestimate the zero-shear viscosity; especially since any low-shear plateau in η is severely missed by this extrapolation. Although for these shear-thinning fluids the TMD method does not completely eliminate the need for extrapolation to zero shear for very dense liquids, it does lessen the dependence of the observed η value on the shear rate and may improve the efficiency and accuracy of the extrapolation. As done with NEMD simulations, the best indicator of shear-rate de-

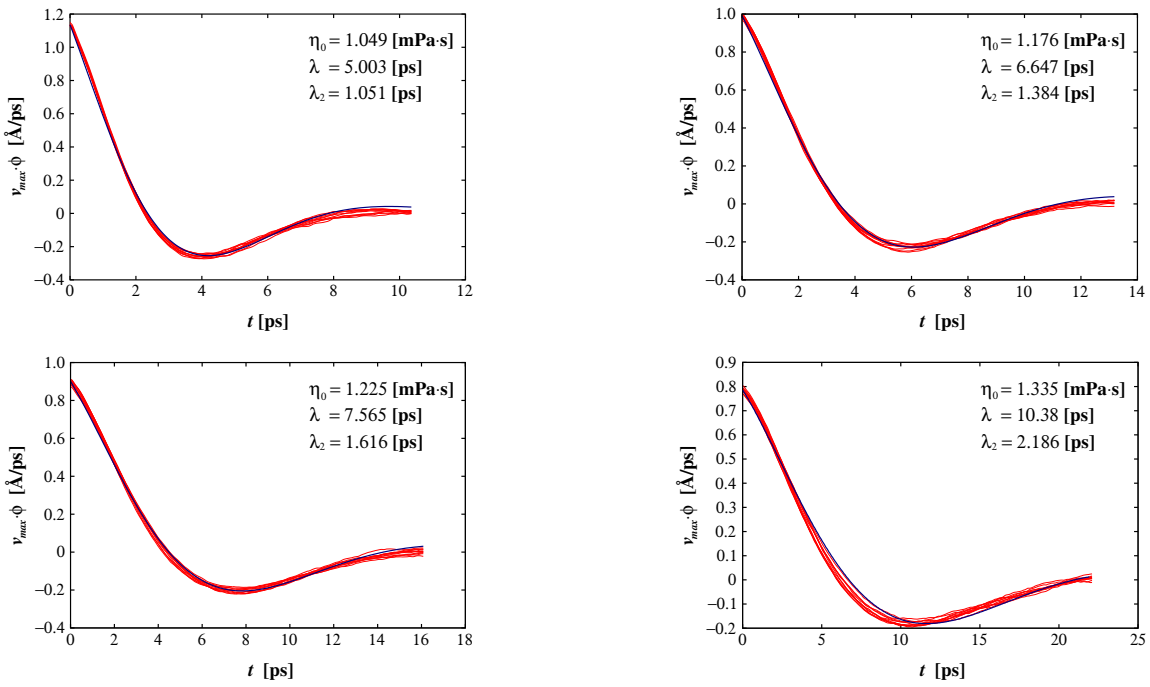

Figure 5.15: Sample responses (—) of *n*-butane and the regressed best fit (—) at a density of 12.721 mol/L and 140 K for four simulation cell sizes. The shear rates decrease and the box length increase from top left, top right, bottom left, to bottom right. The corresponding aspect ratios are 1, 1.5, 2, and 3, respectively.

pendence is to duplicate simulations at different shear rates and see if the viscosity value is significantly affected. When this is done for water, the shear-rate dependence was seen to be negligible. This was expected due to the good agreement of results for water with literature values.

Tables 5.5, 5.6, 5.7, 5.8, 5.9, and 5.10 show results for the regressed viscosity values η, λ, and λ_2. Trends in λ and λ_2 were expected as density increased, but the regressed parameter values did not show any discernable systematic trends. The insensitivities of λ and λ_2 in the regression were likely to blame for the large uncertainties in the regressed values. Any attempt to resolve the behavior of λ and λ_2 using this method would require many more simulations than performed here and was not an objective of this study. Viscosity values have been previously reported from NEMD simulations using the same models for

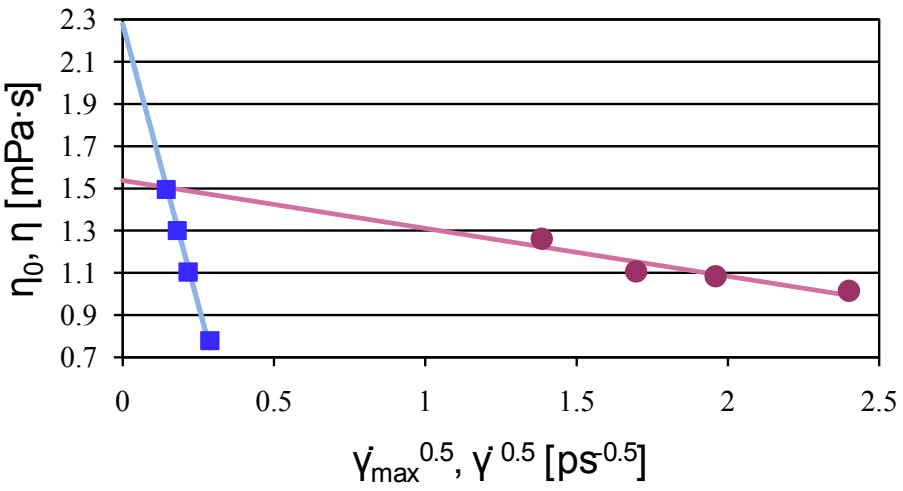

Figure 5.16: Extrapolation to zero-shear rate using regressed *n*-butane viscosity values at a density of 12.721 mol/L and 140 K for four simulation cell sizes assuming a linear shear-rate dependence vs. $\dot{\gamma}^{0.5}$ and compared to the extrapolation of NEMD values. (●) TMD results, (—) TMD zero-shear extrapolation, (■) NEMD results, (—) NEMD zero-shear extrapolation.

n-butane and isobutane in addition to a similar model for *n*-hexane. Results from the TMD method compare favorably with values reported for all three compounds. There is some discrepancy between values for isobutane at higher densities which is likely due to shear-rate dependence of viscosity. The NEMD study also has larger errors due to extrapolation at the higher density values. Comparing results for polar fluids against experimental correlations shows similar trends to those observed for the non-polar fluids. Values agree well for lower-density liquids, but at higher densities the viscosity can be significantly under-predicted. It is believed that the discrepancies with experimental values at higher densities are due to inadequacies in the model. Agreement with NEMD results indicate the TMD method gives correct values for the given model.

It is believed that the Coulombic forces dominate the viscosity for polar molecules. Methanol NEMD results published in the literature suggest that Coulombic interactions became more significant at higher densities [36]. Results were reported for identical simu-

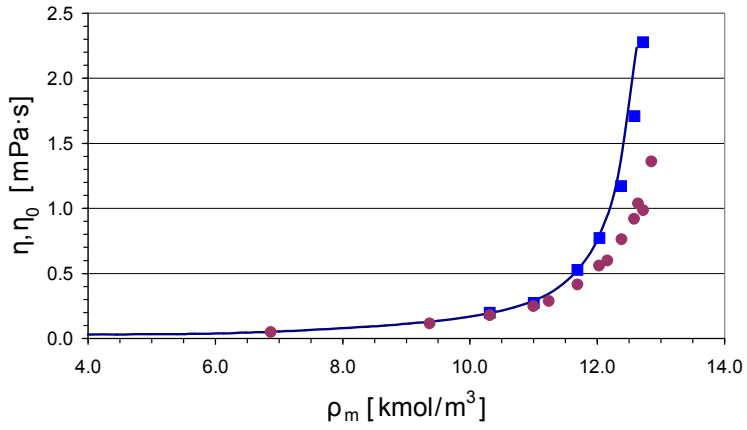

Figure 5.17: Values of *n*-butane viscosity obtained by using the TMD method compared to the DIPPR® 801 correlation and NEMD published results [45, 46]. (●) TMD results, (■) NEMD results, and (—) DIPPR® 801 correlation.

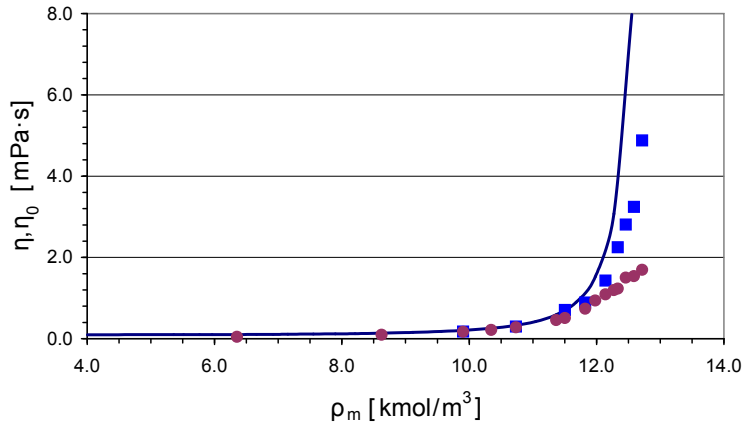

Figure 5.18: Values of isobutane viscosity obtained by using the TMD method compared to the DIPPR® 801 correlation and NEMD published results [45, 46]. (●) TMD results, (■) NEMD results, and (—) DIPPR® 801 correlation.

lations where the Coulombic potential was turned off, leaving only the LJ potentials. Turning off the Coulombic forces resulted in lower viscosity values with increasing deviations as density increased. Whether this shows the significance of including Coloumbic effects or simply the lack of a LJ site on hydrogen is uncertain; however, it makes physical sense that the Coulombic forces could dominate dense liquid behavior.

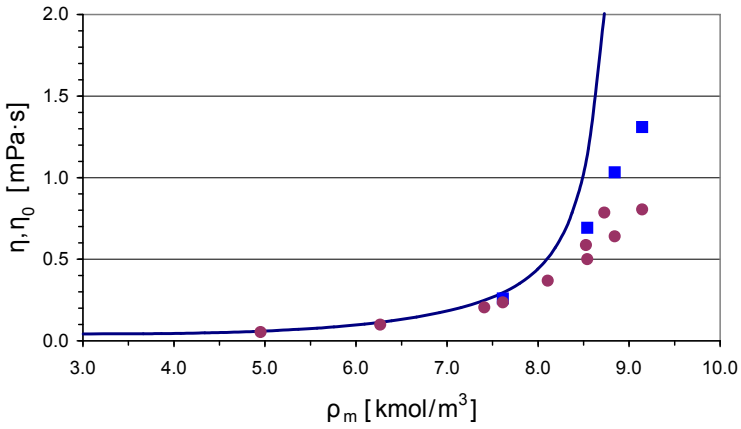

Figure 5.19: Values of *n*-hexane viscosity obtained by using the TMD method compared to the DIPPR® 801 correlation and NEMD published results [80]. (●) TMD results, (■) NEMD results, and (—) DIPPR® 801 correlation.

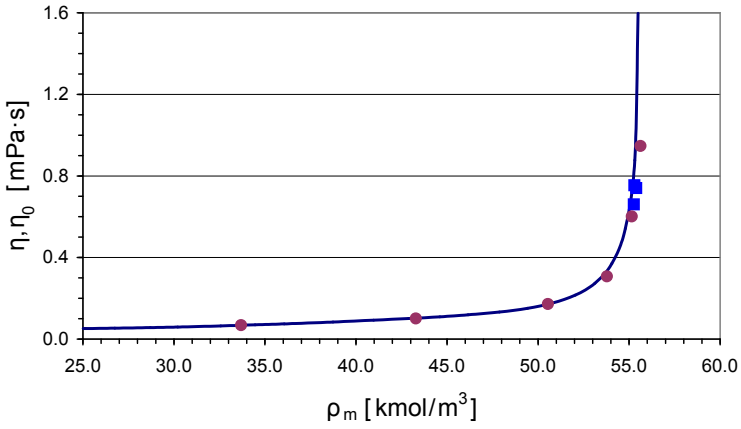

Figure 5.20: Values of water viscosity obtained by using the TMD method compared to the DIPPR® 801 correlation and EMD or NEMD published results [81, 82, 83]. (●) TMD results, (■) EMD or NEMD results, and (—) DIPPR® 801 correlation.

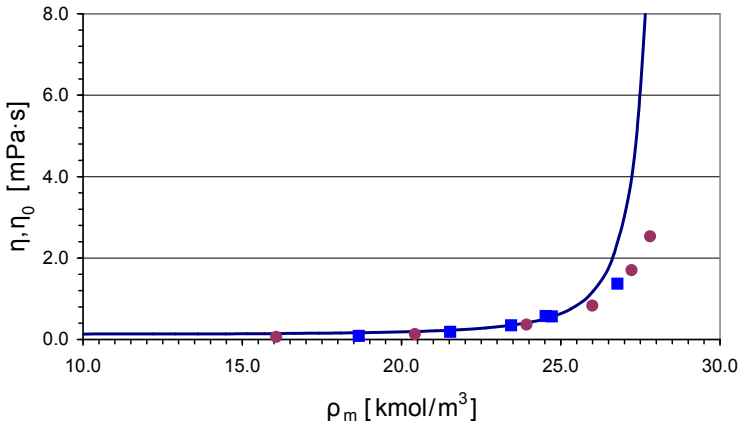

Figure 5.21: Values of methanol viscosity obtained by using the TMD method compared to the DIPPR® 801 correlation, EMD and NEMD published results [36]. (●) TMD results, (■) EMD and NEMD results, and (—) DIPPR® 801 correlation.

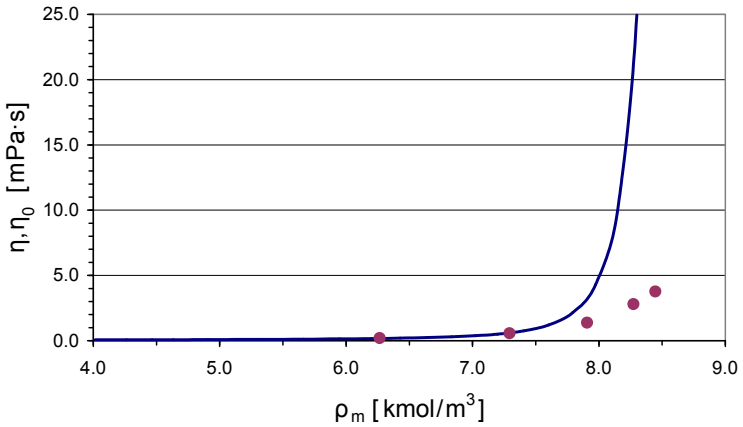

Figure 5.22: Values of 1-hexanol viscosity obtained by using the TMD method compared to the DIPPR® 801 correlation. (●) TMD results, and (—) DIPPR® 801 correlation.

5.5 Conclusions

The TMD method has been shown to give qualitatively correct results for the prediction of viscosity for multi-site models given an appropriate constitutive equation is used. It has been found that responses from multi-site models can be adequately fit when the Jeffreys constitutive equation is chosen. The results are also quantitatively accurate to within 15%

of the literature values and the DIPPR® 801 correlations at the lowest saturated liquid densities. The accuracy of viscosity results at higher densities more heavily depends on the accuracy of the molecular model and the magnitude of the shear-rate dependence. For the small polar molecules water and methanol, the TMD method is quantitatively accurate to within 15% for the given molecular model at all densities. Results for larger molecules such as hexanol at high densities were more than 80% too low in comparison to the DIPPR® 801 correlation.

The TMD method works best at predicting viscosity at low density state points along the saturated liquid viscosity curve. There is less of a concern for shear-rate dependent viscosity and the fluid response becomes more Newtonian. The method works for dense systems, but care must be taken that the appropriate simulation conditions are chosen. The size of the shear rate must not be too large. A smaller shear rate negates potential temperature increases, negates shear-rate viscosity dependence and will create a more Newtonian response in $\phi(t)$.

As stated above, it is important to use an adequate potential model to represent the real molecular systems. The models used for isobutane, *n*-hexane, methanol and 1-hexanol did poorly at high densities in regards to viscosity when compared to experimental values. Simulated viscosities of isobutane, *n*-hexane, methanol and 1-hexanol all were too low with an error greater than 50% at high saturated liquid densities. Results using the *n*-butane molecular model show adequate behavior for dense systems with an error smaller than 50% of the experimental values. The water model performed even better at dense state points with an error smaller than 42% of the experimental values with significant improvement as density decreases. Improved molecular models could significantly improve the quantitative accuracy of the TMD method. In addition, adequately addressing shear-rate dependence remains an issue.

Table 5.5: TMD *n*-butane viscosity results.

ρ	T	$\dot{\gamma}_{max}$				$v_{0,max}$				η_{TMD}	+/-	λ	+/-	λ_2	+/-	η_{DIPPR}	η_{EMD}	η_{NEMD}
kmol/m^3	K									mPa·s		ps		ps		mPa·s	mPa·s	mPa·s
10.31	275.04									0.1908						0.19458		0.1946
11.00	249.98									0.2589						0.29152		0.2713
11.69	200.02	5.618,	3.745,	2.809,	1.873	0.293,	0.256,	0.233,	0.203	0.4290	0.0014	3.5525	0.0398	1.2934	0.0217	0.52502		0.526
		21.759,	14.506,	10.880,	7.253	1.135,	0.992,	0.901,	0.787	0.4270	0.0004	3.3076	0.0106	1.2250	0.0060			
12.03	180.00	5.673,	3.782,	2.836,	1.891	0.293,	0.256,	0.233,	0.203	0.5868	0.0021	4.2667	0.0368	1.2795	0.0154	0.78974		0.77
		21.970,	14.647,	10.985,	7.323	1.135,	0.992,	0.901,	0.787	0.5769	0.0007	4.3466	0.0133	1.3559	0.0056			
12.38	159.84	5.726,	3.818,	2.863,	1.909	0.293,	0.256,	0.233,	0.203	0.9074	0.0053	7.0603	0.0725	1.7214	0.0181	1.37085		1.17
		22.178,	14.785,	11.089,	7.393	1.135,	0.992,	0.901,	0.787	0.8537	0.0018	6.2224	0.0237	1.5939	0.0065			
12.58	146.16	5.758,	3.839,	2.879,	1.919	0.293,	0.256,	0.233,	0.203	1.0610	0.0060	6.7357	0.0632	1.4782	0.0140	2.05108		1.708
		22.300,	14.867,	11.150,	7.433	1.135,	0.992,	0.901,	0.787	1.0563	0.0032	6.9905	0.0338	1.5917	0.0073			
12.72	139.97	5.779,	3.853,	2.889,	1.926	0.293,	0.256,	0.233,	0.203	1.4090	0.0113	8.2797	0.0957	1.5230	0.0144			2.277
		22.381,	14.921,	11.191,	7.460	1.135,	0.992,	0.901,	0.787	1.2341	0.0043	7.3523	0.0383	1.4988	0.0069			

Table 5.6: TMD isobutane viscosity results.

ρ	T	$\dot{\gamma}_{max}$				$v_{0,max}$				η_{TMD}	+/-	λ	+/-	λ_2	+/-	η_{DIPPR}	η_{EMD}	η_{NEMD}
kmol/m^3	K									mPa·s		ps		ps		mPa·s	mPa·s	mPa·s
9.90	300.02									0.1745						0.20427		0.1726
10.74	249.98									0.2793						0.32781		0.2968
11.50	200.02									0.4352						0.69749		0.7057
11.82	180.00									0.5543						1.13197		0.8905
12.14	139.97	5.690,	3.793,	2.845,	1.897	0.293,	0.256,	0.233,	0.203	1.4450	0.0086	7.0413	0.0602	1.2767	0.0094	2.18107		1.427
		22.036,	14.691,	11.018,	7.345	1.135,	0.992,	0.901,	0.787	1.2894	0.0034	6.2310	0.0246	1.2150	0.0045			
12.33	135.00	5.719,	3.813,	2.860,	1.907	0.293,	0.256,	0.233,	0.203	1.7794	0.0139	7.6000	0.0806	1.2013	0.0098	3.64909		2.247
		22.152,	14.768,	11.076,	7.384	1.135,	0.992,	0.901,	0.787	1.5904	0.0053	6.8835	0.0325	1.1887	0.0047			
12.46	120.02	5.739,	3.826,	2.870,	1.913	0.293,	0.256,	0.233,	0.203	2.0609	0.0177	8.0204	0.0896	1.1158	0.0089	5.5914		2.808
		22.228,	14.819,	11.114,	7.409	1.135,	0.992,	0.901,	0.787	1.9026	0.0085	7.3737	0.0439	1.1228	0.0051			
12.59	124.99	5.759,	3.839,	2.879,	1.920	0.293,	0.256,	0.233,	0.203	2.1515	0.0189	7.5044	0.0861	1.0471	0.0088	9.27703		3.241
		22.304,	14.869,	11.152,	7.435	1.135,	0.992,	0.901,	0.787	2.1040	0.0104	7.5356	0.0488	1.1026	0.0051			
12.72	124.99	5.778,	3.852,	2.889,	1.926	0.293,	0.256,	0.233,	0.203	2.3222	0.0201	7.1966	0.0803	0.9427	0.0076			4.876
		22.379,	14.919,	11.189,	7.459	1.135,	0.992,	0.901,	0.787	2.3581	0.0140	7.6535	0.0583	1.0370	0.0054			

Table 5.7: TMD *n*-hexane viscosity results.

ρ	T	η_{TMD}	+/-	λ	+/-	λ_2	+/-	η_{DIPPR}	η_{EMD}	η_{NEMD}
kmol/m^3	K	mPa·s		ps		ps		mPa·s	mPa·s	mPa·s
7.61	298.15	0.2479	0.0004	3.2725	0.0403	1.9284	0.0298	0.29268		0.259
8.54	298.15	0.5368	0.0016	4.0272	0.0415	1.7687	0.0215	1.13514		0.693
8.84	298.15	0.7104	0.0027	3.8050	0.0415	1.5006	0.0188	3.31404		1.032
9.15	298.15	0.9025	0.0036	3.1885	0.0312	1.0702	0.0126	-		1.31
4.95	477.14	0.0536	0.0000	0.4562	0.0651	0.1906	0.0635	0.09447		
6.27	408.57	0.0990	0.0001	1.2905	0.1230	1.0464	0.1183	0.13198		
7.41	317.14	0.2041	0.0005	3.0171	0.0709	1.9524	0.0571	0.24701		
8.11	248.57	0.3684	0.0014	3.9918	0.0654	1.9946	0.0394	0.51597		
8.53	202.86	0.5866	0.0034	3.5201	0.0586	1.3059	0.0273	1.10793		
8.73	180.00	0.7857	0.0057	3.4732	0.0574	0.9870	0.0209	2.00919		

Table 5.8: TMD water viscosity results.

ρ	T	η_{TMD}	+/-	λ	+/-	λ_2	+/-	η_{DIPPR}	η_{EMD}	η_{NEMD}
kmol/m^3	K	mPa·s		ps		ps		mPa·s	mPa·s	mPa·s
33.69	613.93	0.0679	0.0001	0.0000	0.1907	0.0614	0.1814	0.06782		
43.29	535.71	0.1012	0.0003	0.3672	0.1602	0.3203	0.1569	0.10261		
50.55	431.43	0.1720	0.0006	0.1148	0.0328	0.0465	0.0314	0.16969		
50.89	301.07	0.5592	0.0063	0.5030	0.0199	0.1127	0.0119	0.1776		
53.79	353.21	0.3074	0.0019	0.2571	0.0221	0.0936	0.0189	0.3558		
55.15	301.07	0.6011	0.0071	0.4628	0.0203	0.1104	0.0124	0.85303		
55.63	275.00	0.9471	0.0163	0.6888	0.0246	0.1076	0.0095	1.61681		
55.29	298.15							0.99434		0.754
55.26	303.15							0.96049	0.66	
55.40	298.00							1.14002	0.74	

Table 5.9: TMD methanol viscosity results.

ρ	T	η_{TMD}	+/-	λ	+/-	λ_2	+/-	η_{DIPPR}	η_{EMD}	η_{NEMD}
kmol/m^3	K	mPa·s		ps		ps		mPa·s	mPa·s	mPa·s
16.07	486.43	0.0625	0.0000	1.9243	0.0911	1.7980	0.0889	-		
20.42	415.71	0.1311	0.0001	0.7261	0.0221	0.5829	0.0209	-		
23.93	321.43	0.3631	0.0003	1.4960	0.0071	0.7275	0.0046	0.40747		
25.99	250.71	0.8285	0.0014	1.9438	0.0064	0.4287	0.0020	1.16694		
27.22	203.57	1.7001	0.0050	2.9993	0.0123	0.3436	0.0015	3.95216		
27.81	180.00	2.5340	0.0105	3.8658	0.0204	0.3050	0.0013	9.81507		
18.66	453.15							-	0.084	0.0882
21.53	393.15							-	0.198	0.189
23.44	337.85							0.34881	0.378	0.346
24.72	293.15							0.55681	0.588	0.564
26.78	248.15							2.3531	1.388	1.367
24.53	298.15							0.51236		0.574

Table 5.10: TMD hexanol viscosity results.

ρ	T	η_{TMD}	+/-	λ	+/-	λ_2	+/-	η_{DIPPR}	η_{EMD}	η_{NEMD}
kmol/m^3	K	mPa·s		ps		ps		mPa·s	mPa·s	mPa·s
5.06	573.57							0.08736		
6.27	494.29	0.1988	0.0003	3.5095	0.0353	2.1925	0.0251	0.16987		
7.29	388.57	0.5627	0.0013	4.1612	0.0275	1.3625	0.0112	0.59875		
7.91	309.29	1.3751	0.0027	4.2886	0.0138	0.7712	0.0027	3.25832		
8.27	256.43	2.7986	0.0092	5.9529	0.0253	0.5301	0.0019	21.1034		
8.45	230.00	3.7701	0.0130	6.8805	0.0295	0.4613	0.0015	-		

Chapter 6

Conclusions and Recommendations

It has always been a challenge to understand and predict viscosity for the wide range of behaviors seen from the dilute gas to the dense liquid. A theory may work well within a limited scope, but it is extremely difficult to build a comprehensive analytical prediction method. The speed and simplicity of analytical methods are significantly better than for molecular dynamic simulations. Unfortunately the assumptions in conjunction with regressed parameters which occur in an analytical prediction method often cause the method to fail significantly when applied outside the scope in which it was developed and tested. In comparison to analytical prediction methods, simulations allow greater detail to be incorporated and address the complexity of molecular interactions in an explicit, though computationally expensive, manner. With the choice of an appropriate molecular model, a simulation can account for the statistical nature of collisions and their effect upon viscosity. This work leveraged the molecular dynamics method in order to connect the microscopic forces that lead to viscous behavior to the quantitative macroscopic property of viscosity that is important in many chemical engineering applications.

The development of the TMD method and its application to a LJ fluid is able to account for transient behaviors in a methodical manner. The very simple LJ fluid model showed complex behavior over the range of state points. Application of the Newtonian constitutive equation was shown to work well for the low density fluid. Surprisingly, the dense LJ fluid required the more flexible Maxwell constitutive model. The Maxwell constitutive model did exceptionally well at accounting for the liquid response to the transient perturbation.

As a result the TMD results of a LJ fluid were able to predict viscosity within an estimated 10% accuracy.

Extension of the method to multi-site molecules was a natural extension of the TMD method. The inadequacy of the Newtonian or Maxwell constitutive equations was discovered, in contrast to the more general Jeffreys model. The added flexibility of the Jeffreys model allowed the simulation response to be fitted with greater accuracy and overcame some of the problems encountered with under-predicting the viscosity at dense fluid states.

Some of the problems encountered with NEMD simulations such as the shear-rate dependence of viscosity must also be addressed with the TMD method. This was attributed as the main cause for under prediction of viscosity for a given molecular model which worsened as density increased. The most straightforward method to deal with shear-rate dependence is to extrapolate to zero-shear in a manner similar to NEMD simulations, although adding an extrapolation procedure adds to the complexity of the method.

For molecules with strong hydrogen bonding and Coulombic interactions, the TMD method agreed much better at dense state points. The two smallest and most polar molecules, water and methanol, were most accurately modeled for the liquid state. Isobutane and *n*-butane results agreed with literature values at low densities but exhibited problems at higher densities. The larger *n*-hexane and hexanol were reasonably modeled for low densities but showed larger errors at higher densities.

Future work on the TMD method should focus on adequacy of the method at high densities. Incorporation of a shear-rate dependence into the analytic solution of the method should be explored and its effect on the response curve evaluated. More extensive simulations should be preformed to resolve the relaxation time parameters λ and λ_2. The parameters should show systematic trends which can only be seen with additional simulation effort. Due to the significance shear-rate effects, the impact of polar interaction upon shear-rate dependence through Coulombic charges for dense liquids should also be characterized.

Results of the simulations performed in this work have led to insights into the transient responses seen in momentum transport. The degree of non-Newtonian behavior has been characterized and shown to be important on the length and time scales simulated. Further study of the effect of molecular structure on the non-Newtonian behavior of molecules has the potential of greatly increasing the understanding of momentum processes. The potential exists for improving current theories of the dependence of viscous or rheological behavior and the efficacy of current analytical methods.

Appendix A

Laplace Transform

The Laplace Transform is defined as

$$\mathcal{L}\{f(t)\} = \int_0^\infty f(t)e^{-st}\mathrm{d}t = F(s)\ . \tag{A.1}$$

The Laplace Transform is frequently used in signal analysis and control theory. Application of the Laplace Transform frequently relies on tables to get the transform of an equation which is then rearranged and applicable table entries are used to find the inverse transform. Actual direct application of the integral is rarely used in finding the transform and if tractable even more infrequently used to find the inverse transform. The effectiveness of applying the Laplace Transform to find a solution is primarily determined by the availability of pre-computed transforms.

A table of one-sided Laplace transforms is found in Figure A.1.

Table A.1: Laplace transform of commonly used functions

$f(t)$	$\mathcal{L}\{f(t)\}$
$f'(t)$	$sF(s)-f(0^-)$
$f^{(n)}(t)$	$s^nF(s)-s^{n-1}f(0^-)-\cdots-f^{(n-1)}(0^-)$
e^{at}	$F(s-a)$
$e^{-\alpha t}$	$\frac{1}{s+\alpha}$
$(1-e^{-\alpha t})$	$\frac{\alpha}{s(s+\alpha)}$
$\sin(\omega t)$	$\frac{\omega}{s^2+\omega^2}$
$\cos(\omega t)$	$\frac{s}{s^2+\omega^2}$
$e^{\alpha t}\sin(\omega t)$	$\frac{\omega}{(s-\alpha)^2+\omega^2}$
$e^{\alpha t}\cos(\omega t)$	$\frac{s-\alpha}{(s-\alpha)^2+\omega^2}$
$e^{-at}\left[B\cos(\omega t)+\left(\frac{C-aB}{\omega}\sin(\omega t)\right)\right]$	$\frac{Bs+C}{(s+a)^2+\omega^2}$

Appendix B

Equivalent Temporal Response Expressions

The functional form of $\phi(t)$ for a Maxwell or Jeffreys constitutive equation is

$$\phi(t) = \frac{1}{2}\left[A_- \exp\left(-B_+ t/2\lambda\right) + A_+ \exp\left(-B_- t/2\lambda\right)\right] \tag{B.1}$$

with appropriate sub expressions for A_+, A_-, B_+ and B_-. For both the Maxwell and Jeffreys constitutive equations A_+, A_-, B_+ and B_- are either all real or all complex. When all variables are real, the behavior of $\phi(t)$ is the sum of two exponentials. When all variables are complex, the behavior of $\phi(t)$ is a decaying exponential. An alternate form of $\phi(t)$ convenient when the response is a decaying exponential can be found by expressing A_+, A_-, B_+ and B_- as complex variables,

$$A_\pm = c \pm di \tag{B.2}$$

$$B_\pm = (-2\lambda)(p \pm qi) \ . \tag{B.3}$$

Using Euler's formula

$$e^{x+iy} = e^x(\cos y + i \sin y) \ , \tag{B.4}$$

Equation B.1 can be rewritten as

$$\begin{aligned}\phi(t) &= \frac{1}{2}\left[(c-di)\mathrm{e}^{(p+qi)t} + (c+di)\mathrm{e}^{(p-qi)t}\right] \\ &= \frac{1}{2}\left[(c-di)\mathrm{e}^{p\,t}\left(\cos qt + i\sin qt\right) + (c+di)\mathrm{e}^{p\,t}\left(\cos qt - i\sin qt\right)\right] \\ &= \frac{1}{2}\mathrm{e}^{p\,t}\left[2c\cos qt - 2di^2\sin qt\right] \\ &= \mathrm{e}^{p\,t}\left(c\cos qt + d\sin qt\right)\ .\end{aligned} \tag{B.5}$$

B.1 Maxwell Response

Comparing Equations B.2 and B.3 to Equations 5.33 and 5.34, the values of c, d, p, and q for the Maxwell solution are

$$c = 1 \tag{B.6}$$

$$d = \frac{-1}{\sqrt{4a\lambda - 1}} \tag{B.7}$$

$$p = \left(-\frac{1}{2\lambda}\right) \tag{B.8}$$

$$q = \left(-\frac{1}{2\lambda}\right)\sqrt{4a\lambda - 1} \tag{B.9}$$

allowing $\phi(t)$ to be written as

$$\begin{aligned}\phi(t) = \mathrm{e}^{-\frac{1}{2\lambda}t}\Bigg(&\cos\left(\frac{1}{2\lambda}\sqrt{4a\lambda-1}\,t\right) \\ &+ \frac{1}{\sqrt{4a\lambda-1}}\sin\left(\frac{1}{2\lambda}\sqrt{4a\lambda-1}\,t\right)\Bigg)\ .\end{aligned} \tag{B.10}$$

B.2 Jeffreys Response

Comparing Equations B.2 and B.3 to Equations 5.37 and 5.38, the values of c, d, p, and q for the Jeffreys solution are

$$c = 1 \tag{B.11}$$

$$d = \frac{a\lambda_2 - 1}{\sqrt{4a\lambda - 1 - 2a\lambda_2 - a^2\lambda_2^2}} \tag{B.12}$$

$$p = \left(-\frac{1}{2\lambda}\right)(1 + a\lambda_2) \tag{B.13}$$

$$q = \left(-\frac{1}{2\lambda}\right)\sqrt{4a\lambda - 1 - 2a\lambda_2 - a^2\lambda_2^2} \tag{B.14}$$

allowing $\phi(t)$ to be written as

$$\phi(t) = \mathrm{e}^{-\frac{1+a\lambda_2}{2\lambda}t}\left(\cos\left(\frac{1}{2\lambda}\sqrt{4a\lambda - 1 - 2a\lambda_2 - a^2\lambda_2^2}\,t\right) + \frac{1 - a\lambda_2}{\sqrt{4a\lambda - 1 - 2a\lambda_2 - a^2\lambda_2^2}}\sin\left(\frac{1}{2\lambda}\sqrt{4a\lambda - 1 - 2a\lambda_2 - a^2\lambda_2^2}\,t\right)\right). \tag{B.15}$$

B.3 Sinusoidal Oscillations

When the temporal response contains oscillations, the alternate expressions derived above are more convenient when analyzing the behavior of the response. Because the frequency of the sin and cos terms are equal, the weighted sum will be a cosine wave of the same frequency. The magnitude of the wave is given by $\sqrt{c^2 + d^2}$ and the phase shift is $\arctan(d/c)$ for $d \geq 0$ or $\arctan(d/c) + \pi$ for $d < 0$.

For the Maxwell fluid the magnitude is

$$\sqrt{\frac{4a\lambda}{4a\lambda - 1}} \tag{B.16}$$

and the phase shift is

$$\arctan\left(\frac{-1}{\sqrt{4a\lambda - 1}}\right). \tag{B.17}$$

For the Jeffreys fluid the magnitude is

$$\sqrt{\frac{4a\lambda - 4a\lambda_2}{4a\lambda - 1 - 2a\lambda_2 - a^2\lambda_2^2}} \tag{B.18}$$

and the phase shift is

$$\arctan\left(\frac{a\lambda_2 - 1}{\sqrt{4a\lambda - 1 - 2a\lambda_2 - a^2\lambda_2^2}}\right) . \tag{B.19}$$

The effect of λ_2 is to decrease the magnitude of any oscillations and increase the phase shift of the curve to the left. With a plain exponential type decay, λ_2 increases the speed of attenuation.

When oscillations are large, increasing λ_2 quickly reduces the magnitude of the oscillations with only a slight phase shift. As λ_2 increases, the phase shift pushes the response to the left.

It is possible that the same approximate response curve is obtained by increasing λ and λ_2 in proportion such that their influence offsets each other.

B.4 Parameter Estimation by Visual Inspection for the Maxwell Response

Fitting parameters can be approximated by visual inspection of responses of $\phi(t)$ for the solution of a Maxwell fluid. Observed responses are divided into those which have a minimum below zero and those which do not have a minimum below zero.

If a minimum below zero is observed, then a and λ can be reliably estimated. The response is only expected to dip below zero if $a\lambda$ is less than 0.25. The minimum value of ϕ, ϕ_{min}, is observed and the corresponding time, t_{min}, are noted and related to the product $a\lambda$ by

$$a\lambda = 0.25 + \left(\frac{\pi}{2\ln(-\phi_{min})}\right)^2, \quad a\lambda > 0.25 \tag{B.20}$$

The value for λ is then found from

$$\lambda = \frac{t_{min}}{2\pi}\sqrt{4a\lambda - 1}, \quad a\lambda > 0.25\ . \tag{B.21}$$

From the known product $a\lambda$ and λ, a is calculated.

If a minimum below zero is not observed, then the value of a can be approximated by observing the time at which the response has decayed by two-thirds. From

$$\phi = \frac{1}{3} \quad , at \approx 1.1, \quad a\lambda < 0.25 \tag{B.22}$$

the value a is approximated by dividing 1.1 by the time at which ϕ is one-third its original value. The value λ can also be estimated. If the time at which the decay has decayed by 10 percent is noted and divided by the time that it took to decay by two-thirds, then the ratio r can be used to estimate $a\lambda$ from

$$a\lambda \approx -0.1859 + 3.0930r - 16.8233r^2 + 49.875r^3, \quad 0.96 < r < 0.2323, \quad a\lambda < 0.25\ . \tag{B.23}$$

From the known a and product $a\lambda$, λ is calculated. It should be noted that the uncertainty of λ will be considerably greater than that of a.

Appendix C

Non-Linear Regression of Time-Series Data

Application of a least squares fit to an arbitrary function can be done if the Jacobian can be evaluated, sufficient data is available and good initial parameter values are chosen. The Jacobian is a matrix consisting of width p and length n where p is the number of parameters being regressed and n is the number of data points used in the regression. The columns contain the derivative of the function f being fit with respect to the fitting parameters. Each row contains the derivatives evaluated for the specific state of the data point. Each element of the Jacobian is evaluate as $J_{i,j} = \frac{\partial f_i}{\partial x_j}$ where f_i is the value of the function associated with row i and x_j is a fitting parameter associated with column j.

Functional forms used in the non-linear regression for the evaluation of the Jacobian are presented for the solutions of the temporal response corresponding to the Newtonian, Maxwell and Jeffreys constitutive equations.

C.0.1 Newtonian Constitutive Model

The solution of the temporal response for the boundary value problem as applied in the TMD method for a Newtonian constitutive equation is

$$\phi(t) = \exp\left[-\frac{\eta}{\rho}\left(\frac{2\pi}{L}\right)^2 t\right] \tag{C.1}$$

To improve the fit, a pre-exponential factor A is added to the functional form. The function used in the regression is

$$f = A\exp\left[-\frac{\eta}{\rho}\left(\frac{2\pi}{L}\right)^2 t\right] \tag{C.2}$$

The parameters fit in a regression are A and η. The pertinent derivatives with respect to these parameters are found as follows.

$$\begin{aligned}\frac{\partial f}{\partial A} &= \exp\left[-\frac{\eta}{\rho}\left(\frac{2\pi}{L}\right)^2 t\right] \\ \frac{\partial f}{\partial \eta} &= -\frac{t}{\rho}\left(\frac{2\pi}{L}\right)^2 A\exp\left[-\frac{\eta}{\rho}\left(\frac{2\pi}{L}\right)^2 t\right]\end{aligned} \tag{C.3}$$

These derivatives are used in the evaluation of the Jacobian.

C.0.2 Maxwell Constitutive Model

The solution of the temporal response for the boundary value problem as applied in the TMD method for a Maxwell constitutive equation is

$$\phi(t) = \frac{1}{2}\left[A_- \exp\left(-B_+ t/2\lambda\right) + A_+ \exp\left(-B_- t/2\lambda\right)\right] \tag{C.4}$$

where

$$A_\pm = 1 \pm (1-4a\lambda)^{-1/2} \quad B_\pm = 1 \pm (1-4a\lambda)^{1/2} \quad a = \frac{\eta_0}{\rho}\left(\frac{2\pi}{L}\right)^2 \tag{C.5}$$

Allowing the fitting function f to equal $\phi(t)$, we will take the derivatives of this function

with respect to η and λ. First some preliminary derivatives are taken

$$\begin{aligned}
\frac{\partial}{\partial a}\left[(1-4a\lambda)^{-1/2}\right] &= \left(-\frac{1}{2}\right)(1-4a\lambda)^{-3/2}(-4\lambda) &&= 2\lambda\Omega^{-3} \\
\frac{\partial}{\partial \lambda}\left[(1-4a\lambda)^{-1/2}\right] &= \left(-\frac{1}{2}\right)(1-4a\lambda)^{-3/2}(-4a) &&= 2a\Omega^{-3} \\
\frac{\partial}{\partial a}\left[(1-4a\lambda)^{1/2}\right] &= \left(\frac{1}{2}\right)(1-4a\lambda)^{-1/2}(-4\lambda) &&= -2\lambda\Omega^{-1} \\
\frac{\partial}{\partial \lambda}\left[(1-4a\lambda)^{1/2}\right] &= \left(\frac{1}{2}\right)(1-4a\lambda)^{-1/2}(-4a) &&= -2a\Omega^{-1}
\end{aligned} \tag{C.6}$$

where $\Omega = \sqrt{1-4a\lambda}$. Using the above derivatives and allowing $e_p = \mathrm{e}^{-\frac{1}{2\lambda}t[1+\Omega]}$ and $e_n = \mathrm{e}^{-\frac{1}{2\lambda}t[1-\Omega]}$, another preliminary derivative is found to be

$$\begin{aligned}
\frac{\partial f}{\partial a} = &\frac{f_0}{2}\left\{\left[-2\lambda\Omega^{-3}\right] + \left[1-\Omega^{-1}\right]\left[t\Omega^{-1}\right]\right\} e_p \\
&+ \frac{f_0}{2}\left\{\left[2\lambda\Omega^{-3}\right] + \left[1+\Omega^{-1}\right]\left[-t\Omega^{-1}\right]\right\} e_n \,.
\end{aligned} \tag{C.7}$$

The Jacobian elements are

$$\frac{\partial f}{\partial \eta} = \frac{\partial f}{\partial a}\cdot\frac{\partial a}{\partial \eta} = -\frac{t}{\rho}\left(\frac{2\pi}{L}\right)^2 \cdot \frac{\partial f}{\partial a} \tag{C.8}$$

$$\begin{aligned}
\frac{\partial f}{\partial \lambda} = &\frac{f_0}{2}\left\{\left[-2a\Omega^{-3}\right] + \left[1-\Omega^{-1}\right]\left[-\frac{t}{2}[1+\Omega] - a\lambda t\Omega^{-1}\right]\right\} e_p \\
&+ \frac{f_0}{2}\left\{\left[2a\Omega^{-3}\right] + \left[1+\Omega^{-1}\right]\left[-\frac{t}{2}[1-\Omega] + a\lambda t\Omega^{-1}\right]\right\} e_n \,.
\end{aligned} \tag{C.9}$$

With rearrangement the final Jacobian elements are

$$\begin{aligned}
\frac{\partial f}{\partial \eta} = &-\frac{t}{\rho}\left(\frac{2\pi}{L}\right)^2 \frac{f_0}{2}\left\{-2\lambda\Omega^{-3} + t\cdot\Omega^{-1} - t\cdot\Omega^{-2}\right\} e_p \\
&-\frac{t}{\rho}\left(\frac{2\pi}{L}\right)^2 \frac{f_0}{2}\left\{2\lambda\Omega^{-3} - t\cdot\Omega^{-1} - t\cdot\Omega^{-2}\right\} e_n
\end{aligned} \tag{C.10}$$

$$\frac{\partial f}{\partial \lambda} = \frac{f_0}{2}\left\{2a\Omega^{-3} + \frac{a}{b}t(\Omega^{-2} - \Omega^{-1}) + \frac{1}{2}t\cdot\Omega^{-1} - \frac{1}{2}t\cdot\Omega\right\}e_p \\ + \frac{f_0}{2}\left\{-2a\Omega^{-3} + a\lambda t(\Omega^{-2} + \Omega^{-1}) - \frac{1}{2}t\cdot\Omega^{-1} + \frac{1}{2}t\cdot\Omega\right\}e_n\,. \tag{C.11}$$

C.0.3 Jeffreys Constitutive Model

The fitting function used for the Jeffreys model is Equation 5.36. The derivative of this function will be taken with respect to a, λ_1 and then λ_2. If we redefine Ω as $\Omega = \sqrt{1+2a\lambda_2+a^2\lambda_2^2-4a\lambda_1}$, then the preliminary derivatives are

$$\begin{aligned}
\frac{\partial}{\partial a}\left[\Omega^{-1}\right] &= \left(-\frac{1}{2}\right)\left(1+2a\lambda_2+a^2\lambda_2^2-4a\lambda_1\right)^{-3/2}\left(2\lambda_2+2a\lambda_2^2-4\lambda_1\right) \\
&= -\left(\lambda_2+a\lambda_2^2-2\lambda_1\right)\Omega^{-3} \\
\frac{\partial}{\partial \lambda_1}\left[\Omega^{-1}\right] &= \left(-\frac{1}{2}\right)\left(1+2a\lambda_2+a^2\lambda_2^2-4a\lambda_1\right)^{-3/2}(-4a) \\
&= 2a\Omega^{-3} \\
\frac{\partial}{\partial \lambda_2}\left[\Omega^{-1}\right] &= \left(-\frac{1}{2}\right)\left(1+2a\lambda_2+a^2\lambda_2^2-4a\lambda_1\right)^{-3/2}\left(2a+2a^2\lambda_2\right) \\
&= -\left(a+a^2\lambda_2\right)\Omega^{-3}
\end{aligned} \tag{C.12}$$

$$\begin{aligned}
\frac{\partial}{\partial a}\left[\Omega\right] &= \left(\frac{1}{2}\right)\left(1+2a\lambda_2+a^2\lambda_2^2-4a\lambda_1\right)^{-1/2}\left(2\lambda_2+2a\lambda_2^2-4\lambda_1\right) \\
&= \left(\lambda_2+a\lambda_2^2-2\lambda_1\right)\Omega^{-1} \\
\frac{\partial}{\partial \lambda_1}\left[\Omega\right] &= \left(\frac{1}{2}\right)\left(1+2a\lambda_2+a^2\lambda_2^2-4a\lambda_1\right)^{-1/2}(-4a) \\
&= -2a\Omega^{-1} \\
\frac{\partial}{\partial \lambda_2}\left[\Omega\right] &= \left(\frac{1}{2}\right)\left(1+2a\lambda_2+a^2\lambda_2^2-4a\lambda_1\right)^{-1/2}\left(2a+2a^2\lambda_2\right) \\
&= \left(a+a^2\lambda_2\right)\Omega^{-1}
\end{aligned} \tag{C.13}$$

Using the above derivatives and redefining e_p and e_n as $e_p = \mathrm{e}^{-\frac{1}{2\lambda_1}t[1+ac+\Omega]}$ and $e_n =$

$e^{-\frac{1}{2\lambda_1}t[1+ac-\Omega]}$ where Ω was redefined above, then with rearrangement we can evaluate the Jacobian elements to be

$$\begin{aligned}
\frac{\partial f}{\partial a} &= \frac{f_0}{2}\left\{\left[\frac{\lambda_2}{\Omega}+(1-a\lambda_2)\frac{(\lambda_2+a\lambda_2^2-2\lambda_1)}{\Omega^3}\right]\right. \\
&\qquad \left.+\left[1-\frac{1-a\lambda_2}{\Omega}\right]\left[-\frac{1}{2\lambda_1}t\left(\lambda_2+\frac{\lambda_2+a\lambda_2^2-2\lambda_1}{\Omega}\right)\right]\right\}e_p \\
&\quad +\frac{f_0}{2}\left\{\left[-\frac{\lambda_2}{\Omega}-(1-a\lambda_2)\frac{(\lambda_2+a\lambda_2^2-2\lambda_1)}{\Omega^3}\right]\right. \\
&\qquad \left.+\left[1+\frac{1-a\lambda_2}{\Omega}\right]\left[-\frac{1}{2\lambda_1}t\left(\lambda_2-\frac{\lambda_2+a\lambda_2^2-2\lambda_1}{\Omega}\right)\right]\right\}e_n \\
&= \frac{f_0}{2}\left\{\frac{\lambda_2}{\Omega}+\frac{C_2}{\Omega^3}-\frac{t}{2\lambda_1}\left(\lambda_2+\frac{C_1}{\Omega}-\frac{C_2}{\Omega^2}\right)\right\}e_p \\
&\quad +\frac{f_0}{2}\left\{-\frac{\lambda_2}{\Omega}-\frac{C_2}{\Omega^3}-\frac{t}{2\lambda_1}\left(\lambda_2-\frac{C_1}{\Omega}-\frac{C_2}{\Omega^2}\right)\right\}e_n
\end{aligned} \tag{C.14}$$

where $C_1 = 2a\lambda_2^2 - 2\lambda_1$ and $C_2 = 2a\lambda_1\lambda_2 + \lambda_2 - 2\lambda_1 - a^2\lambda_2^3$.

$$\begin{aligned}
\frac{\partial f}{\partial \lambda_1} &= \frac{f_0}{2}\left\{\left[-(1-a\lambda_2)\frac{2a}{\Omega^3}\right]+\left[1-\frac{1-a\lambda_2}{\Omega}\right]\left[\frac{1}{2\lambda_1^2}t\,(1+a\lambda_2+\Omega)+\frac{1}{2\lambda_1}t\left(\frac{2a}{\Omega}\right)\right]\right\}e_p \\
&\quad +\frac{f_0}{2}\left\{\left[(1-a\lambda_2)\frac{2a}{\Omega^3}\right]+\left[1+\frac{1-a\lambda_2}{\Omega}\right]\left[\frac{1}{2\lambda_1^2}t\,(1+a\lambda_2-\Omega)-\frac{1}{2\lambda_1}t\left(\frac{2a}{\Omega}\right)\right]\right\}e_n \\
&= \frac{f_0}{2}\left\{-\frac{C_1}{\Omega^3}+\frac{t}{2\lambda_1^2}\left(2a\lambda_2+\Omega-\frac{C_2}{\Omega}-\frac{\lambda_1 C_1}{\Omega^2}\right)\right\}e_p \\
&\quad +\frac{f_0}{2}\left\{\frac{C_1}{\Omega^3}+\frac{t}{2\lambda_1^2}\left(2a\lambda_2-\Omega+\frac{C_2}{\Omega}-\frac{\lambda_1 C_1}{\Omega^2}\right)\right\}e_n
\end{aligned} \tag{C.15}$$

where $C_1 = 2a(1-a\lambda_2)$ and $C_2 = 1 - 2a\lambda_1 - a^2\lambda_2^2$.

$$
\begin{aligned}
\frac{\partial f}{\partial \lambda_2} &= \frac{f_0}{2}\left\{\left[\frac{a}{\Omega}+(1-a\lambda_2)\frac{(a+a^2\lambda_2)}{\Omega^3}\right]+\left[1-\frac{1-a\lambda_2}{\Omega}\right]\left[-\frac{1}{2\lambda_1}t\left(a+\frac{a+a^2\lambda_2}{\Omega}\right)\right]\right\}e_p \\
&\quad+\frac{f_0}{2}\left\{\left[-\frac{a}{\Omega}-(1-a\lambda_2)\frac{(a+a^2\lambda_2)}{\Omega^3}\right]+\left[1+\frac{1-a\lambda_2}{\Omega}\right]\left[-\frac{1}{2\lambda_1}t\left(a-\frac{a+a^2\lambda_2}{\Omega}\right)\right]\right\}e_n \\
&= \frac{f_0}{2}a\left\{\frac{1}{\Omega}+\frac{C_1}{\Omega^3}-\frac{t}{2\lambda_1}\left(1+\frac{C_2}{\Omega}-\frac{C_1}{\Omega^2}\right)\right\}e_p \\
&\quad+\frac{f_0}{2}a\left\{-\frac{1}{\Omega}-\frac{C_1}{\Omega^3}-\frac{t}{2\lambda_1}\left(1-\frac{C_2}{\Omega}-\frac{C_1}{\Omega^2}\right)\right\}e_n
\end{aligned}
\tag{C.16}
$$

where $C_1 = 1-a^2\lambda_2^2$ and $C_2 = 2a\lambda_2$.

Bibliography

[1] D. van Velzen, R. L. Cardozo, and H. Langenkamp, "A liquid viscosity-temperature-chemical constitution relation for organic compounds," *Ind. & Eng. Chem. Fund.*, vol. 11, no. 1, pp. 20–25, 1972.

[2] B. E. Poling, J. M. Prausnitz, and J. P. O'Connell, *The Properties of Gases and Liquids*. McGraw-Hill, 2001.

[3] J. W. Przedziecki and T. Sridhar, "Prediction of liquid viscosities," *AIChE J.*, vol. 31, no. 2, pp. 333–335, 1985.

[4] R. L. Rowley, W. V. Wilding, J. L. Oscarson, Y. Yang, N. A. Zundel, T. E. Daubert, and R. P. Danner, *DIPPR Data Compilation of Pure Compound Properties*. Design Institute for Physical Properties, AIChE: New York, 2003.

[5] R. B. Bird, W. E. Stewart, and E. N. Lightfoot, *Transport Phenomena*. John Wiley & Sons, Inc., 2nd ed., 2002.

[6] D. Reichenberg, "The viscosity of organic vapors at low pressures," Tech. Rep. DSC Rep. 11, National Physical Laboratory, Teddington, England, Aug. 1971.

[7] D. Reichenberg, "The indeterminacy of the values of potential parameters as derived from transport and virial coefficients," *AIChE J.*, vol. 19, no. 4, pp. 854–856, 1973.

[8] D. Reichenberg, "New methods for the estimation of the viscosity coefficients of pure gases at moderate pressures (with particular reference to organic vapors)," *AIChE J.*, vol. 21, no. 1, pp. 181–183, 1975.

[9] P. Yoon and G. Thodos, "Viscosity of nonpolar gaseous mixtures at normal pressures," *AIChE J.*, vol. 16, no. 2, pp. 300–304, 1970.

[10] L. I. Stiel and G. Thodos, "The viscosity of polar substances in the dense gaseous and liquid regions," *AIChE J.*, vol. 10, no. 2, pp. 275–277, 1964.

[11] T.-H. Chung, L. L. Lee, and K. E. Starling, "Applications of kinetic gas theories and multiparameter correlation for prediction of dilute gas viscosity and thermal conductivity," *Ind. & Eng. Chem. Fund.*, vol. 23, no. 1, pp. 8–13, 1984.

[12] K. J. Okeson and R. L. Rowley, "A four-parameter corresponding-states method for prediction of Newtonian, pure-component viscosity," *Int. J. Thermophysics*, vol. 12, no. 1, pp. 119–136, 1991.

[13] P. D. Neufeld, A. R. Janzen, and R. A. Aziz, "Empirical equations to calculate 16 of the transport collision integrals $\Omega^{(l,s)*}$ for the Lennard-Jones (12–6) potential," *The Journal of Chemical Physics*, vol. 57, no. 3, pp. 1100–1102, 1972.

[14] H.-C. Hsu, Y.-W. Sheu, and C.-H. Tu, "Viscosity estimation at low temperatures ($T_r <$ 0.75) for organic liquids from group contributions," *Chem. Eng. J.*, vol. 88, no. 1, 2002.

[15] V. R. Bhethanabotla, "A group contribution method for liquid viscosity," Master's thesis, The Pennsylvania State University, University Park, PA, 1983.

[16] L. H. Thomas, "The dependence of the viscosities of liquids on reduced temperature, and a relation between viscosity, density, and chemical constitution," *J. Chem. Soc.*, 1946.

[17] J. H. Hildebrand, *Viscosity and Diffusivity: A Predictive Treatment*. John Wiley & Sons, Inc., 1977.

[18] R. C. Reid, J. M. Prausnitz, and B. E. Poling, *The Properties of Gases and Liquids*. McGraw-Hill, New York, 4th ed., 1987.

[19] K. G. Joback and R. C. Reid, "Estimation of pure-component properties from group contribution," *Chem. Eng. Comm.*, vol. 57, no. 1, pp. 233–243, 1987.

[20] J. F. Ely and H. J. M. Hanley, "Prediction of transport properties. 1 viscosity of fluids and mixtures," *Ind. Eng. Chem. Fundam.*, vol. 20, 1981.

[21] M. P. Allen and D. J. Tildesley, *Computer Simulation of Liquids*. Oxford University Press, 1989.

[22] D. Frenkel and B. Smit, *Understanding Molecular Simulation From Algorithms to Applications*. 2nd ed., 2002.

[23] D. M. Heyes, "Transport coefficients of simple fluids with steeply repulsive potentials," *J. Phys. Condensed Mat.*, vol. 6, 1994.

[24] K. Meier, A. Laesecke, and S. Kabelac, "Transport coefficients of the Lennard-Jones model fluid. I. Viscosity," *J. Chem. Phys.*, vol. 121, no. 8, pp. 3671–3687, 2004.

[25] R. Vogelsang, C. Hoheisel, and G. Ciccotti, "Thermal conductivity of the Lennard-Jones liquid by molecular dynamics calculations," *J. Chem. Phys.*, vol. 86, no. 11, pp. 6371–6375, 1987.

[26] D. J. Evans, "Homogeneous nemd algorithm for thermal conductivity: Application of non-canonical linear response theory," *Phys. Lett. A*, vol. 91, no. 9, pp. 457–460, 1982.

[27] D. J. Evans, W. G. Hoover, B. H. Failor, B. Moran, and A. J. C. Ladd, "Nonequilibrium molecular dynamics via Gauss's principle of least constraint," *Phys. Rev. A*, vol. 28, no. 2, pp. 1016–1021, 1983.

[28] D. J. Evans and O. P. Morriss, "Non-newtonian molecular dynamics," *Computer Phys. Rep.*, vol. 1, no. 6, pp. 297–343, 1984.

[29] D. J. Evans and G. P. Morriss, "Nonlinear-response theory for steady planar Couette flow," *Phys. Rev. A*, vol. 30, no. 3, pp. 1528–1530, 1984.

[30] F. Muller-Plathe, "A simple nonequilibrium molecular dynamics method for calculating the thermal conductivity," *J. Chem. Phys.*, vol. 106, no. 14, pp. 6082–6085, 1997.

[31] V. R. Vasquez, E. A. Macedo, and M. S. Zabaloy, "Lennard-Jones viscosities in wide ranges of temperature and density: Fast calculations using a steady-state periodic perturbation method," *Int. J. Thermophysics*, vol. 25, no. 6, pp. 1799–1818, 2004.

[32] B. Hess, "Determining the shear viscosity of model liquids from molecular dynamics simulations," *J. Chem. Phys.*, vol. 116, no. 1, pp. 209–217, 2002.

[33] H. J. C. Berendsen, J. P. M. Postma, W. F. van Gunsteren, A. DiNola, and J. R. Haak, "Molecular dynamics with coupling to an external bath," *J. Chem. Phys.*, vol. 81, no. 8, pp. 3684–3690, 1984.

[34] H. J. C. Berendsen, "Transport properties computed by linear response through weak coupling to a bath," *Computer Simulations in Material Science*, 1991.

[35] A. W. Lees and S. F. Edwards, "The computer study of transport processes under extreme conditions," *J. Phys. C*, vol. 5, 1972.

[36] D. R. Wheeler, N. G. Fuller, and R. L. Rowley, "Non-equilibrium molecular dynamics simulation of the shear viscosity of liquid methanol: adaptation of the Ewald sum to Lees-Edwards boundary conditions," *Mol. Phys.*, vol. 92, no. 1, pp. 55–62, 1997.

[37] G. Pan and C. McCabe, "Prediction of viscosity for molecular fluids at experimentally accessible shear rates using the transient time correlation function formalism," *J. Chem. Phys.*, vol. 125, no. 19, pp. 194527/1–194527/9, 2006.

[38] D. J. Evans and G. P. Morriss, *Statistical Mechanics of Nonequilibrium Liquids*. Academic Press, New York, 1990.

[39] D. J. Evans, H. J. M. Hanley, and S. Hess, "Non-newtonian phenomena in simple fluids," *Physics Today*, vol. 37, no. 1, pp. 26–33, 1984.

[40] A. Berker, S. Chynoweth, U. C. Klomp, and Y. Michopoulos, "Non-equilibrium molecular dynamics (nemd) simulations and the rheological properties of liquid n-hexadecane," *J. Chem. Soc. Faraday T.*, vol. 88, 1992.

[41] J.-P. Ryckaert, A. Bellemans, G. Ciccotti, and G. V. Paolini, "Shear-rate dependence of the viscosity of simple fluids by nonequilibrium molecular dynamics," *Phys. Rev. Lett.*, vol. 60, no. 2, pp. 128–131, 1988.

[42] C. Pierleoni and J.-P. Ryckaert, "Non-newtonian viscosity of atomic fluids in shear and shear-free flows," *Phys. Rev. A*, vol. 44, no. 8, pp. 5314–5317, 1991.

[43] G. V. Vinogradov and A. Yakovlevich Malkin, *Rheology of Polymers*. Springer, Berlin, 1980.

[44] R. B. Bird, R. C. Armstrong, and O. Hassager, *Dynamics of Polymeric Liquids*. Wiley, New York, 1987.

[45] R. L. Rowley and J. F. Ely, "Nonequilibrium molecular dynamics simulations of n-butane and isobutane viscosity," *Mol. Simulation*, vol. 7, no. 5, 1991.

[46] R. L. Rowley and J. F. Ely, "Non-equilibrium molecular dynamics simulations of structured molecules Part I. Isomeric effects on the viscosity of butanes," *Mol. Phys.*, vol. 72, no. 4, pp. 831–846, 1991.

[47] Y. Yang, T. A. Pakkanen, and R. L. Rowley, "Nemd simulations of viscosity and viscosity index for lubricant-size model molecules," *Int. J. Thermophysics*, vol. 23, no. 6, pp. 1441–1454, 2002.

[48] E. J. Maginn, A. T. Bell, and D. N. Theodorou, "Transport diffusivity of methane in silicalite from equilibrium and nonequilibrium simulations," *J. Phys. Chem.*, vol. 97, no. 16, pp. 4173–4181, 1993.

[49] G. Arya, E. J. Maginn, and H.-C. Chang, "Efficient viscosity estimation from molecular dynamics simulation via momentum impulse relaxation," *J. Chem. Phys.*, vol. 113, no. 6, pp. 2079–2087, 2000.

[50] R. J. Hulse, R. L. Rowley, and W. V. Wilding, "Transient nonequilibrium molecular dynamic simulations of thermal conductivity: 1. Simple fluids," *Int. J. Thermophysics*, vol. 26, no. 1, pp. 1–12, 2005.

[51] R. J. Hulse, *Thermal Conductivity of Liquids and Gases Through Experiment and Molecular Dynamic Simulations*. Ph.D. Dissertation, Brigham Young University, Provo, Utah, Dec. 2003.

[52] R. L. Rowley and M. M. Painter, "Diffusion and viscosity equations of state for a Lennard-Jones fluid obtained from molecular dynamics simulations," *Int. J. Thermophysics*, vol. 18, no. 5, pp. 1109–1121, 1997.

[53] M. S. Kelkar and E. J. Maginn, "Rapid shear viscosity calculation by momentum impulse relaxation molecular dynamics," *J. Chem. Phys.*, vol. 123, 2005.

[54] E. Keshavarzi, M. Vahedpour, S. Alavi, and B. Najafi, "High-frequency shear modulus and relaxation time of soft-sphere and Lennard-Jones fluids," *Int. J. Thermophysics*, vol. 25, no. 6, pp. 1747–1762, 2004.

[55] R. B. Bird, W. E. Stewart, and E. N. Lightfoot, *Dynamics of Polymeric Liquids Volume 1*. John Wiley & Sons, Inc., 2nd ed., 2002.

[56] D. A. McQuarrie, *Statistical Mechanics*. Harper & Row, New York, 1976.

[57] L. V. Woodcock, "Equation of state for the viscosity of Lennard-Jones fluids," *AIChE J.*, vol. 52, no. 2, pp. 438–446, 2006.

[58] N. G. Fuller and R. L. Rowley, "The effect of model internal flexibility upon nemd simulations of viscosity," *Int. J. Thermophysics*, vol. 21, no. 1, pp. 45–55, 2000.

[59] D. R. Wheeler and J. Newman, "A less expensive Ewald lattice sum," *Chem. Phys. Lett.*, vol. 366, 2002.

[60] T. Darden, D. York, and L. Pedersen, "Particle mesh Ewald: An N log(N) method for Ewald sums in large systems," *J. Chem. Phys.*, vol. 98, no. 12, pp. 10089–10092, 1993.

[61] M. Deserno and C. Holm, "How to mesh up Ewald sums. I. A theoretical and numerical comparison of various particle mesh routines," *J. Chem. Phys.*, vol. 109, no. 18, pp. 7678–7693, 1998.

[62] M. Deserno and C. Holm, "How to mesh up Ewald sums. II. An accurate error estimate for the particle-particle-particle-mesh algorithm," *J. Chem. Phys.*, vol. 109, no. 18, pp. 7694–7701, 1998.

[63] W. L. Jorgensen, J. D. Madura, and C. J. Swenson, "Optimized intermolecular potential functions for liquid hydrocarbons," *J. Am. Chem. Soc.*, vol. 106, no. 22, pp. 6638–6646, 1984.

[64] W. L. Jorgensen and J. Tirado-Rives, "The OPLS potential functions for proteins. Energy minimizations for crystals of cyclic peptides and crambin," *J. Am. Chem. Soc.*, vol. 110, no. 6, pp. 1657–1666, 1988.

[65] W. L. Jorgensen, D. S. Maxwell, and J. Tirado-Rives, "Development and testing of the OPLS all-atom force field on conformational energetics and properties of organic liquids," *J. Am. Chem. Soc.*, vol. 118, no. 45, pp. 11225–11236, 1996.

[66] R. C. Rizzo and W. L. Jorgensen, "OPLS all-atom model for amines: Resolution of the amine hydration problem," *J. Am. Chem. Soc.*, vol. 121, no. 20, pp. 4827–4836, 1999.

[67] G. A. Kaminski, R. A. Friesner, J. Tirado-Rives, and W. L. Jorgensen, "Evaluation and reparametrization of the OPLS-AA force field for proteins via comparison with accurate quantum chemical calculations on peptides," *J. Phys. Chem. B*, vol. 105, no. 28, pp. 6474–6487, 2001.

[68] M. G. Martin and J. I. Siepmann, "Transferable potentials for phase equilibria. 1. United-atom description of n-alkanes," *J. Phys. Chem. B*, vol. 102, no. 14, pp. 2569–2577, 1998.

[69] M. G. Martin and J. I. Siepmann, "Novel configurational-bias Monte Carlo method for branched molecules. Transferable potentials for phase equilibria. 2. United-atom description of branched alkanes," *J. Phys. Chem. B*, vol. 103, no. 21, pp. 4508–4517, 1999.

[70] B. Chen and J. I. Siepmann, "Transferable potentials for phase equilibria. 3. Explicit-hydrogen description of normal alkanes," *J. Phys. Chem. B*, vol. 103, no. 25, pp. 5370–5379, 1999.

[71] C. D. Wick, M. G. Martin, and J. I. Siepmann, "Transferable potentials for phase equilibria. 4. United-atom description of linear and branched alkenes and alkylbenzenes," *J. Phys. Chem. B*, vol. 104, no. 25, pp. 8008–8016, 1999.

[72] B. Chen, J. J. Potoff, and J. I. Siepmann, "Monte Carlo calculations for alcohols and their mixtures with alkanes. Transferable potentials for phase equilibria. 5. United-atom description of primary, secondary, and tertiary alcohols," *J. Phys. Chem. B*, vol. 105, no. 15, pp. 3093–3104, 2001.

[73] J. M. Stubbs, J. J. Potoff, and J. I. Siepmann, "Transferable potentials for phase equilibria. 6. United-atom description for ethers, glycols, ketones, and aldehydes," *J. Phys. Chem. B*, vol. 108, no. 45, pp. 17596–17605, 2004.

[74] C. D. Wick, J. M. Stubbs, N. Rai, and J. I. Siepmann, "Transferable potentials for phase equilibria. 7. Primary, secondary, and tertiary amines, nitroalkanes and nitrobenzene, nitriles, amides, pyridine, and pyrimidine," *J. Phys. Chem. B*, vol. 109, no. 40, pp. 18974–18982, 2005.

[75] N. Lubna, G. Kamath, J. J. Potoff, N. Rai, and J. I. Siepmann, "Transferable potentials for phase equilibria. 8. United-atom description for thiols, sulfides, disulfides, and thiophene," *J. Phys. Chem. B*, vol. 109, no. 50, pp. 24100–24107, 2005.

[76] N. Rai and J. I. Siepmann, "Transferable potentials for phase equilibria. 9. Explicit hydrogen description of benzene and five-membered and six-membered heterocyclic aromatic compounds," *J. Phys. Chem. C*, vol. 111, no. 36, pp. 10790–10799, 2007.

[77] J. C. Thomas and R. L. Rowley, "Transient molecular dynamics simulations of viscosity for simple fluids," *J. Chem. Phys.*, vol. 127, 2007.

[78] H. J. C. Berendsen, J. R. Grigera, and T. P. Straatsma, "The missing term in effective pair potentials," *J. Phys. Chem.*, vol. 91, no. 24, pp. 6269–6271, 1987.

[79] J.-P. Ryckaert and A. Bellemans, "Molecular dynamics of liquid alkanes," *Faraday Discuss. Chem. Soc.*, vol. 66, 1978.

[80] R. L. Rowley and J. F. Ely, "Non-equilibrium molecular dynamics simulations of structured molecules Part II. Isomeric effects on the viscosity of models for n-hexane, cyclohexane and benzene," *Mol. Phys.*, vol. 75, no. 3, pp. 713–730, 1992.

[81] S. Balasubramanian, C. J. Mundy, and M. L. Klein, "Shear viscosity of polar fluids: Molecular dynamics calculations of water," *J. Chem. Phys.*, vol. 105, no. 24, pp. 11190–11195, 1996.

[82] D. R. Wheeler and R. L. Rowley, "Shear viscosity of polar liquid mixtures via non-equilibrium molecular dynamics: water, methanol, and acetone," *Mol. Phys.*, vol. 94, no. 3, pp. 555–564, 1998.

[83] D. R. Wheeler and J. Newman, "Molecular dynamics simulations of multicomponent diffusion. 1. Equilibrium method," *J. Phys. Chem. B*, vol. 108, no. 47, pp. 18353–18361, 2004.

[84] K. I. Katsuji Noda, Mitsuhisa Ohashi, "Viscosities and densities at 298.15 k for mixtures of methanol, acetone, and water," *J. Chem. Eng. Data*, vol. 27, no. 3, pp. 326–328, 1982.